UNIVERSITY OF CALIFORNIA SAN DIEGO

Deepening the Understanding of Lithium Phosphorus Oxynitride and Associated Interfaces

via Advanced Electron Microscopy in All-solid-state Thin Film Batteries

A dissertation submitted in partial satisfaction of the requirements for
the degree Doctor of Philosophy

in

Materials Science and Engineering

by

Diyi Cheng

Committee in charge:

Professor Ying Shirley Meng, Chair
Professor Eric Fullerton, Co-chair
Professor Zheng Chen
Professor David Fenning
Professor Andrew Kummel
Professor Ping Liu

2023

The Dissertation of Diyi Cheng is approved, and it is acceptable in
quality and form for publication on microfilm and electronically.

University of California San Diego

2023

DEDICATION

To my beloved parents Yuan Cheng and Lianrong Huyan

To all my lovely friends through this journey

TABLE OF CONTENTS

LIST OF TABLES

Arvind Kamath, Dr. Khanh Tran, Dr. Zhongchun Wang, Shoba Rao and Richard van der Linde from Ensurge Micropower.

Last but not least, I would like to thank my parents and other family members. Your patience, love and support has become an indispensable part through this journal. And I would like to thank all my lovely friends that are always there to back me up and share the joy of life.

Chapter 2, in part, is a reprint of the material, as it appears in a manuscript that is being prepared to submit for publication: D. Cheng, K. Tran, S. Rao, Z. Wang, R. van der Linde, A. Kamath and Y. S. Meng, "Manufacturing Scale-Up of Anodeless Solid State Lithium Thin Film Battery for High Volumetric Energy Density Application", 2023. The dissertation author was the primary investigator and first author of this paper.

Chapter 3, in full, is a reprint of the material, as it appears in: D. Cheng, B. Lu, G. Raghavendran, M. Zhang and Y. S. Meng, "Leveraging Cryogenic Electron Microscopy for Advancing Battery Design", *Matter*, 2022, 5, 26–42. The dissertation author was the primary investigator and first author of this paper.

Chapter 4, in full, is a reprint of the material, as it appears in: D. Cheng, T. A. Wynn, X. Wang, S. Wang, M. Zhang, R. Shimizu, S. Bai, H. Nguyen, C. Fang, M. Kim, W. Li, B. Lu, S. J.

Kim and Y. S. Meng, "Unveiling the Stable Nature of the Solid Electrolyte Interphase between Lithium Metal and LiPON via Cryogenic Electron Microscopy", *Joule*, 2020, 4, 11, 2484-2500. The dissertation author was the primary investigator and first author of this paper.

Chapter 5, in full, is a reprint of the material, as it appears in: R. Shimizu*, D. Cheng*, J. L. Weaver, B. Lu, T. Wynn, M. Kim, G. Zhu, M. Zhang and Y. S. Meng, "Unraveling the stable cathode electrolyte interface in all solid-state thin-film battery operating at 5V", *Adv. Energy Mater.* 2022, 2201119. The dissertation author was the co-primary investigator and co-first author of this paper.

Chapter 6, in full, is a reprint of the material, as it appears in a work that is currently under rebuttal with *Nature Nanotechnology*: D. Cheng, T. Wynn, B. Lu, B. Han, R. Shimizu, B. Sreenarayanan, M. Marple, Y. Yang, H. Nguyen, W. Li, G. Zhu, M. Zhang and Y. S. Meng, "Freestanding LiPON: from Fundamental Study to Uniformly Dense Li Metal Deposition Under Zero External Pressure", 2023. The dissertation author was the primary investigator and first author of this paper.

Chapter 7, in part, is a reprint of the material, as it appears in: D. Cheng, B. Lu, G. Raghavendran, M. Zhang and Y. S. Meng, "Leveraging Cryogenic Electron Microscopy for Advancing Battery Design", *Matter*, 2022, 5, 26–42. The dissertation author was the primary investigator and first author of this paper.

VITA

2017   Bachelor of Science in Materials Physics, Jilin University

2019   Master of Science, University of California San Diego

2023   Doctor of Philosophy, University of California San Diego

PUBLICATIONS

(* authors contributed equally to the work)

D. Cheng, T. A. Wynn, X. Wang, S. Wang, M. Zhang, R. Shimizu, S. Bai, H. Nguyen, C. Fang, M. Kim, W. Li, B. Lu, S. J. Kim and Y. S. Meng, "Unveiling the Stable Nature of the Solid Electrolyte Interphase between Lithium Metal and LiPON via Cryogenic Electron Microscopy", *Joule*, 2020, 4, 11, 2484-2500

M. Kim*, N. Ahn*, **D. Cheng***, M. Xu, S. Ham, X. Pan, S. J. Kim, Y. Luo, D. P. Fenning, D. H. S. Tan, M. Zhang, G. Zhu, K. Jeong, M. Choi and Y. S. Meng, "Imaging Real-Time Amorphization of Hybrid Perovskite Solar Cells under Electrical Biasing", *ACS Energy Lett.* 2021, 6, 3530−3537

D. Cheng, B. Lu, G. Raghavendran, M. Zhang and Y. S. Meng, "Leveraging Cryogenic Electron Microscopy for Advancing Battery Design", *Matter*, 2022, 5, 26–42

R. Shimizu*, **D. Cheng***, J. L. Weaver, B. Lu, T. Wynn, M. Kim, G. Zhu, M. Zhang and Y. S. Meng, "Unraveling the stable cathode electrolyte interface in all solid-state thin-film battery operating at 5V", *Adv. Energy Mater.* 2022, 2201119

D. Cheng, T. Wynn, B. Lu, B. Han, R. Shimizu, B. Sreenarayanan, M. Marple, Y. Yang, H. Nguyen, W. Li, G. Zhu, M. Zhang and Y. S. Meng, "Freestanding LiPON: from Fundamental Study to Uniformly Dense Li Metal Deposition Under Zero External Pressure", *Nature Nanotechnology*, 2023, Under rebuttal

D. Cheng, K. Tran, S. Rao, Z. Wang, R. van der Linde, A. Kamath and Y. S. Meng, "Manufacturing Scale-Up of Anodeless Solid State Lithium Thin Film Battery for High Volumetric Energy Density Application", 2023, Manuscript in preparation

M. Zhang*, **D. Cheng***, B. Lu, M. Chouchane, Z. Liu, B. Han, Y. Chen, S. Bai, L. Li, B. B. Van Leer, R. Passey, A. Stokes, M. McClendon, J. Jang, G. Raghavendran, J. Lee and Y. S. Meng, "Room Temperature Study on Microstructure and Reactivity of Lithium Metal for Optimizing Electrochemical Reversibility", 2023, Manuscript in preparation

M. A. T. Marple, T. A. Wynn, **D. Cheng**, R. Shimizu, H. E. Mason, and Y. S. Meng, "Local structure of glassy lithium phosphorus oxynitride thin films: a combined experimental and ab initio approach", *Angew. Chem. Int. Ed.* 2020, 59, 2–11

M. Kim, S. Ham, **D. Cheng**, T. A. Wynn, H. S. Jung and Y. S. Meng, "Advanced Characterization Techniques for Overcoming Challenges of Perovskite Solar Cell Materials", *Adv. Energy Mater.* 2020, 2001753

W. Yim, **D. Cheng**, S. H. Patel, R. Kou, Y. S. Meng and J. V. Jokerst, "KN95 and N95 Respirators Retain Filtration Efficiency despite a Loss of Dipole Charge during Decontamination", *ACS Appl. Mater. Interfaces*, 2020, 12, 49, 54473–5448

S. Zhao, D. Xia, M. Li, **D. Cheng**, K. Wang, Y. S. Meng, Z. Chen & J. Bae, "Self-Healing and Anti-CO2 Hydrogels for Flexible Solid-State Zinc-Air Batteries", *ACS Applied Materials & Interfaces*, 2021, 13, 10, 12033–12041

C. Fang, B. Lu, G. Pawar, M. Zhang, **D. Cheng**, S. Chen, M. Ceja, J. Doux, H. Musrock, M. Cai, B. Liaw and Y. S. Meng, "Pressure-tailored lithium deposition and dissolution in lithium metal batteries", *Nature Energy* 2021, 6, 987–994

B. Sayahpour, H. Hirsh, S. Bai, N. B. Schorr, T. N. Lambert, M. Mayor, W. Bao, **D. Cheng**, M. Zhang, K. Leung, K. L. Harrison, W. Li and Y. S. Meng, "Revisiting Discharge Mechanism of CFx as A High Energy Density Cathode Material for Lithium Primary Battery", *Adv. Energy Mater.* 2021, 2103196

B. Lu, E. Olivera, J. Scharf, M. Chouchane, C. Fang, M. Ceja, L. E. Pangilinan, S. Zheng, A. Dawson, **D. Cheng**, W. Bao, O. Arcelus, A. A. Franco, X. Li, S. H. Tolbert & Y. S. Meng, "Quantitatively Designing Porous Copper Current Collectors for Lithium Metal Anodes", *ACS Appl. Energy Mater.* 2021

W. Bao, C. Fang, **D. Cheng**, Y. Zhang, B. Lu, D. H. S. Tan, R. Shimizu, B. Sreenarayanan, S. Bai, W. Li, M. Zhang and Y. S. Meng, "Quantifying lithium loss in amorphous silicon thin-film anodes via titration-gas chromatography", *Cell Reports Physical Science*, 2021, 2,100597

Y. Li, W. Li, R. Shimizu, **D. Cheng**, H. Nguyen, J. Paulsen, S. Kumakura, M. Zhang and Y. S. Meng, "Elucidating the Effect of Borate Additive in High-Voltage Electrolyte for Li-Rich Layered Oxide Materials", *Adv. Energy Mater.* 2022, 2103033

Y. Yin, Y. Yang, **D. Cheng**, M. Mayer, J. Holoubek, W. Li, G. Raghavendran, A. Liu, B. Lu, D. M. Davies, Z. Chen, O. Borodin and Y. S. Meng, "Fire-extinguishing, recyclable liquefied gas electrolytes for temperature-resilient lithium-metal batteries", *Nature Energy*, 2022, 7, 548–559

J. Jang, Y. Chen, G. Deysher, **D. Cheng**, S. Ham, A. Cronk, P. Ridley, H. Yang, B. Sayahpour, B. Han, W. Li, W. Yao, E. A. Wu, J. Doux, L. H. B. Nguyen, J. A. S. Oh, D. H. S. Tan and Y. S. Meng, "Enabling a Co-Free, High-Voltage LiNi0.5Mn1.5O4 Cathode in All-Solid-State Batteries with a Halide Electrolyte", *ACS Energy Lett.* 2022, 7, 2531−2539

H. Chung, Y. Li, M. Zhang, A. Grenier, C. Mejia, **D. Cheng**, B. Sayahpour, C. Song, M. H. Shen, R. Huang, E. A. Wu, K. W. Chapman, S. J. Kim and Y. S. Meng, "Mitigating Anisotropic Changes in Classical Layered Oxide Materials by Controlled Twin Boundary Defects for Long Cycle Life Li-Ion Batteries", *Chem. Mater.* 2022, 34, 16, 7302–7312

W. Li, **D. Cheng**, R. Shimizu, Y. Li, W. Yao, G. Raghavendran, M. Zhang, Y. S. Meng, "Artificial Cathode Electrolyte Interphase for Improving High Voltage Cycling Stability of Thick Electrode with Co-Free 5 V Spinel Oxides", *Energy Storage Materials*, 2022, 49, 77-84

B. Lu, W. Li, **D. Cheng**, B. Bhamwala, M. Ceja, W. Bao, C. Fang and Y. S. Meng, "Suppressing Chemical Corrosions of Lithium Metal Anodes", *Adv. Energy Mater.* 2022, 2202012

S. Wang, B. Lu, **D. Cheng**, Z. Wu, S. Feng, M. Zhang, W. Li, Q. Miao, M. Patel, J. Feng, E. Hopkins, J. Zhou, S. Parab, B. Bhamwala, B. Liaw, Y. Meng, P. Liu, "Structural Transformation in Sulfurized Polymer Cathode to Enable Long Life Rechargeable Lithium Sulfur Batteries", *J. Am. Chem. Soc.* 2023, Accepted

B. Lu, **D. Cheng**, B. Sreenarayanan, W. Li, B. Bhamwala, W. Bao, Y. S. Meng, "Key Parameters in Determining the Reactivity of Lithium Metal Battery", *Energy Environ. Sci.*, 2023, Under Review

ABSTRACT OF THE DISSERTATION

Deepening the Understanding of Lithium Phosphorus Oxynitride and Associated Interfaces via

Advanced Electron Microscopy in All-solid-state Thin Film Batteries

by

Diyi Cheng

Doctor of Philosophy in Materials Science and Engineering

University of California San Diego, 2023

Professor Ying Shirley Meng, Chair
Professor Eric Fullerton, Co-chair

Since the discovery of intercalation chemistry in the early 70s, lithium battery technology has been rapidly developed through the efforts in expanding cathodes chemistry for higher energy density, exploring advanced electrolytes for nonflammability and wider voltage window, and enabling high theoretical capacity anode materials. Nevertheless, the ideal anode candidate, Li metal, remains as the holy grail for researchers in the fields of both liquid-electrolyte battery and

its solid-state analogues. Future advancement of safe Li metal battery calls for new strategies to enable uniform Li metal plating/stripping at lower stacking pressure and to stabilize Li metal interfaces by engineering. In this dissertation, by leveraging the well-defined interface platforms in all-solid-state thin film battery and utilizing advanced electron microscopy, we demonstrate the fresh understanding at electrode/electrolyte interfaces in a battery system that employs lithium phosphorus oxynitride (LiPON) as the solid-state electrolyte. Firstly, cryogenic electron microscopy unveils a 76-nm-thick Li/LiPON interface that consists of Li_2O, Li_3N and Li_3PO_4 as the interphase components, which are embedded in an amorphous matrix and exhibit chemical gradients across the interface. Next, the interface between LiPON and a high-voltage $LiNi_{0.5}Mn_{1.5}O_{1.5}$ (LNMO) cathode shows overlithiation on the surface of pristine LNMO near the interface. The LNMO/LiPON interface contact remains intact after over 500 cycles, suggesting the essence of both atomic interface contact and removing conductive agents on achieving interfacial stability at high voltage. The efforts on producing a freestanding LiPON film offered invaluable quantitative insights on interface formation between Li metal and LiPON by solid-state NMR, which serves as supportive evidence to the electron microscopy observation. DSC measurement yields a well-defined glass transition temperature of LiPON. Nanoindentation shows a Young's modulus of ~33GPa of LiPON, which could be related to the residual stress release process in the freestanding form. Moreover, freestanding LiPON is demonstrated to enable Li metal plating in a uniform and fully dense manner without external pressure. Such observations not only provide new insight on interface engineering strategy in bulk batteries, but also shed light on reducing the external pressure on Li metal all-solid-state batteries that is required for stable cycling.

Chapter 1. Introduction

1.1 Motivation

Global energy crisis and climate change are two pressing issues confronted by human society in the present century. Although fossil fuels including coal, natural gas and oil are the key drivers of world-wide economic growth since the first industrial evolution, the overmining and overuse of fossil fuels have resulted in some severe environmental issues, where global warming appeared to be the most prominent one.[1,2] Moreover, the world's growing population has led to a rising demand for energy that surpasses the available fossil fuel resources in the coming centuries.[1] To alleviate the energy crisis and mitigate climate change, developing sustainable energy resources and reducing the emission of greenhouse gas have become the mutual tasks for all humankind presently.
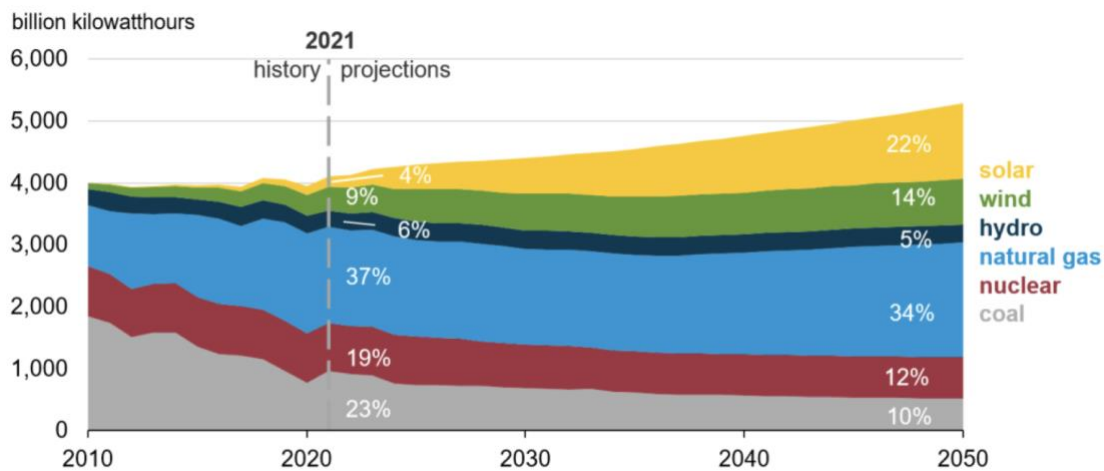
Figure 1.1 U.S. electricity generation from selected fuels from 2010 to 2050.[2]

Figure 1.1 recorded the history and projection of U.S. electricity generation from selected fuels that include solar power, wind power, hydropower, natural gas, nuclear energy and coal till 2050.[2] Despite the continuous increase of total electricity demand, the contribution of sustainable

1

energy resources such as solar power, wind power and hydropower are predicted to be largely

growing in the coming decades, adding up to 41% for the total available electricity supply in 2050.

The projection of such growth of sustainable energy resources manifests the effort that has been

devoted to mitigating energy crisis. Nevertheless, an emerging problem along with the

development of sustainable energy resources is how to store such large amount of energy to

maximize the utilization efficiency, considering the availability, variability and uncertainty of such

energy resources when they are generated.[3]
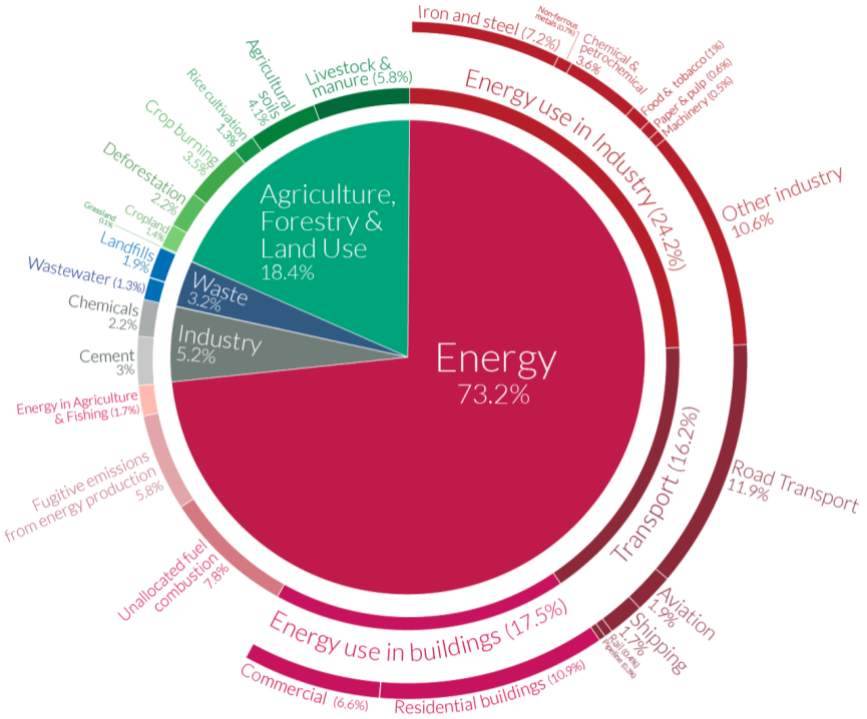
Figure 1.2 Global greenhouse gas emission by sector in 2020.[4]

On the other hand, reducing the emission of greenhouse gas calls for changes in many

sectors related to daily life and production. Among all the sectors that emit greenhouse gas,

transport sector yields a leading portion with 16.2% of the total global greenhouse gas emission in

2020 (Figure 1.2).[4] Within the transport sector, road transport that includes both passenger travel

and road freight contribute up to 11.9% of the total greenhouse gas emission. Therefore, the

electrification of road transport sector and transition to a fully decarbonized electricity mix are essential for reducing global greenhouse gas emission by a large extent.[4]

As such, rechargeable battery technology serves as a sound solution to the question of energy storage for both sustainable energy resources and electrifying road vehicle. Among all the rechargeable battery chemistries discovered, including nickel/cadmium (Ni/Cd) battery, lead-acid battery, nickel-metal hydride (Ni/MH) battery, intercalation-chemistry battery, etc., lithium battery is the most-developed type due to its higher energy density and lower toxicity.[5] Though the last five decades have seen tremendous progress made in modern lithium battery technology, current state-of-art lithium-ion battery still falls short to the demanding requirement for higher energy density and safety. With the complexity of battery system, it is non-trivial to realize the ultimate goal of utilizing Li metal anode and implementing safer solid-state electrolytes in rechargeable batteries, which still call for further research efforts to explore the unknowns hidden at the many buried interfaces.

1.2 Lithium battery technology

Battery is a closed electrochemical system for energy storage and conversion, where electrical energy is stored in the form of chemical energy via redox reactions and is released when the battery is discharged. Rechargeability of a battery is defined when the redox reactions can occur repeatedly in a quasi-reversible way.[5,6] With the many rechargeable battery chemistries explored in history, including nickel/cadmium (Ni/Cd) battery, lead-acid battery, nickel-metal hydride (Ni/MH) battery, intercalation-chemistry battery, etc., lithium-based battery has become the most prominent and well-developed one because of its higher energy density and lower toxicity.[5] Modern lithium batteries are generally categorized into lithium-ion battery and lithium metal battery, depending on whether a graphite anode or metallic lithium anode is being used.[7]

Lithium battery is also alternatively categorized into liquid battery and all-solid-state battery, defined by whether a solid-state electrolyte is used for conducting lithium ions.
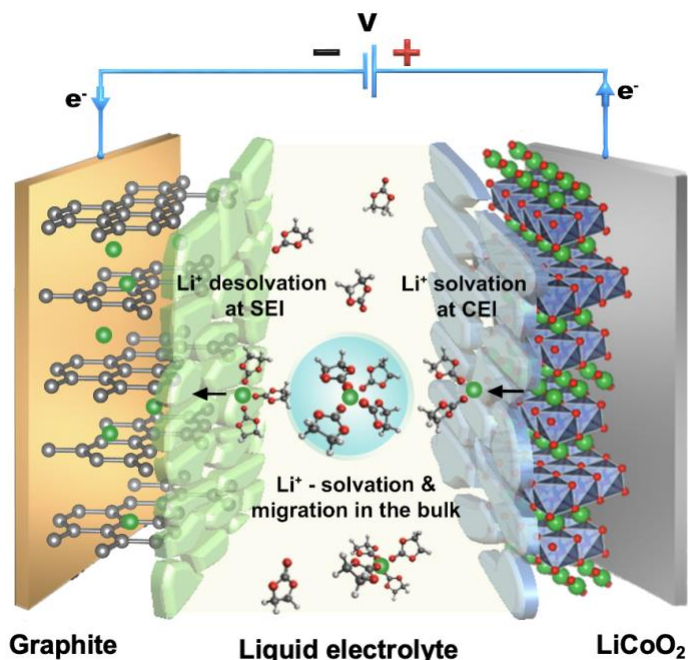
Figure 1.3 A schematic of lithium-ion battery components. The molecules in the electrolyte region represent ethylene carbonate species.[8]

The state-of-the-art lithium-ion battery consists of a layered oxide cathode (lithium cobalt oxide, ($LiCoO_2$, LCO)) to provide the lithium inventory, a layered graphite anode to host lithium ions and an ethylene carbonate liquid electrolyte to conduct lithium ions, as shown in Figure 1.3.[8] During the charging process, lithium ions move towards anode from cathode driven by the external electric field while the transition metal species within cathode material is oxidized. Lithium solvation then occurs in the liquid electrolyte to ensure lithium-ion transportation, where each lithium ion is surrounded by four ethylene carbonate molecules. Lithium ions are subsequently intercalated into the layered structure of graphite anode, where electrical energy is stored in the form of chemical energy. Associated redox reactions occur at cathode and anode sides during charging process can be expressed as follow:

$$\text{Cathode: } LiCoO_2 \leftrightarrow Li_{1-x}CoO_2 + xLi+ + xe- \qquad (1.1)$$

$$\text{Anode: } 6C + xLi + \leftrightarrow Li_xC_6 \qquad (1.2)$$

Upon discharging, electrons flow through the external circuit/device while lithium ions move back to the cathode side, and the chemical energy level of the whole system is decreased. Note that due to the chemical potential mismatch between electrode materials and electrolyte, interphases are commonly formed in battery system, which originate from the decomposition of the electrolyte components on the electrode surface. Such interphase on anode and cathode are called solid electrolyte interphase (SEI) and cathode electrolyte interphase (CEI), respectively, as shown in Figure 1.3. A good interphase allows for facile lithium ion transport, and passivates the electrode surface to alleviate further decomposition reactions.
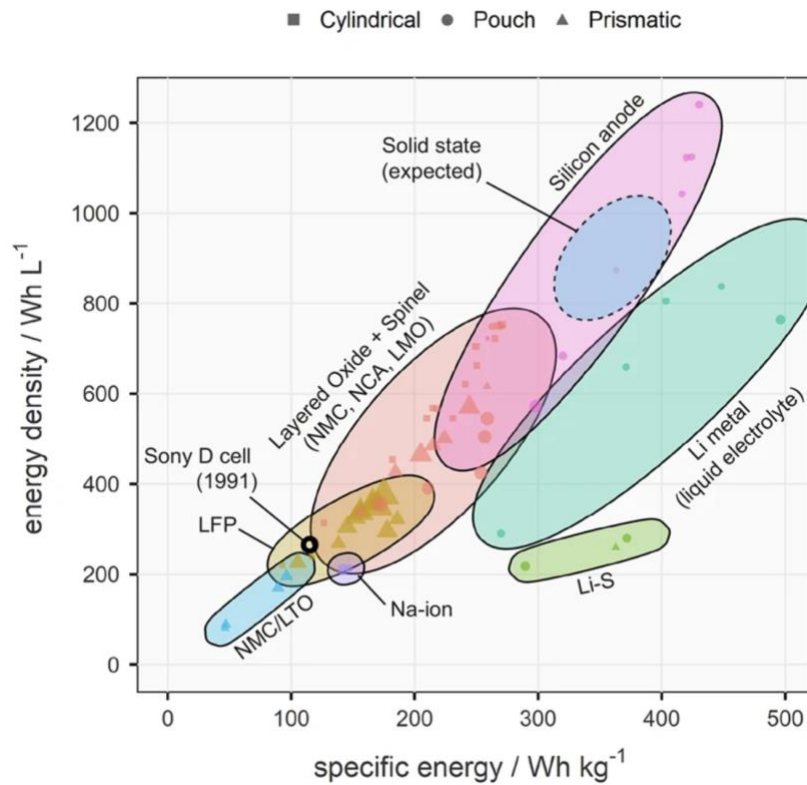
Figure 1.4 Energy density vs specific energy plot for selected Li-ion and "post-Li-ion" cell chemistries[9]

Battery research in the early era focused on the emerging chemistries of cathode materials that could deliver more capacity with good thermal stability and long cyclability, where TiS_2,[10] $LiCoO_2$ [11] and a vast variety of cathodes were invented based on the solid-solution concept (i.e. $LiMn_2O_4$ (LMO),[12] $Li(Ni_xMn_yCo_z)O_2$ (NMC),[13] $LiFePO_4$ (LFP),[14] $LiNi_{0.5}Mn_{1.5}O_4$ (LNMO),[15] etc.). Figure 1.4 depicts the energy density vs specific energy in various cell chemistries, which clearly shows that enabling Si anode and Li metal anode is essential to realize an energy density over 1200 Wh/L and a specific energy over 500 Wh/kg, respectively.[9] Although Si and Li metal anodes stand out as ideal candidates owing to their high theoretical capacities,[7] issues arose with the promises of these materials. Silicon anode follows an alloying mechanism upon lithium insertion into its structure, which causes over 300% volumetric expansion. The impact of such drastic physical change is profound – silicon anode structure easily collapses during repeated volume expansion and shrinkage; newly exposed fresh surface of silicon anode is prone to react with liquid electrolyte to form solid electrolyte interphase (SEI) that leads to the consumption of limited lithium source and an increased cell impedance upon cycling[16]. Differing from the case of Si, Li metal anode suffers from a dendritic metal growth during Li metal plating, where Li ions travel from cathodes and nucleate on the bare current collector or pre-existing Li metal surface. Due to the hardly controllable mass transfer in a mixed liquid system[17], Li metal deposits tend to grow as dendrites, which may penetrate through the polymer separator to cause short-circuiting of battery and raise safety concerns[18]. On the other hand, batteries that utilize solid-state electrolytes might provide different perspectives for solutions.

1.3 All-solid-state battery

Employing an electrolyte material that is in solid state, all-solid-state batteries (ASSB) differ from liquid-electrolyte as they promote battery safety[19], exhibit a wide operational temperature window, and improve energy density by enabling Li metal as anode materials for next-generation lithium-ion batteries.[20,21] Figure 1.5 shows the schematic of an typical configuration of ASSB which contains a composite cathode, solid-state electrolyte (SSE) and Li metal anode.
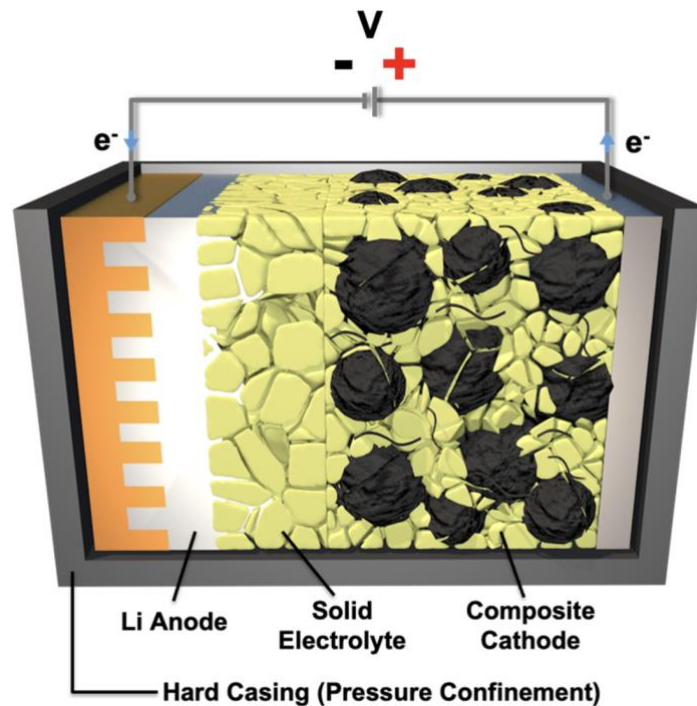
Figure 1.5 A schematic of all-solid-state battery with Li metal anode.[8]

A composite cathode consists of cathode particles and solid-state electrolyte (SSE) particles, along with binding materials and conducting agents.[8] The mixture of cathode with SSE is to increase the contact area so that lithium ion transport at cathode and SSE particle interface can be improved. The architecture of anode current collector shown in Figure 1.5 serves the similar idea but is more for enabling uniform Li nucleation and plating.

Despite the suitable mechanical properties to prevent Li dendrite penetration,[22] relatively wide electrochemical stability windows,[23] comparable ionic conductivities,[24] and intrinsic safety, most SSEs currently used in ASSB are found to be thermodynamically unstable against Li metal, where SSE decomposition produces a complex interphase, analogous to the SEI formed in liquid electrolyte systems. Conventional SSEs, including $Li_7La_3Zr_2O_{12}$, $Li_{1+x}Al_xGe_{2-x}(PO_4)_3$, $Li_{10}GeP_2S_{12}$, $Li_7P_3S_{11}$, $Li_{0.5}La_{0.5}TiO_3$ and lithium phosphorus oxynitride (LiPON) are predicted by DFT thermodynamic calculations to form SEIs upon contact with Li metal due its high reduction potential,[25,26] which have been validated by experimental findings in many cases.[27–33]
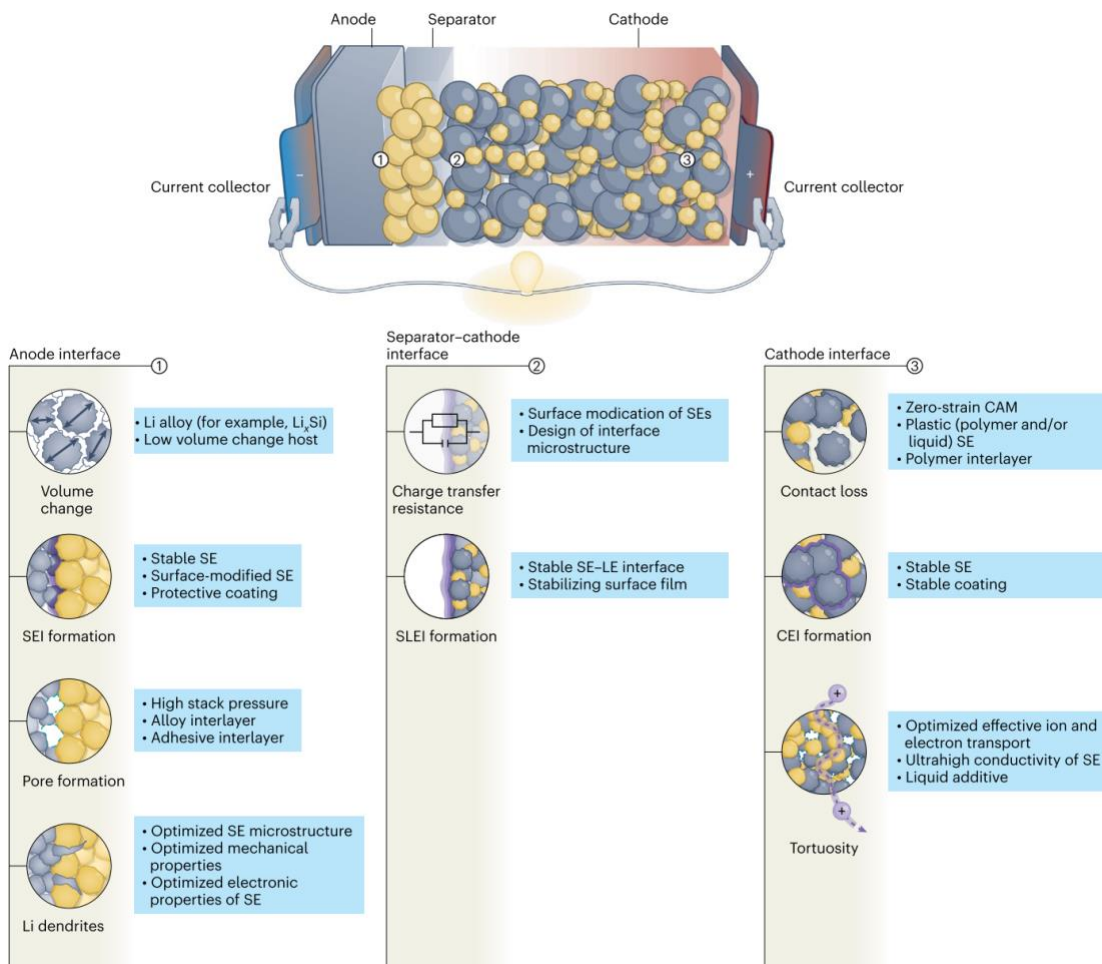
Figure 1.6 A schematic of ASSB showing the presence of various issues in different component and potential solutions to each issue.[34]

The nature of these decomposed phases governs the properties of the interface; an ideal passivation layer should consist of ionically conductive but electronically insulating components to prevent the SSE from being further reduced. However, in most scenarios such ideal interface is hard to obtain, which cause deleterious impact on the battery performance and eventually leads to the end of battery life. Figure 1.6 delineates all the existing issues in ASSB that include not only the interfaces (SEI, CEI, etc.) between different battery components, but also pore formation, contact loss and Li dendrite formation, etc. Strategies have been proposed to each of the listed issue. For instance, SEI/CEI layers could be potentially stabilized with the protective coating on electrode particles; pore formation could be mitigated via increasing the stacking pressure, adding interlayer, or introducing adhesives between the particles. However, due to the complexity of the ASSB system, one needs to pay extra attention to other characteristics of the system while modifying one single parameter. Moreover, as most of these existing issues are buried underneath the battery assembly, it remains extremely difficult to precisely locate the root cause of certain issue. In this case, an ASSB with a simplified configuration is needed to uncover the fundamentals behind the present issues in ASSB and shed light on future engineering directions, where thin film battery comes to the stage.

Chapter 2. Thin Film Battery

2.1 Overview of thin film battery

In the present lithium battery catalogue, ASSB provides improved safety and energy density over the liquid electrolyte counterparts, which therefore has garnered increased attention and research efforts.[35,36] Sharing a similar formulation concept, thin film battery (TFB) is one of the ASSBs that utilizes solid-state electrolyte and active electrode thin films produced via vacuum deposition techniques such sputtering, pulsed laser deposition, atomic layer deposition, etc., and
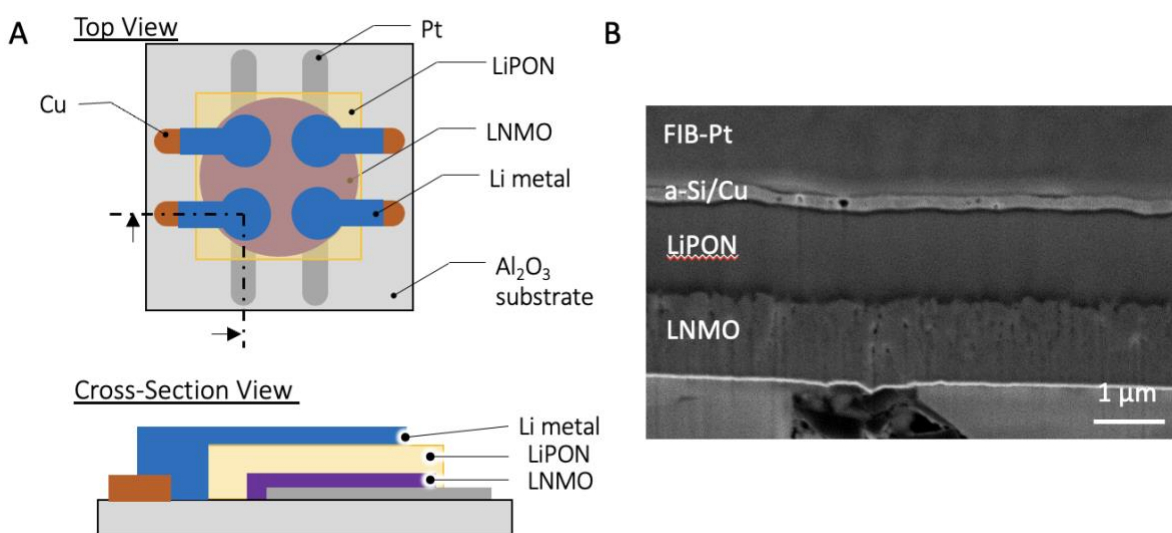
Figure 2.1 (A) Schematic of thin film battery that consists of a Li metal anode, LiPON electrolyte, and LNMO cathode on an alumina substrate. (B) A cross-section image showing the well-defined interfaces in TFB

was pioneered by Oak Ridge National Laboratory from 1992.[37,38] TFBs employing lithium phosphorus oxynitride (LiPON) SSE have demonstrated exemplary high-voltage compatibility (up to 5V) and remarkable capacity retention over thousand cycles.[39,40] TFB typically consists of layered architecture as shown in Figure 2.1A. Each layer is deposited by one specific technique and stacked together to form an electrochemical battery with a total thickness of less than 5 μm for the active materials. One major merit of TFB is its well-defined interface cell geometry, which

can serve as ideal platforms for fundamental research on interfaces and electrochemical behaviors within ASSB system (Figure 2.1B).[41,42]

2.2 Thin film deposition techniques

Despite the excellent battery performance and ideal platform for fundamental research, TFB fabrication can be costly due to the use of high vacuum environment and bottom-up process. A variety of physical vapor deposition (PVD) techniques have been optimized for TFB fabrication, including sputtering, pulse laser deposition and thermal evaporation.

2.2.1 Sputtering

Under high vacuum condition ($<10^{-4}$ Pa), sputtering process utilizes a glow discharge plasma that is generated by gas ionization under a strong electric field (Figure 2.2). The ionized gas species from working gas (i.e., Ar, O_2, or N_2), including atoms, ions, etc., are accelerated in the electric field toward a charged target material, where atomic bombardment transfers kinetic energy and leads to a physical ablation of the target material. There are numerous other energy exchanges inside the plasma, as secondary particles and negative ions are also emitted from the target along with radiation and local heating. The ablated atoms are then deposited onto a substrate, which may be biased and/or heated in the meantime for different purposes.
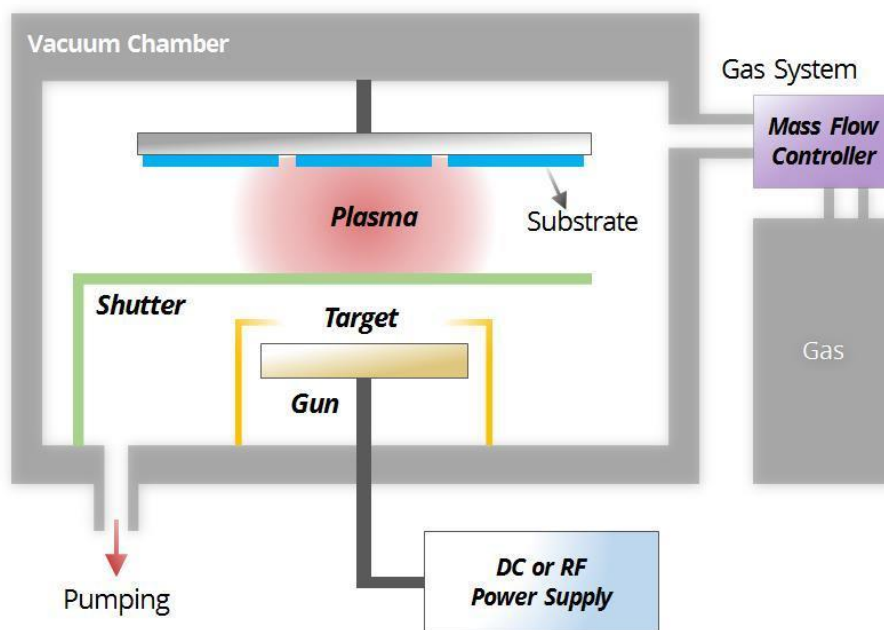
Figure 2.2 The schematic of DC/RF sputtering system[43]

Charge accumulation on the target surface occurs when there is excess charge due to the insulating surface, which can repulse the incoming ions and diminish the deposition efficiency. Therefore, direct current (DC) sputtering is commonly used for metal deposition, as no charge accumulation is present. However, for ceramic targets, radio frequency (RF) sputtering is employed to prevent such charge build up. To increase the sputtering yield with RF power source, magnetron sputtering is generally used, where the target is placed against a static magnetic field, confining ionized species toward the target surface. Sputtering is a good at transferring the target stoichiometry to the thin film.

2.2.2 Thermal evaporation

Thermal evaporation takes place in high vacuum chamber ($<10^{-5}$ Pa) where a solid material inside a heating boat is heated to its evaporation temperate through Joule heating, as shown in Figure 2.3. The vaporized particles travel through vacuum and then condense onto a substrate on

the top sample holder. Thermal evaporation takes advantage of decreased evaporation temperature at a low pressure and it's commonly used for simple substance such as Li metal, Au metal, Cu metal, etc.
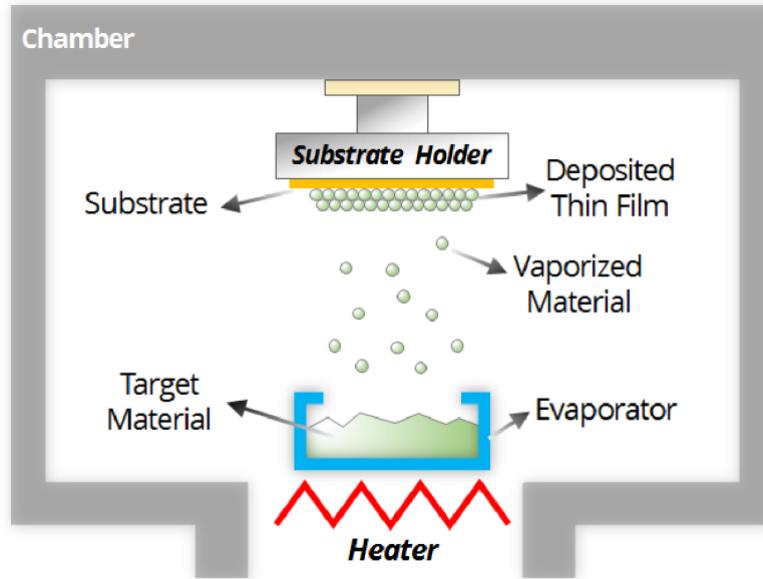
Figure 2.3 The schematic of thermal evaporation process[43]

2.2.3 Pulsed laser deposition

Pulsed laser deposition (PLD) is generally used for depositing complex materials. A high-power excimer laser (~2 J/pulse) is generated from the laser source and travels through a set of optical elements to reshape and focus. The focused laser beam on the target surface leads to physical ablation, after which the ablated species condenses onto the substrate (Figure 2.4). PLD can utilized either high vacuum environment or a gaseous environment to promote certain surface chemical modification.
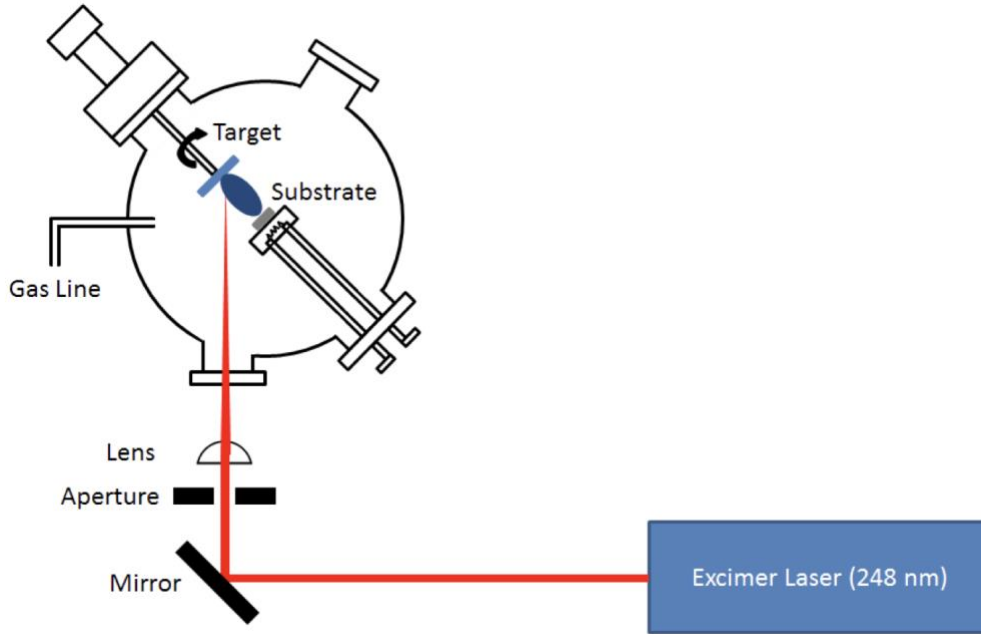
Figure 2.4 The schematic of pulsed laser deposition setup

2.3 Thin film battery manufacturing

The thin nature of cathode material in TFB determines that the energy stored in such cells falls short of the need in large devices such as electric vehicles, which shifts the direction of TFB development towards small electronics. Concurrently, miniaturizing electronics nowadays has been a trending direction due to the advancement in wearable and hearable technologies. Compact electrochemical energy storage components with small size that can be integrated to power the electronic system for the life of the device are increasingly needed at commercial scale.[44] TFBs serves as a solution as they offer significantly higher energy density and provides unparalleled processability with various form factors owing to its modifiable cell dimensions. However, current microbattery market requires technology and manufacturing breakthroughs at large scale to meet the higher volumetric energy density (VED). Common substrate materials for TFB fabrication include alumina, silicon, sapphire, mica etc. which are typically thick, rigid, electrically insulating,

brittle and expensive. These features lead to low VED, limited area form factor that confines such TFBs to niche applications with capacities in the range around 250 µAh, unsuitable for mAh-class applications.
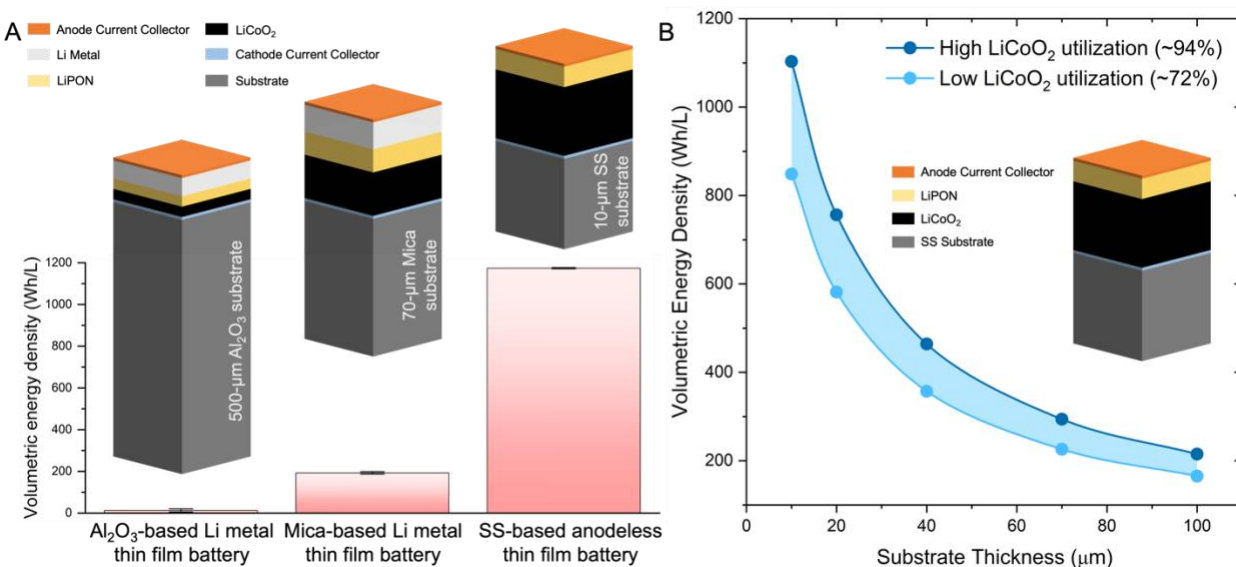
Figure 2.5 (A) Schematics of Li metal thin film batteries with different cell architectures and corresponding VEDs. (B) VEDs of SS-based anodeless TFB with varying SS thicknesses

Figure 2.5 depicts the VED of TFB with various cell configuration and materials. In depicted three cases, Li metal serves as anode material, LiPON serves as the SSE while LCO is the commercially available cathode. For commercial lab-scale production, $LiCoO_2$ thickness usually comes below 4 µm and common material such as alumina (Al_2O_3) is used as substrate, which in total gives relatively low VED due to the low cathode loading and high substrate volume;[39] In some of the commercially available TFB products, cathode thickness can be managed to reach around 7-10 µm.[45] Nevertheless, due to the use of Mica-based substrate that is over tens of µm thick, cell VED is limited to below 200 Wh/L, not to mention the wasted volume on packaging materials; To boost the VED, two solutions are favorable – employing anodeless configuration and redcuing the thickness of substrate. Note that a high utilization of thin film cathode capacity requires high temperature annealing of the cathode during or post deposition.

Therefore, a thin, high-temperature-compatible and low-cost substrate is needed, such as stainless steel (SS). As such, the third cell configuration in Figure 2.5A employs an anodeless setup and a thin SS substrate (10-μm thick), which can yield a VED up to 1168 Wh/L when a 10-μm-thick LiCoO$_2$ is used. Figure 2.5B further demonstrates the impact of substrate thickness on the VED of TFB. As SS substrate thickness increases from 10 μm to 100 μm, the corresponding entitlement VEDs drops from 1103 Wh/L to 215 Wh/L, stressing on the essence of utilizing thin substrates and getting high utilization of cathode. For benchmarking purpose, the state-of-art liquid electrolyte battery offers a VED around 450-700 Wh/L and ASSB can provides a VED about 900 Wh/L,[20,46,47] less than the amount that can be utilized from anodeless TFB, which gives it opportunity to largely improve the time of endurance for smart devices.
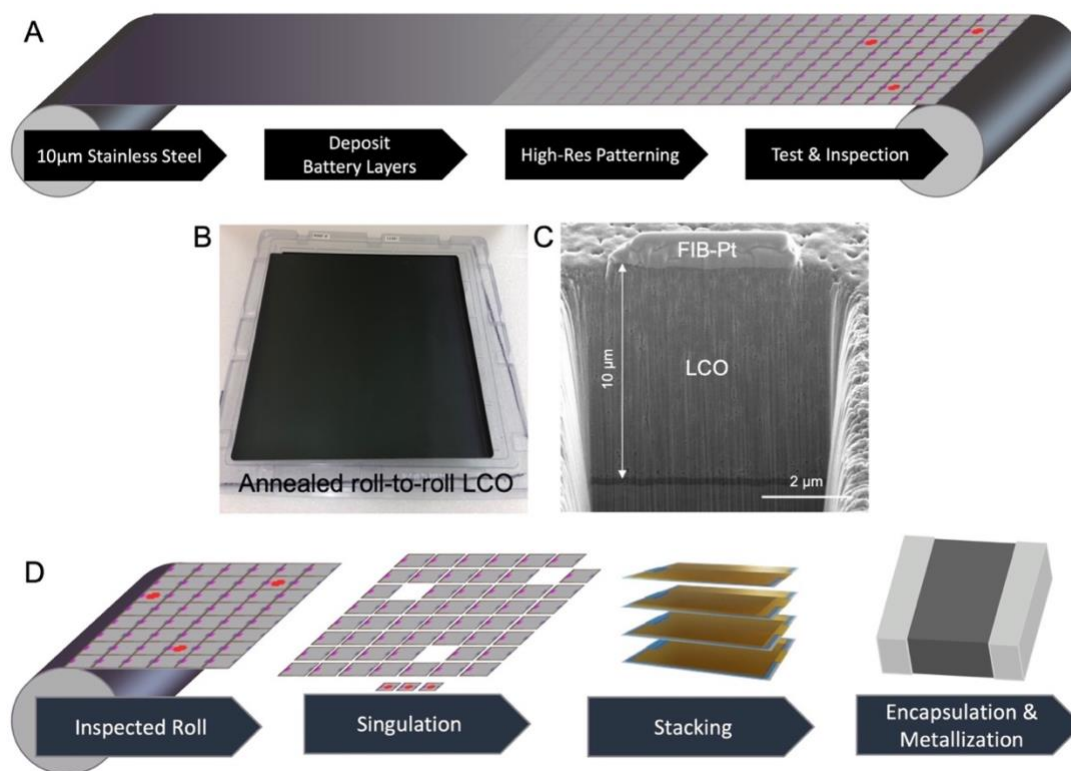
Figure 2.6 (A) Schematic of the high-throughput roll-to-roll deposition. (B) Photo of an annealed roll-to-roll LCO sheet. (C) Cross-section image of annealed roll-to-roll LCO. (D) Schematics of the dry-process manufacturing

In typical TFB fabrications, as most of the substrates are made of rigid solid materials, a roll-to-roll manufacturing process is not feasible. To overcome such problem, a high-throughput manufacturing process is demonstrated in Figure 2.6. Figure 2.6A shows the general procedure for high-throughput TFB manufacturing. After deposition, a single high-resolution patterning technique is applied to define and isolate the individual cells from the battery sheet, which subsequently go through impedance measurement for inspection. With deposition and annealing parameters well-tuned, such roll-to-roll process could produce high-quality LCO cathode as demonstrated in Figure 2.6B & C. Figure 2.6D shows the subsequent workflow after the impedance inspection, where each cell can be singulated from the whole sheet and go through a stacking process towards the encapsulation and metallization as the final product. Owing to the anodeless nature of such TFB, cell handling after singulation takes place in normal cleanroom environment, with no dry room needed, which further brings down the production cost. Such manufacturing process has been provided practical pathway to commercialized LiPON-based TFB in largr scale.

2.4 Lithium phosphorus oxynitride (LiPON): promises and challenges

Lithium phosphorus oxynitride (LiPON) is a thin film SSE that is conventionally deposited on solid substrates. LiPON was first reported by Bates et al. in 1992 by substituting 5%-8% of O with N in Li_3PO_4 by RF sputtering in nitrogen.[37] LiPON rapidly drew research attention in the solid state battery field as it exhibits exemplary cyclability with a vast choices of electrode materials, i.e., $LiCoO_2$,[48] $LiMn_2O_4$,[48] $LiNi_{0.5}Mn_{1.5}O_4$,[40] $Li_4Ti_5O_{12}$,[49] and Li metal,[40,48,49] etc. LiPON has enabled an ASS TFB with a Li metal anode and a high-voltage $LiNi_{0.5}Mn_{1.5}O_4$ (LNMO) cathode to achieve a capacity retention of 90% over 10,000 cycles with a Coulombic efficiency

17

over 99.98%.[40] As the timeline of LiPON development shown in Figure 2.7, many companies have inquired the license of LiPON patent and put solid efforts into its commercialization over the last three decades, including industrial giants such as ST Micro and Apple Inc. In the meantime, numerous research efforts have been undertaken to shed light on the structure and properties of the material itself and associated interfaces, for the sake of gaining knowledge regarding the stable nature and performance of LiPON, and providing guidelines to engineering other SSEs for next generation lithium rechargeable batteries.
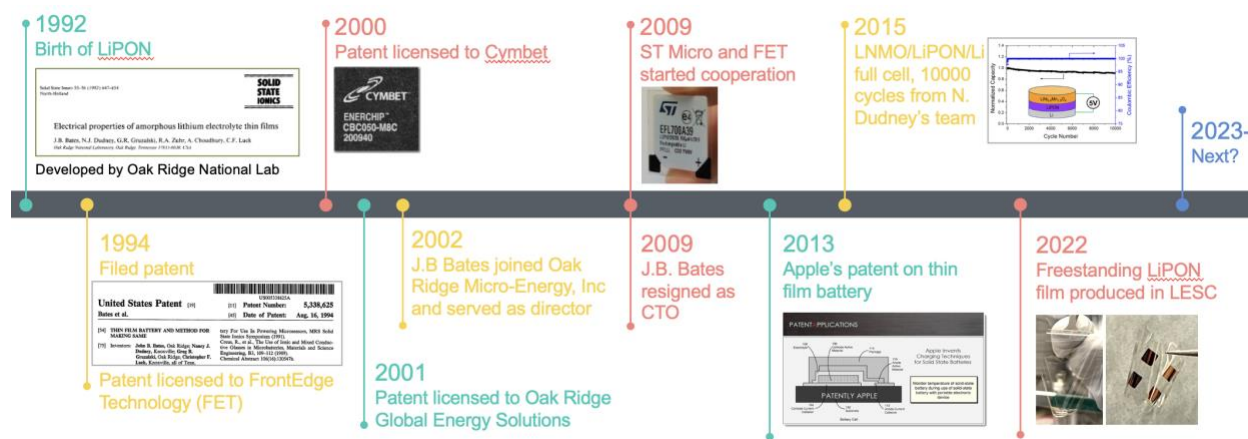
Figure 2.7 Timeline of LiPON development since 1992

Interpretation of the intrinsic properties of LiPON, nevertheless, has been disputed due to the amorphous nature of LiPON, its sensitivity to ambient environment, and the presence of solid substrate. One of the long-lasting debates pertains to the N bonding structure and its impact on the lithium transport properties in LiPON. Early studies on the chemistry of LiPON primarily relied on X-ray photoelectron spectroscopy (XPS), where two different N environments were identified and regarded as double-bridging N and triple-bridging N.[38,50,51] Such peak assignment was in part due to the pervasive belief that the cross-linked configuration introduced by N incorporation is the key for the ionic conductivity enhancement of LiPON over Li_3PO_4.[38] Alternative methods suitable

to probe local bonding environment such as neutron paired distribution function (PDF) and solid-state nuclear magnetic resonance (ss-NMR) were previously unable to validate this hypothesis due to the difficulty to obtain enough signal-to-noise (S/N) ratio, as the presence of substrates beneath LiPON thin film largely limits the active material amount that can be measured. Regardless, Lacivita et al. managed to obtain sufficient sample for neutron PDF measurements by scraping LiPON from the substrate and ruled out the existence of triple-bridging N, showing instead the prevalence of double-bridging N and apical-N bonding environments that was later verified with ss-NMR spectroscopy.[52,53] Regardless, new methods to characterize the native properties of LiPON material await breakthrough.

From the perspective of interface study, LiPON enabling stable cycling against Li metal and high-voltage LNMO cathode indicates the presence of extremely stable interphases between LiPON and electrode materials. The superior electrochemical performance of LiPON against Li metal has attracted numerous research efforts aiming to understand the underlying nature of stable Li/LiPON interphase. Computational efforts calculated the stability window of LiPON against Li metal to be from 0.68 V to 2.63 V, predicting decomposition products in this SEI as Li_3P, Li_2O and Li_3N.[54] Experimental efforts to identify this stable interphase of LiPON against Li metal, however, have been impeded by the limited characterization techniques available due to the low interaction volume of lithium, the amorphous nature of LiPON, and the extreme susceptibility of both lithium metal and LiPON to ambient air and probe damage.[55,56] Among the limited characterization methodologies, *in situ* X-ray photoelectron spectroscopy (XPS) conducted on LiPON thin films exposed to evaporated Li illustrated chemical change following Li deposition and identified the decomposition products at the Li/LiPON interphase to be Li_3PO_4, Li_3P, Li_3N and Li_2O.[31] Nevertheless, the structure and spatial distribution at nano-scale of these

decomposition products and their influence on interfacial stability remain unclear due to the nature of the buried interphase.

On the cathode interface side, Santhanagopalan et al. observed a lithium accumulation between LCO and LiPON upon repeated cycling, which impacts the ion transport at the interface and counts for irreversible capacity loss.[57] Later Wang et al. identified the cause of lithium accumulation as a disordered LCO formation at the LCO/LiPON interface, which continues to grow at an elevated temperature and leads to a further performance degradation.[41,45] All these research efforts shed light on possible degradation modes at the cathode/electrolyte interface. However, most of these effects are caused by structural change(s) within the cathode and not from LiPON decomposition. This contrasts starkly with the degradation mechanisms occurring in liquid analogues. The underlying mechanism that provides such exceptional stability remains elusive, largely due to a lack of available characterization tools that can access the buried interfaces and tackle the air-/beam-sensitivity of LiPON.[42]

In order to overcome the difficulty of characterizing both Li metal/LiPON interface and LNMO/LiPON interface, tools that can probe local structural or chemical information while mitigating potential damage from the probe source is urgently needed.

Chapter 2, in part, is a reprint of the material, as it appears in a manuscript that is being prepared to submit for publication: **D. Cheng**, K. Tran, S. Rao, Z. Wang, R. van der Linde, A. Kamath and Y. S. Meng, "Manufacturing Scale-Up of Anodeless Solid State Lithium Thin Film Battery for High Volumetric Energy Density Application", 2023. The dissertation author was the primary investigator and first author of this paper.

Chapter 3. Advanced Electron Microscopy for Battery Research

3.1 Overview of electron microscopy development

In 1931, Ruska and Max Knoll demonstrated the first TEM image on a platinum grid in Germany[58]. (Figure 3.1) Since then, TEM has been vastly applied throughout the material science field to identify crystal structures and diagnose material degradation at atomic scales. After decades of development, TEM began to flourish in the battery field by demonstrating its power to determine the structural change and chemical composition evolution in cathode materials to pinpoint the battery degradation mechanism, such as the generation of defects and disordering phase in $LiCoO_2$ cathode after electrochemical cycling[59] In stark contrast to cathode materials, anode materials and associated interphases are generally more prone to the chemical and structural changes by electron beam irradiation due to joule heating and radiolysis[56], while interphases might suffer additionally from electrostatic charging effects because of their insulating nature. To overcome the characterization barrier set by the beam intolerance and sizes, there has been a growing need to develop tools that can access nanoscale insights of beam sensitive Li metal, Li alloy and their SEIs with minimized beam interference.

New functionalities were then added on TEM in the structural biology field from 1970s. TEM was originally designed for imaging inorganic solids such as metal and oxides that have relatively high melting temperatures, strong chemical bonding, and resilience against high energy electron beam. For imaging biological samples to identify their molecular structures, researchers in structural biology field started to apply cryogenic protection for the beam-sensitive specimens. In early 1974, attempts to freeze the sample for protection under electron beam have enabled the collection of electron diffraction pattern of a catalase crystal after being frozen in liquid nitrogen[60]. (Figure 3.1) Advances in cryogenic methodology quickly evolved to the adoption of a method

Diffraction Pattern of a Catalase Crystal Frozen by Liquid Nitrogen

1931
First TEM
Developed by Ruska and Max Knoll in Germany.

First TEM Image Platinum Grid Magnification: 13

1974
First Cryo-EM
Sample protection against beam damage by freezing the sample

1982
Plunge Freezing
Sample protection against beam damage by vitrification.

Cryo-EM Image of Polystyrene Sphere Vitrified in Pure Water

1990
3D Reconstruction
Atomic structure of organic materials by electron crystallography

Ribbon Diagram of Bacteriorhodopsin reconstructed by Electron Diffraction

1998
Maximum-Likelihood (ML) Approach
Reduce the noise in single particle Cryo-EM images

Noise Reduction by ML Approach

2013
MicroED
3D tomography of nano-crystals by electron diffraction.

2017
First demonstration of Cryo-EM on Li metal anode without beam damage.

MicroED Structure of lysozyme at 2.9 Å Resolution

c) 120 e/Å² f) 120 e/Å²
500 nm   500 nm
296 K   110 K

The Stability of Li under e-beam at Different Temperatures

2019
Cryo-FIB
Prepare battery electrode lamella without beam damage.

The Stability of Li under ion-beam at Different Temperatures
296 K
100 K

Now
Deciphering the "Unknowns" in Battery Systems

Figure 3.1 An overview – a brief history of cryo-EM development.

named plunge freezing, during which the sample is frozen in amorphous ice by vitrification and can thus be protected. Such methods have enabled the TEM imaging of polystyrene spheres and

are still extensively used in structural biology field[61]. The three decades following this development witnessed the rapid growth in structural biology field with the emergence of advanced characterization toolsets, including 3D-reconstruction of organic material by electron crystallography[62], noise reduction of TEM images via machine learning approach[63] and 3D-tomography of nanocrystals[64]. (Figure 3.1) Such developments have made imaging beam sensitive biological materials and identifying their molecular structure at angstrom level a routine task, which amounts to the recognition by the 2017 Nobel Prize in Chemistry.

Concurrently, battery researchers realized that imaging anode materials can be potentially enabled by cryo-EM since anode materials are generally less susceptible to beam irradiation compared with biological samples. In 2017, two research groups in the United States adopted the sample preparation methodology and cryo-TEM instrumentation pioneered by the structural biology field, and successfully resolved the atomic structure of Li metal anode and its nanostructured SEI species.[56,65] Falling into the category of EM, another exemplary tool - cryogenic focused ion beam/scanning electron microscopy (cryo-FIB/SEM) has also been incorporated into battery field along with the introduction of cryo-TEM. This versatile tool provides large-area examination of the bean-sensitive materials that complements the local information obtained by cryo-TEM[66], and offers cryogenic protection during TEM lamella preparation so that imaging beam-sensitive solid-solid interfaces becomes possible[67]. Such an interdisciplinary transition of characterization tools had a profound impact to the direction of battery field development. Since the first adoptions of cryo-TEM and cryo-FIB/SEM to characterizing Li metal anode, there has been exponential growth in studies trying to implant cryogenic protection to investigate beam-sensitive material and interfaces within battery system, ranging from alkaline metal anodes[56,65,67–69], alloying anodes[70] to associated interfaces[42,67].

3.2 Cryogenic protection for beam-sensitive components in battery

3.2.1 Cryogenic-FIB/SEM characterization at bulk scale

Along with the adoption of cryo-TEM in the battery field, cryo-FIB/SEM has drawn much attention since its applications in both liquid and solid electrolyte (SE) systems (Figure 3.2A). As shown in Figure 3.2B, FIB/SEM utilizes high energy ions such as gallium (Ga) ion to mill certain amount of sample by designated patterns and depth, after which SEM is used to probe the freshly exposed surface or a lamella can be lifted out with the aids of a micromanipulator. However, due to the local heating and ion implantation during milling, beam sensitive materials such as Li metal suffer from morphological and chemical changes through the FIB process at room temperature[66]. To minimize such deleterious effects, cryogenic protection with the aid of liquid nitrogen is incorporated into FIB/SEM instrument to maintain sample at low temperature during operation, which has proven effective and critical for beam sensitive materials.

In detail, cryo-FIB/SEM works with a stage that is cooled down with nitrogen gas coming through a liquid nitrogen dewar (Figure 3.2B). Heat from the stage is constantly transferred to the carrier nitrogen gas so that stage temperature can be maintained around -180 ℃ to -170 ℃. This process guarantees that the sample stays at low temperature without the need of direct contact with liquid nitrogen, avoiding an undesired impact. In 2018, cryo-FIB/SEM was applied to examine the cross-sectional morphology of Li metal foil (Figure 3.2C). The cross section of commercial Li metal foil after room-temperature milling exhibits a porous structure with adequate amount of Ga implantation while the cryogenic-temperature milling well maintains the fully dense feature of commercial Li metal foil without noticeable Ga ion implantation, demonstrating the necessity of
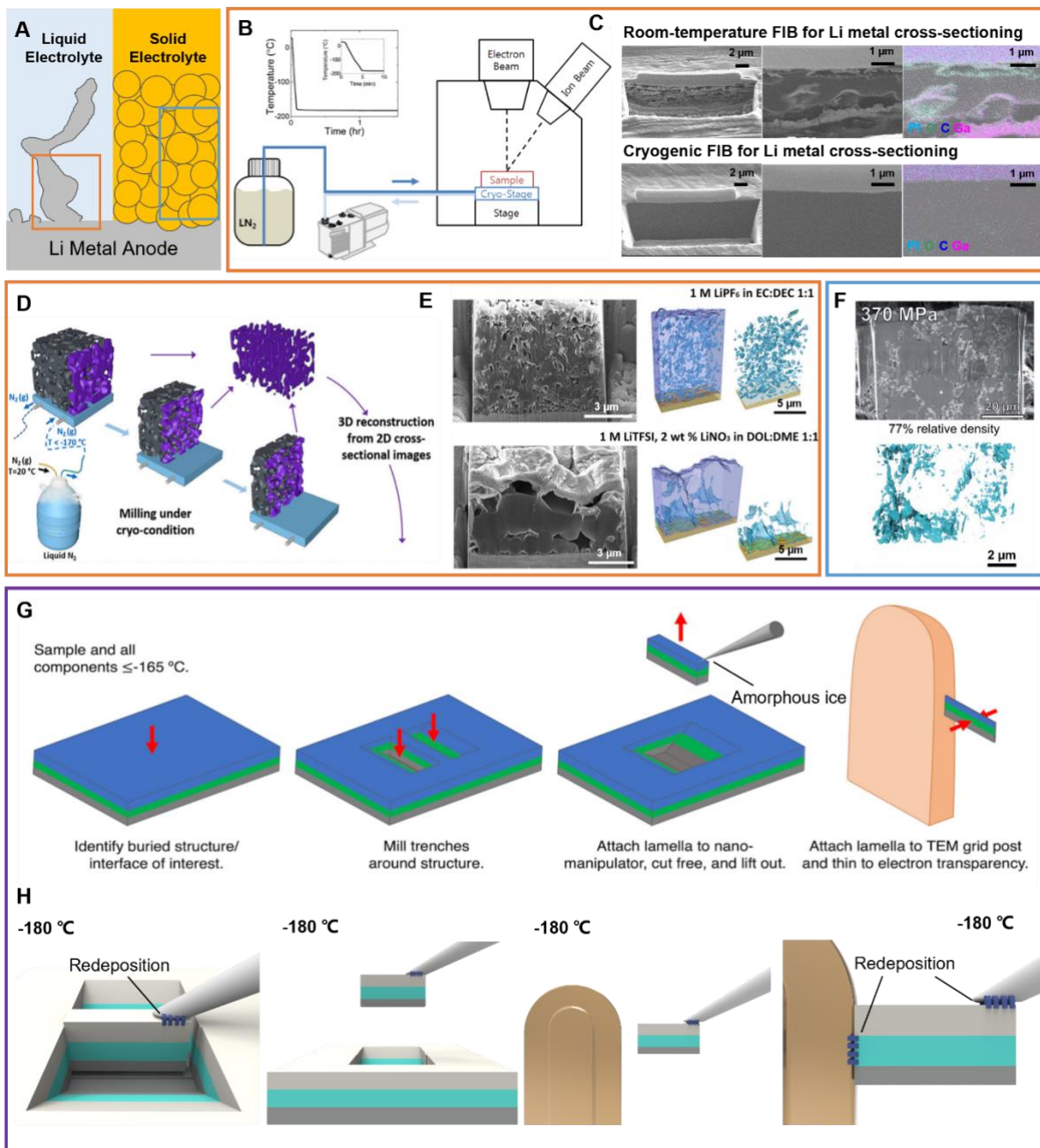
Figure 3.2 (A) Schematic showing Li deposits in liquid electrolyte and Li metal in contact with solid electrolyte. (B) Cryogenic FIB/SEM instrument configuration. (C) Li metal cross-sectional morphology and chemistry difference by room-temperature FIB and cryo FIB. (D) 3D models demonstrating the workflow of 3D reconstruction. (E) 3D reconstruction of Li metal in liquid electrolyte. (F) 3D reconstruction of solid electrolyte layer. Cryogenic TEM sample preparation methodology using amorphous ice (G) and redeposition material (H).

applying cryogenic temperature during FIB milling to preserve the pristine morphology and chemistry of beam sensitive materials such as Li metal[66].

Cryo-FIB/SEM further enables the 3D-visulization of the material by coupling sequential milling/imaging steps and analysis software (Figure 3.2D). Such techniques have enabled the examination of Li metal deposit structure in three dimensions, quantitatively determining important parameters such as porosity, surface area and components volume ratio that correlate with the performance of anode materials. Yang et al. applied cryo-FIB/SEM to reconstruct the structure of Li metal deposited in different electrolytes, where the porosity and tortuosity of Li metal deposits were found to be positively related to the electrochemical performance of the specific liquid electrolyte[71] (Figure 3.2E). Not limited to application in studying liquid electrolyte system, cryo-FIB/SEM has been confirmed effective for SE systems. (Figure 3.2F) 3D reconstruction of sulfide-based SE clearly unravels the internal structure of a pressed SE layer, building a relationship between the applied stacking pressure and the porosity of SE[72]. Such buried interfaces or bulk materials have remained unclear before the application of cryo-FIB/SEM, which adds up the missing yet critical knowledge for better understanding how electrolytes affect anode operation and how morphology is correlated to electrochemical performance.

To date, conventional Ga-ion FIB/SEM has been widely employed for battery materials development including interface/interphase characterization, 3D quantification and simulation analysis. However, materials removal efficiency of Ga-ion FIB/SEM limits its capability to access representative area and volume in some battery materials systems, e.g., electrode with tens of micron particle size. Recently, the emerging plasma FIB/SEM (PFIB/SEM) technology has been developed with different ion sources and high removal efficiency. It promises great potential for battery materials characterization by accessing representative 2D area and 3D volume via 40-time faster (than Ga^+ system) milling rate as well as enabling Ga-free sample preparation for alkali metal electrode through non-reactive ion source (Xe^+ and Ar^+ ion).

3.2.2 Cryogenic-FIB/SEM for TEM sample preparation

Due to the requirement of electron transparency, TEM samples are commonly prepared by FIB/SEM. Not limited to characterizing the bulk material from cross-sectioning and reconstruction, cryo-FIB/SEM gives a chance to beam sensitive materials for TEM examination. Differing from the room-temperature TEM sample preparation process in FIB, the common material, platinum, as the connection media between a lamella and a micromanipulator cannot be used at cryogenic temperature. To lift out the lamella from bulk sample at cryogenic condition then becomes an important step to bridge cryo-FIB/SEM preparation and cryo-TEM measurement.

There are two generally accepted methodologies for cryogenic liftout (cryo-liftout), as shown in Figure 3.2G & H. After the lamella is trenched from the bulk sample, a temperature-controlled micromanipulator needle is inserted and made contact with the top edge of the lamella. A gas-injection system then releases water vapor to designated patterns and region to form amorphous ice so that the lamella and the needle can be connected, after which the lamella is lifted out from the bulk sample and mounted on TEM grid applying the same method, ready for final cleaning and thinning[67].

Another liftout method utilizes the redeposition mechanism during the FIB milling process. When the sample is bombarded by incoming Ga ions, surface materials are sputtered away in the forms of atoms, ions and clusters from their original positions and flying around in vacuum.

Depending on ion beam intensity and sample geometry, a certain number of sputtered materials would redeposit on nearby surfaces in an amorphous form. When applying redeposition for cryo-liftout, the micromanipulator is parked at the top edge of the lamella, where a series of parallel cross-section milling patterns are used to mill the material from lamella so that it redeposits

around the pattern region and fills the gap so that the manipulator can be connected with the lamella (Figure 3.2H). After extracting the lamella from the bulk material, it is mounted on a TEM grid using the same protocol[42].

Amorphous ice is convenient and easier to apply as a connection material, however, there is a large chance that the reactive material itself such as Li metal can react with water vapor during the liftout process and lead to undesired surface chemical changes. To the contrary, redeposition method avoids the use of water vapor but uses the material itself for connection, which minimizes the impact of sample reactivity. Nevertheless, redeposition method requires experience and careful examination before it can be applied on the sample, giving rise to a larger chance of failure during cryo-liftout. Even so, both methods are compatible with TEM sample preparation that particularly needs cryogenic protection, which bridge cryo-FIB/SEM and cryo-TEM so that a bulk-to-nanoscale characterization on beam sensitive material becomes possible. so that a bulk-to-nanoscale characterization on beam sensitive material becomes possible. dvancing the understanding of beam sensitive electrodes and associated interfaces

3.3 Advancing the understanding of beam sensitive electrodes and interfaces

3.3.1 SEI and inactive components identification in metal anodes

In 2017, two groups first explored the possibility of applying cryo-EM to study Li metal and associated interphases. Li et al. demonstrated the atomic structure of Li metal that was electrochemically deposited on a copper mesh TEM grid[65]. (Figure 3.3A) Two distinct SEI structures are identified – multilayered and mosaic structure, both with nanocrystalline inorganic species embedded in an organic amorphous matrix, consistent with the long-existing SEI models proposed in 1980s and 1990s[73,74]. (Figure 3.3B) Wang et al. observed the nanostructure of

electrochemically deposited Li metal under cryo-EM and identified the existence of lithium

fluoride (LiF), a SEI component that has been proposed as one of the most important species[56].

Since the first introduction of cryo-EM to the battery field, Li metal research rapidly rejuvenated

owing to this new suitable tool that can access nanoscale insights on metastable phenomena of

beam sensitive components, enhancing the existing knowledge of electrochemically deposited Li

metal and associated SEI species while also challenging conventional perspectives on SEIs.

One of the famous debates that pertains to the dominating effects of SEI on Li metal anode

cycling performance is on the role of LiF, which is predicted to form and dominate in the SEI

when fluorinated electrolyte is used[75]. LiF is regarded as a species that facilitates the Li metal

deposition due to its high stability against Li metal and low electronic conductivity, however, the

low ionic conductivity of LiF cast doubts on if this species can improve the transport and kinetics

at the interphase during battery operation[42]. Further examination of SEI species on

electrochemically deposited Li metal shows the evidence of crystalline LiF in SEI[19] (Figure 3.3C).

Later Cao et al. used a fluorinated orthoformate-based electrolyte for Li metal deposition, where a

fully amorphous monolithic SEI on the order of 10 nm is identified on the surface of deposited Li

metal. Fluorine signal within such an amorphous layer is detected via energy dispersive

spectroscopy spectra (EDS)[76]. The improved electrochemical performance is claimed to be the

result of the formation of such fluorine containing amorphous SEI. However, dissent was proposed

soon by Huang et al., where they observe that LiF exists in a form of nanoparticle covered by

lithium oxide (Li_2O) and distributes near the bottom vicinity of Li metal dendrites. Elemental

mapping by scanning transmission electron microscopy/electron energy loss spectroscopy

(STEM/EELS) shows the absence of fluorine signal on the surface of Li dendrite[69], further

questioning the role of LiF for stabilizing SEI.
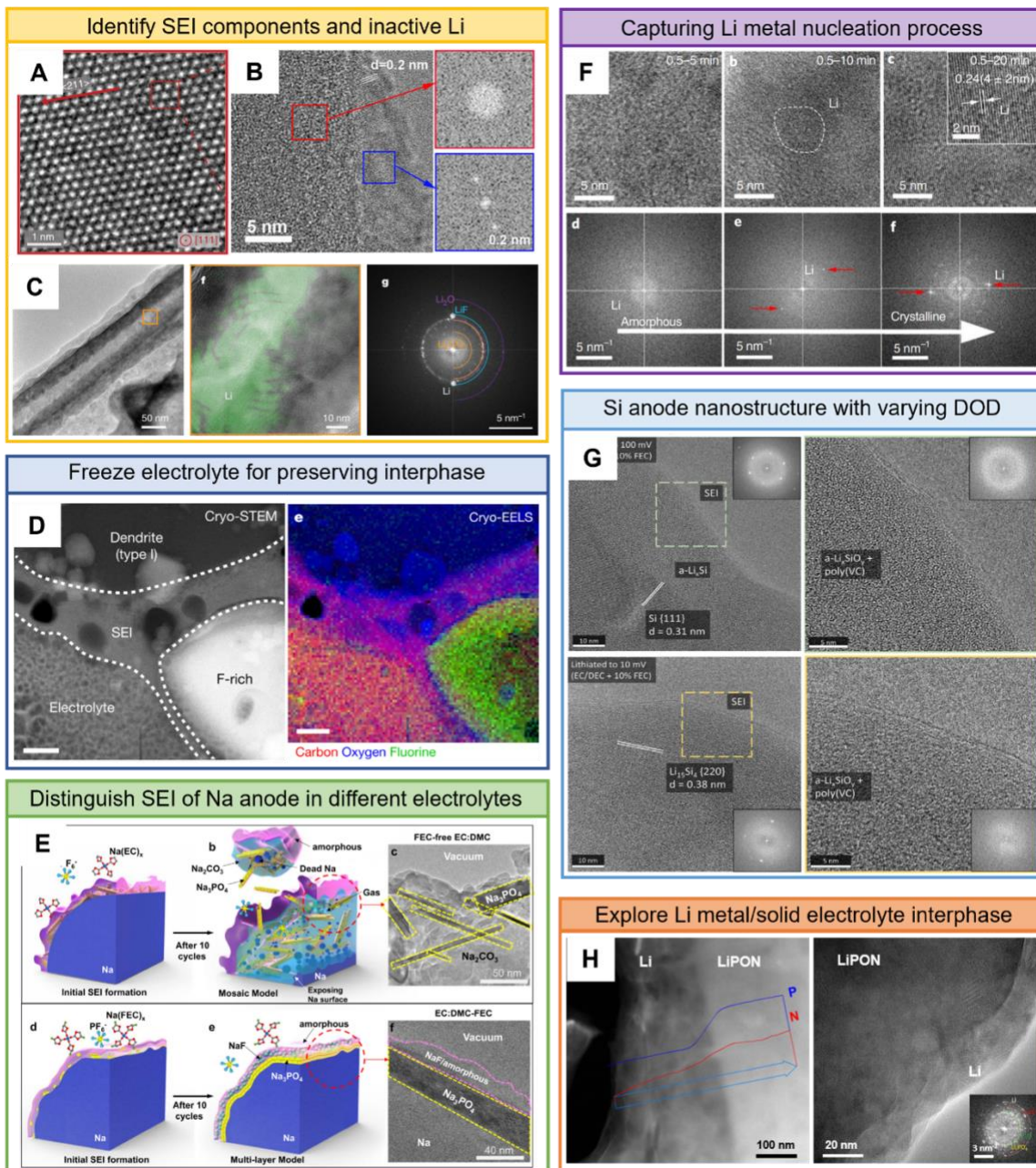
Figure 3.3 Cryo-EM for identifying (A) Li metal nanostructure, (B) SEI component and (C) inactive lithium distribution within Li dendrites. (D) Cryo-STEM imaging and EELS elemental mapping of Li metal within frozen electrolyte; (E) SEI components of Na metal anode in different electrolytes; (F) Li metal nucleation process captured by cryo-EM; (G) Si anode nanostructure at varying depth of discharge (DOD). (H) Li/LiPON interphase uncovered by cryo-STEM image, cryo-STEM-EDS linescan and cryo-TEM.

Besides the investigation on LiF, the existence and role of lithium hydride (LiH) species has also raised considerable debates in the field. LiH was first identified by Zachman et al. who

30

successfully preserved cycled Li metal anode with liquid electrolyte as a whole entity in its original configuration by freezing the coin cell and transferring to cryo-FIB/SEM[67]. Adopting 3D reconstruction in cryo-FIB/SEM and cryo-STEM/EELS, an extended SEI layer wrapping around Li metal dendrites is found, with a majority of oxygen signal detected (Figure 3.3D). Two types of Li dendrites with distinct sizes and morphologies are unraveled, where LiH is identified by EELS for the first time in Li dendrites. Nevertheless, another work from Fang et al. excluded the presence of LiH in either SEI or bulk Li deposits using titration gas chromatography (TGC) and residual gas analyzer.[19] The dispute regarding the existence of LiH also raised concerns on the LiF detection through TEM measurements by earlier literature since there is a chance that LiF and LiH species are mislabeled due to their similar lattice spacings[77]. Attempting to address the argument, Shadike et al. applied synchrotron-based X-ray diffraction and claimed both LiH and LiF species exist in SEIs[77]. Although more evidence is needed to have a solid conclusion on the presence of LiH and its impact on anode performance, LiH is proposed to form solid solutions with LiF and facilitate Li transport through interphases[77]. Such controversy has inspired increased research efforts on SEI, while prompting the battery community to look for ways to regulate cryo-EM data collection and interpretation by establishing standardized protocols to resolve the long-debating issues such as the role of LiF and LiH.

Another factor that closely correlates with the cycling performance of Li metal anodes is the formation of inactive lithium during cycling. Non-uniform SEI and Li deposits are produced due to the inhomogeneous Li metal nucleation and growth. Inactive lithium generates when non-uniform Li deposition and dissolution lead to the cleavage of thin Li deposits and electronically insulating SEI layers[78,79]. The loss of the electron pathway renders the Li metal wrapped within SEI unable to be dissolved as Li ions and make this portion of Li metal inactive, resulting in the

degradation of Li metal anodes. Cryo-EM also turns out to be a powerful tool to identify how the inactive lithium is distributed within Li deposits and how inactive lithium formation correlates with the performance of Li metal anode when coupled with TGC, further improving the understanding of the failure mechanism of Li metal anodes[19] (Figure 3.3C). Knowledge gained from cryo-FIB/SEM and cryo-EM examinations have shifted the focus of Li metal research from eliminating Li dendrite growth to suppressing the formation of inactive lithium on Li metal anode during battery operation.

Apart from Li metal batteries, new insights gained via cryo-EM also benefit other alkaline metal batteries, among which sodium (Na) batteries are now regarded as a promising technology particularly applicable in grid storage owing to the low cost of Na element and its abundance in earth crust. To enable the use of Na metal, a deep understanding of SEI formation on Na anodes is gained via exploring the effects of fluorinated ethylene carbonate (FEC) on the cycling behavior of Na metal anode. It is found that Na metal surface forms a multiplayer SEI structure containing sodium fluoride (NaF) and sodium phosphate (Na_3PO_4) when FEC is added into the electrolyte, exhibiting a higher stability compared with the SEI formed without FEC additive[80] (Figure 3.3E). To practically utilize the high theoretical capacity of metal anodes, new strategies to minimize SEI growth and regulate metal deposition await new insights to be unveiled by a wider adoption of cryo-EM, which is a trending for future.

3.3.2 Probing nucleation behavior of metal anodes

To resolve the non-uniform metal deposition that leads to the formation of dendritic metal growth and subsequent inactive components, a comprehensive understanding of metal nucleation process in the early stage is critically needed. Wang et al. applied cryo-TEM to look at the Li metal

nucleation process, where an amorphous-to-crystalline transition that can tuned by current density and types of liquid electrolytes was observed[81] (Figure 3.3F). Insights gained from such glassy metal formation at an early stage during Li metal deposition not only gives rise to new strategies on minimizing non-uniform Li metal plating, but extends the nucleation study on other metal species, i.e., Na, K, Mg and Zn. The similar glass formation discovered for these metals during deposition are distinct from common fast quenching process, calling for attention on electrochemically driven formation of metallic glasses that can be used for various applications. An alternative solution to regulate Li metal nucleation is the use of seeding layers that commonly include lithophilic metal species (i.e., Au, Ag) and metal compounds (i.e., MoS_2). Work performed by Tao group demonstrated the advantage of offering nucleation sites for Li metal deposition that results in homogenous growth of non-dendritic Li deposits[82,83].

Ideally, Li metal ought to nucleate uniformly on the surface of the current collector and grow homogeneously to form large granular Li deposits with a columnar structure. In the very beginning of Li metal nucleation, factors such as current densities, electrolytes or seeding layers could play an important role. However, on a microscale level, external parameter control turns out to be crucial in determining the nucleation behavior of Li metal. Deploying cryo-FIB/SEM to observe the Li deposition morphology in the presence of different uniaxial pressures during battery cycling, Fang et al. shows that a columnar Li deposit structure with large grain sizes is achieved when the cell runs under a pressure of 350 kPa, where Li metal tends to form more homogenous nucleates and evolves to a dense, low-tortuosity and uniform deposit layer regardless of current densities or electrolyte types. A Li metal reservoir with such characteristics is consequently important for uniform Li metal deposition[84]. This work puts forward a universal strategy that can potentially boost the cyclability of Li metal anode in practical use by tuning the morphology of Li

deposits to reduce SEI formation and inactive Li accumulation, which also provides a guideline and potential solutions for other metal anode deposition processes.

3.3.3 Progress in other anode systems

The ubiquity of cryo-EM as a powerful analytic tool is not monopolized by the metal anode field. Graphite material has long been adopted in commercialized products owing to its stability and modest capacity[7]. It is well known that graphite is incompatible with propylene carbonate (PC) electrolyte due to the exfoliation effects upon lithiation. Recently Han et al. found that graphite exfoliation occurs even with ethylene carbonate (EC) based electrolyte, a compatible analogue instead of PC, when an aggressive formation process is applied. Detailed analysis gained by cryo-EM sheds light on the importance of electrolyte additives such as vinylene carbonate and provides a mechanistic understanding of the impact of proper formation protocol on graphite anodes[85].

Promising for its high theoretical capacity, Si anode suffers from poor cyclability due to the drastic volumetric changes during lithiation and delithiation. An electrolyte additive FEC has been used for improving the cyclability while the underlying root cause remains elusive. Huang et al. deployed cryo-EM on Si anodes at different lithiation/delithiation states, where the SEI consisting of poly vinylene carbonate is found to be stable against oxidation and remains conformal after delithiation, contributing an enhanced cyclability[70] (Figure 3.3G). Recently He et al. further unveil the correlation between the structural and chemical evolution of Si and its SEI in three dimensions by integrating EDS tomography, cryo-STEM and an advanced algorithm, where SEI is shown to grow towards the interior of the Si electrode and form dead Si as a consequence of continuous void generation during the repeated delithiation processes[86].

The overview of anode study by cryo-EM emphasizes the importance for establishing appropriate protocols to protect beam sensitive anode materials during characterizations, featuring the vital role of cryo-EM on obtaining mechanistic understanding of complex metastable phenomena within anode materials.

3.3.4 New insights in cathode and associated interphases

Moving forward to the counter electrode in the battery system, cathode materials are generally more resilient under electron beam compared with anodes. Despite that cathodes have been intensively studied at atomic scale in the past few decades by normal-EM, with the ascending attention for interphase-controlled performance, cathode electrolyte interphase (CEI) also awaits rigorous research efforts. Due to the highly oxidative environment on the cathode surface during the charging process, most electrolytes decompose and form a thin layered material covering on the cathode. To access such a thin layer that is also air- and beam-sensitive, cryo-EM finds a way to explore the properties of CEI.

Alvarado et al. studied the impact of sulfone-based liquid electrolyte on the performance of high-voltage LNMO cathode using cryo-EM, where the CEI found in baseline electrolyte exhibits a non-uniform coverage on LNMO surface, increasing the chance of cathode surface being exposed to fresh electrolyte and consuming Li source. However, the CEI found in the advanced electrolyte demonstrates a conformal coverage on LNMO particles with an evenly distributed thickness around 0.612 nm, well correlated with the improved electrochemical performance[87]. An analogous reduced CEI thickness and uniform CEI coverage on $LiNi_{0.6}Mn_{0.2}Co_{0.2}O_2$ (NMC) cathode have also been identified by Yang et al. when coupled with a liquid gas electrolyte system[88]. In another study by Zhang et al., the NMC cathode particle forms a uniform CEI layer

35

after an electrical shorting treatment at pristine state, leading to an improved capacity retention and reduced cell impedance[89].

Apart from solely demonstrating the morphology of CEI layers, cryo-EM also helps to identify the CEI species for sulfurized polyacrylonitrile (SPAN) cathode. In an ether-based liquid electrolyte system with lithium nitrate ($LiNO_3$) additive, the CEI formed on SPAN particle consists of LiF and lithium nitrite ($LiNO_2$), believed to be the key for the enhanced cyclability of SPAN cathode[90].

New insights on cathode study by cryo-EM have drawn more attention to the interphase-pivoted electrochemical performance. Nevertheless, compared with anode systems, the uniqueness of cryogenic protection for cycled cathodes has not been well acknowledged in the literature. Detailed imaging parameter control such as electron dose needs to be well documented depending on the types of cathodes and state of charges, since highly charged cathodes exhibit a much higher beam sensitivity and chemical reactivity. Without proper protection, the electron beam especially under scanning mode can induce phase transformation of the cycled cathode materials more than the electrochemical cycling itself.

3.3.5 Accessing buried solid-solid interfaces

Unlike solid-liquid interface that is more convenient to access, solid-solid interface in batteries is generally difficult to characterize due to its buried nature and equally high reactivity to ambient and beam irradiation. In the case of all solid-state battery, a complex interface commonly forms between Li metal and SEs due to chemical or electrochemical incompatibility. Among common SEs, oxides are generally more beam tolerant, which enables high-resolution STEM imaging of their crystal structures and interphases with metal anode[91–94]. In contrast, other SEs

made of sulfides, halides, nitrides and polymers are prone to beam damage due to their intrinsic properties such as low electronic conductivity or weak chemical bonding. The formation of electrically insulating species upon decomposition between SEs and Li metal adds on difficulties for probing such solid-solid interfaces. Cryogenic protection turns out to be a solution for probing some of the SEs. Besides Li/LiPON system, the solid-solid interface between Li metal and a polymer SE, poly(ethylene oxide) (PEO) has also been investigated by cryo-EM. Sheng et al. unveils a Li/PEO interface comprising nanocrystalline Li_2O, $LiOH$, and Li_2CO_3 species that are incorporated inside an amorphous phase[95]. The polycrystalline features of Li metal in the vicinity of PEO indicates the drastic thermodynamic instability that could lead to side reactions and increased cell impedance. A mitigation strategy is then proposed by adding Li_2S to prevent the continuous reaction between Li metal and PEO. By coupling cryo-EM, XPS and computational methods, Li_2S is shown to accelerate the decomposition of $LiN(CF_3SO_2)_2$ (LiTFSI) that gives rise to a LiF-rich interphase between Li metal and PEO, which stabilizes the polymer electrolyte and enhances the ion transport properties[95].

The introduction of cryo-EM technologies in the different branches of battery research undoubtedly revived the efforts of achieving a practical metal anode battery with better cathodes for higher energy density and prolonged cyclability. Cryo-EM is the key to uncover the unknowns at LiPON-associated interfaces in TFB.

Chapter 3, in full, is a reprint of the material, as it appears in: **D. Cheng**, B. Lu, G. Raghavendran, M. Zhang and Y. S. Meng, "Leveraging Cryogenic Electron Microscopy for Advancing Battery Design", *Matter*, 2022, 5, 26–42. The dissertation author was the primary investigator and first author of this paper.

Chapter 4. Unveiling the Stable Nature of the Solid Electrolyte Interphase between Lithium Metal and LiPON via Cryogenic Electron Microscopy

The solid electrolyte interphase (SEI) is regarded as the most complex but the least understood constituent in secondary batteries using liquid and solid electrolytes. The dearth of such knowledge in all-solid-state battery (ASSB) has hindered a complete understanding of how certain solid-state electrolytes, such as LiPON, manifest exemplary stability against Li metal. By employing cryogenic electron microscopy (cryo-EM), the interphase between Li metal and LiPON is successfully preserved and probed, revealing a multilayer mosaic SEI structure with concentration gradients of nitrogen and phosphorous, materializing as crystallites within an amorphous matrix. This unique SEI nanostructure is less than 80 nm and is stable and free of any organic lithium containing species or lithium fluoride components, in contrast to SEIs often found in state-of-the-art organic liquid electrolytes. Our findings reveal insights on the nanostructures and chemistry of such SEIs as a key component in lithium metal batteries to stabilize Li metal anode.

4.1 Introduction

The past four decades have witnessed intensive research efforts on the chemistry, structure, and morphology of the solid electrolyte interphase (SEI) in Li-metal and Li-ion batteries (LIBs) using liquid or polymer electrolytes, since the SEI is considered to predominantly influence the performance, safety and cycle life of batteries.[75,96–100] Pioneering work by Peled *et al.*[74] and Aurbach *et al.*[73] has independently proposed two widely accepted SEI models – a mosaic SEI and a multilayer SEI – to explain the structural and chemical evolution mechanism during the SEI formation. Regardless of the structural difference in the models, consensus is that most SEIs in

organic liquid or polymer electrolytes are comprised of both inorganic species that are thermodynamically stable against Li metal and organic species that are partially reduced by Li metal.[73,74] A recent study using tip-enhanced Raman spectroscopy investigated the nanoscale distribution of the organic species in the SEI formed on amorphous silicon.[101] Although the studies on SEI chemistry and morphology formed by using various electrolyte compositions and electrode materials have been well documented in literature, existing models still require further efforts to be truly validated in terms of the distribution of nanostructures within the SEI layer. The dearth of SEI studies for solid-state electrolytes (SSE) also leaves the SEI formation mechanism at the Li/SSE interphase elusive.

Originating from the structural biology field, cryogenic focused ion beam (cryo-FIB) and cryogenic electron microscopy (cryo-EM) have recently been introduced to battery research, and have proven the ability to preserve and probe Li metal for quantitative structural and chemical analysis.[56,102,103] Li *et al.* observed different nanostructures in SEIs formed in standard carbonate-based electrolyte and fluorinated-carbonate-based electrolyte respectively by using cryo-EM. They hypothesize that the enhanced electrochemical performance using fluorinated electrolyte is attributed to the formation of a multilayer SEI structure, in contrast to the mosaic SEI structure formed with standard carbonate-based electrolyte, which stressed the competing impact of SEI nanostructure versus SEI chemistry for stabilizing Li metal anodes.[104] Further, Cao *et al.* observed a monolithic amorphous SEI in electrolyte that contains highly-fluorinated solvents. The homogeneous and amorphous features of this SEI was proposed to be the key for the largely improved Coulombic efficiency and dense Li plating.[76] These findings highlighted the importance in investigating the SEI nanostructure formed in liquid electrolytes, and also

prompted cryo-EM-based examination of the SEI in ASSBs, which can provide missing yet critical insights on how to build a stable interphase between SSE and Li metal.

Given the susceptibility of LiPON and Li under electron beam exposure,[56,105] herein we combined cryo-FIB and cryo-EM to preserve the Li/LiPON interphase and characterize its chemistry and structure. We observed concentration gradients of nitrogen and phosphorous into Li metal, and a <80 nm thick interphase consisting of a distribution of crystalline decomposition products embedded within an amorphous matrix. The observed structural and chemical evolution across the interphase identifies the SEI components to be Li_2O, Li_3N and Li_3PO_4, with a unique multilayer-mosaic distribution, confirmed by XPS depth profiling. The observed distinct SEI components (Li_3N and Li_3PO_4) are compared with the SEI in liquid systems and the multilayer-mosaic distribution sheds light on their positive effect on stable Li metal cycling. According to these findings, we propose a formation mechanism of the interphases and discuss how this type of SEI facilitates stabling cycling against Li metal.

4.2 Experimental Methods

4.2.1 Sample preparation

LiPON thin film was deposited on $Pt/Cr/SiO_2/Si$ substrate by radio-frequency (RF) sputtering using a crystalline Li_3PO_4 target (2″ in diameter, from Plasmaterials, Inc.) in UHP nitrogen atmosphere. Base pressure of the sputtering system was 3×10^{-6} Torr. LiPON deposition used a power of 50W and nitrogen gas pressure of 15 mTorr. The as-deposited LiPON thin film was 1 μm in thickness with a growth rate of ~0.46 Å/min. Ionic conductivity of as-deposited LiPON thin film was measured by electrochemical impedance spectroscopy (EIS) to be 3×10^{-6} S/cm, similar to that in literature.[55] After RF sputtering, LiPON thin film was transferred with

environmental isolation from the sputtering chamber to thermal evaporation chamber to minimize air exposure and prepare for lithium metal deposition. Lithium metal thin film was evaporated on LiPON in a high-vacuum chamber with a base pressure lower than 3×10^{-8} Torr. Growth rate and film thickness of the lithium metal were monitored by a quartz crystal microbalance (QCM). The average evaporation growth rate was calibrated to be ~1.53 Å/s. Film thickness was controlled by deposition rate and deposition time. For the full cell fabrication, LNMO cathode was first deposited on Pt-coated (100 nm thick) alumina substrate by pulsed laser deposition (PLD) using a Lambda Physik KrF Excimer laser. Laser fluence and repetition rate were set at ~2J cm^{-2} and 10 Hz. During deposition, substrate temperature was 600°C and oxygen partial pressure was controlled at 0.2 Torr. LNMO film had a thickness of 650 nm with an active area of 4.9 mm^2 and an active mass of ~0.013 mg. Active material loading is 0.03 mAh/cm^2. LiPON solid electrolyte and Li metal anode were subsequently deposited following the procedures above. The thickness of Li metal anode was 570 nm, which corresponded to 203% excess capacity compared to that of cathode.

4.2.2 Liquid cell fabrication

The materials were all purchased from vendors without any further treatment. The electrode was casted on the Al foil by the doctor blade method. The ratio of active material (LNMO, Haldor Topsoe), conductive agent (SPC65, Timical) and binder (PVDF HSV900, Arkema) was 90:5:5, the electrode was dried in the vacuum oven overnight after casting. Active material loading is 0.65 mAh/cm^2 (~4.5mg/cm^2). The size of the electrode was 12.7mm as the diameter, the coin cell type was CR2032. 50 μL electrolyte (1M LiPF6 in EC:EMC=3:7 wt%), one piece of Celgard

2325 separator and Li metal chip were used. As for the testing protocols, two cycles at C/10 (1C = 147 mA/g) were applied and rest cycles were conducted at C/3.

4.2.3 Electrochemical measurement

Thin film full cell was cycled between 3.5 V and 5.1V using a Biologic SP-200 low current potentiostat. A constant current of C/10 was applied at the 1st, 2nd and 535th cycle. A constant current of 5C was applied during the rest of cycles.

4.2.4 Cryogenic focused ion beam/scanning electron microscopy (cryo-FIB/SEM)

A FEI Scios DualBeam FIB/SEM equipped with cryo-stage was used to observe the surface and cross-section morphology of Li/LiPON sample and prepare for TEM sample. The operating voltage of electron beam was 5 kV. Emission current of electron beam was set to 25 pA to minimize potential damage of electron beam on Li/LiPON sample surface and cross-section. An argon ion beam source was used to mill and thin the sample. The operating voltage of ion beam source was 30 kV. Different emission currents of ion beam were chosen for different purposes, i.e. 10 pA for imaging by ion beam, 0.1 nA for cross-section cleaning/lamella thinning and 3 nA for pattern milling. To preserve the Li/LiPON interphase during TEM sample preparation, cryo-stage was used during pattern milling, cross-section cleaning and lamella thinning processes, where the temperature of cryo-stage was maintained at around -185°C due to heat exchanging with cooled nitrogen gas.

4.2.5 Cryogenic lift-out methodology

Conventional cryo-FIB preparation process requires the stage and sample to cool down and remain stable at liquid nitrogen temperature before further milling or thinning, which alone approximately consumes at least 1.5 hour and about 5 liters of liquid nitrogen. Pt deposition was required to connect lamella with the tungsten probe for lamella lift-out and mounting, which could not be performed due to the inability to heat Pt source under cryogenic temperature (around 100K). To avoid repeatedly cooling and warming the stage during Li/LiPON TEM sample preparation, we applied a cryo-lift-out methodology by using redeposition, which has essentially improved the work efficiency and saved research resources. Figure 4.2 demonstrates the methodology to complete a cryo-lift-out without Pt deposition at liquid nitrogen temperature, which saves 3-4 hours for each TEM sample preparation.

4.2.6 Cryogenic (scanning)/transmission electron microscopy (cryo-S/TEM)

The Li/LiPON interphase lamella for cryo-EM observation was extracted from a separate deposition, which was comprised of Li metal, LiPON and substrates. The Li/LiPON lamella was transferred from the FIB chamber under vacuum using an air-free quick loader (FEI), and stored in an Ar purged glovebox. STEM/EDS line scan results and TEM images were recorded on a JEOL JEM-2800F TEM, equipped with a Gatan Oneview camera operated at 200 kV. A single-tilt liquid nitrogen cooling holder (Gatan 626) was used to cool the samples to approximately -170℃ to minimize electron beam damage where the TEM grids were sealed in heat-seal bags and transferred to TEM column using a purging home-made glovebox filled with Ar gas. STEM/EELS results were obtained on a JEOL JEM-ARM300CF TEM at 300 kV. A TEM cryo-holder (Gatan) was used to load the sample where TEM grids were immersed in liquid nitrogen and then mounted

onto the holder via a cryo-transfer workstation. The whole TEM sample preparation and transfer process guaranteed minimum contact of Li metal with air.

4.2.7 X-ray photoelectron spectroscopy

X-Ray photoelectron spectroscopy (XPS) was performed in an AXIS Supra XPS by Kratos Analytical. XPS spectra were collected using a monochromatized Al Kα radiation (hυ = 1486.7 eV) under a base pressure of 10^{-9} Torr. To avoid moisture and air exposure, a nitrogen filled glovebox was directly connected to XPS spectrometer. All XPS measurements were collected with a 300×700 µm^2 spot size. Survey scans were performed with a step size of 1.0 eV, followed by a high-resolution scan with 0.1 eV resolution, for lithium 1s, carbon 1s, oxygen 1s, nitrogen 1s, and phosphorous 2p regions. A 5 keV Ar plasma etching source was used for depth profiling with a pre-etching for 5 s, etching for 60 s and post-etching for 10 s. All spectra were calibrated with adventitious carbon 1s (284.6 eV) and analyzed by CasaXPS software.

4.2.8 Cryogenic X-ray Diffraction

The powder crystal X-ray diffraction was carried out on a Bruker micro focused rotating anode, with double bounced focusing optics resulting in Cu $K_{\alpha 1}$ and $K_{\alpha 2}$ radiation ($\lambda_{avg} = 1.54178$ Å) focused at the sample. A sample of LiPON was mounted onto a four circle Kappa geometry goniometer with APEX II CCD detector. The sample was cooled and data were collected in a nitrogen gas stream at 100 K.

4.2.9 Electron Energy Loss Spectroscopy Simulation

Electron energy loss spectroscopy simulations were conducted using FEFF9 software. The crystal structures used included a Li_2O cif file (ID #22402), a Li_3PO_4 cif file (ID # 77095) and a Li_3P cif file (ID # 240861) taken from ICSD database. The amorphous LiPON structure was generated by AIMD. The simulation parameters for FEFF9 included beam energy of 200 keV, collection and convergence angles of 10 mrads, xkmax value of 4, xkstep value of 0.02 and estep value of 0.01. Hedin Lundqvist exchange and RPA corehole were used for electron core interactions in FEFF9.

4.2.10 Calculation of Diffusion Barriers in Li Metal

Density functional theory (DFT) calculations were performed using the generalized gradient approximation (GGA)[106] approximation, and projector augmented-wave method (PAW)[107] pseudopotentials were used as implemented by the Vienna Ab initio Simulation Package (VASP)[108,109]. The Perdew-Burke-Ernzerhof exchange correlation[110] and a plane wave representation for the wavefunction with a cutoff energy of 450 eV were used. For calculations of diffusion in Li metal, the Brillouin zone was sampled with a k-point mesh of 5x5x5 for both structural relaxations and nudged elastic band (NEB)[111] calculations. NEB calculations were performed placing dopant ions in interstitial locations of a 128 Li atom unit cell and interpolating 5 intermediate images.

4.3 Results

4.3.1 Electrochemistry and a methodology for interface sample preparation

The presence of a stable interface between Li and LiPON was first demonstrated by a thin film battery consisting of a high-voltage spinel LNMO cathode, a LiPON solid electrolyte and a Li metal anode. Figure 4.1A shows the representative voltage curve of LNMO cathode. The
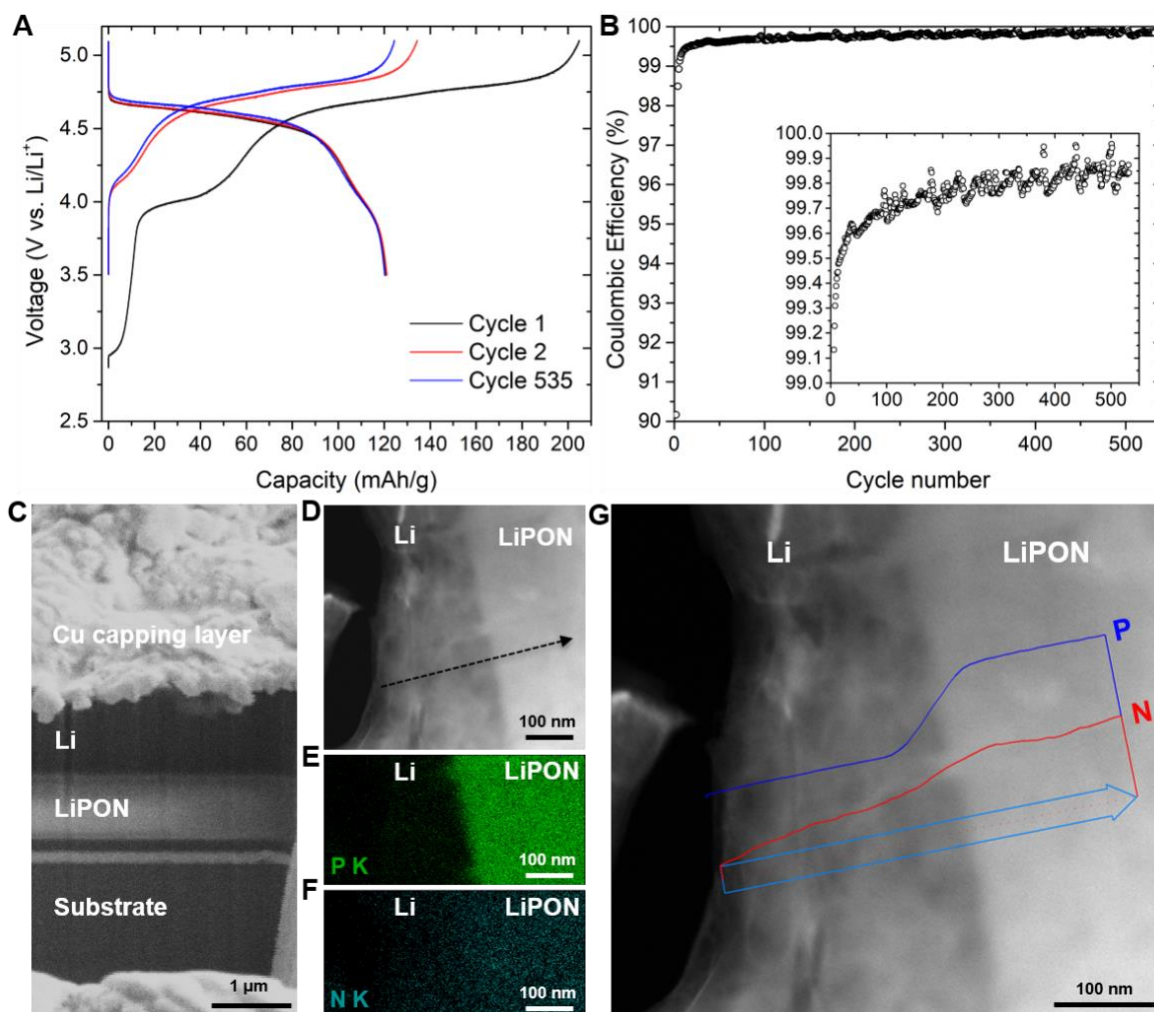
Figure 4.1 Electrochemical performance of Li/LiPON/LNMO full cell and cryo-STEM EDS results. (A) The voltage profiles of the 1st, 2nd and 535th cycle. (B) The Coulombic efficiency change with cycle numbers over 500 cycles. (C) Cryo-FIB-SEM cross-sectional image of the Li/LiPON sample. (D) Cryo-STEM DF image of Li/LiPON interface. EDS mapping results of P (E) and N (F) signals in the region shown in (D). (G) EDS line-scan of P and N signals (counts per second) along the black dashed arrow in (D). P and N signals were normalized respectively and plotted along the arrow to show the concentration gradient across the interface.

discharge capacity did not experience obvious degradation after 535 cycles at a charge/discharge rate of 5C. Figure 4.1B displays the Coulombic efficiency (CE) change as cycling proceeded, where the CE was stabilized beyond 99.70% after 100 cycles and 99.85% after 400 cycles, which is much better than liquid cell equivalents. The excellent electrochemical cycling of this full cell not only confirmed the superior cyclability of LiPON against Li metal anode, but also rendered us eligible to further investigate the nature of this stable interfaces within this battery.

To access a buried interface and elucidate its significance for long-term stable cycling, a combination of FIB and TEM was used, as proven effective to explore many interfacial phenomena.[41,45,57,112] Considering the high reactivity and beam sensitivity of both Li metal and LiPON, cryogenic protection is necessary to minimize the potential damage and contamination during sample preparation, transfer, and imaging. [19,56,66,71] Here, we have applied a method of transferring a lamella from the bulk sample to the FIB grid in order to avoid the contamination from organometallic Pt or amorphous ice, both of which have been used as bonding materials in FIB.[66,67] Conventionally, organometallic Pt is deposited to attach the lamella to the nano manipulator, which is then transferred to a FIB grid.[66] This process is generally performed at room temperature, but is impeded under cryogenic temperature due to the condensation of organometallic Pt vapor. Alternatively, Zachman *et al*. used water vapor as a connection material, which condenses to amorphous ice in cryo-FIB.[67] Note that both Pt and water can react with Li causing potential damage and artifacts to the Li/LiPON interphase. Therefore, we applied a re-deposition mounting methodology in the cryo-FIB, where the etched Li metal material was trapped and redeposited at the gap between lamella and manipulator or FIB grid as the connection material. Details of this methodology can be found in Figure 4.2. In this way, no extra materials were

introduced while conducting the cryo-lift-out for preserving and preparing well-defined Li/LiPON interphases for study in this work.
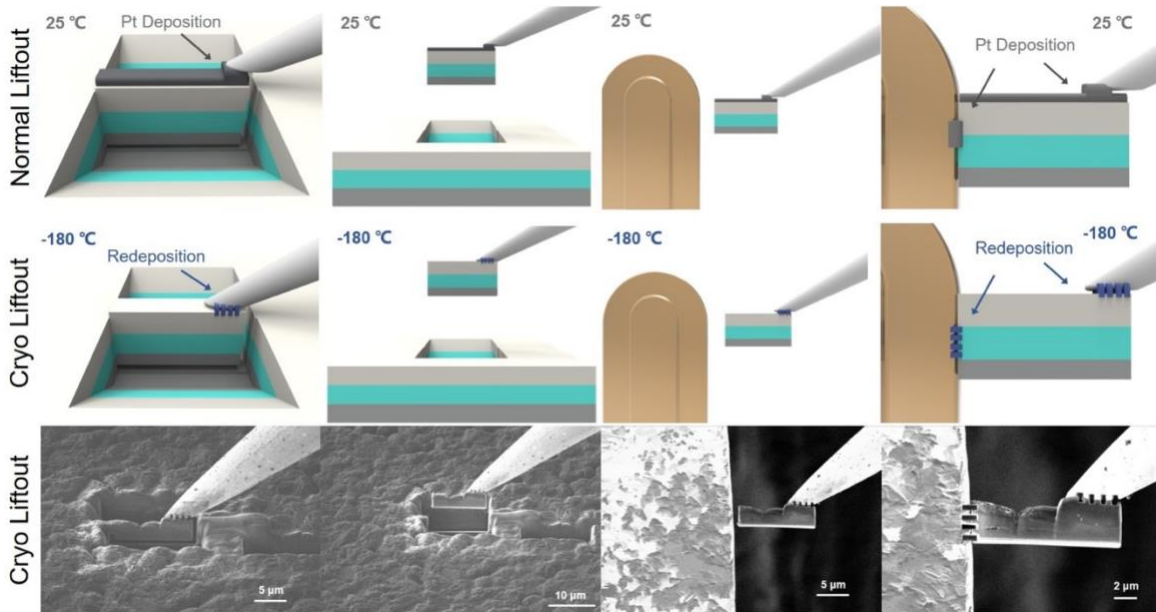
Figure 4.2 Redeposition mounting methodology. At -180 ℃, several rectangular milling patterns are drawn at the junction of tungsten probe and lamella top surface. A 10-pA ion beam current is then used to mill through the patterned region, where the redeposition materials will redeposit at the surrounding region and connect lamella with the tungsten probe for liftout at cryogenic temperature.

As shown in Figure 4.1C, the Li/LiPON interphase lamella was extracted from a sample that consists of 1.5-μm lithium metal deposited on a LiPON thin film and thinned to less than 120 nm for TEM observation. The TEM sample was transferred into the TEM column with minimum air exposure using a glovebox. The sample protection methods for each transfer process are listed in Table 2.1. Prior to the observation of Li/LiPON interphase, we first examined the beam stability of LiPON in cryo-EM since FIB-prepared LiPON has shown electron beam susceptibility at room temperature.[105] Figure 4.3 demonstrates that continuous high-resolution imaging in cryo-STEM did not cause obvious damage or morphology change of LiPON, showing the capability of cryo-FIB and cryo-EM to preserve the structure of otherwise beam intolerant solids.[57] Besides the beam stability, the amorphous phase of LiPON at cryogenic temperature was confirmed by cryo-XRD,

as shown in Figure 4.4, to exclude the effect of potentially phase change of LiPON during the

following cryo-(S)TEM observations.

Table 4.1 Electrical and ionic conductivities of different SEI components

	Electronic Conductivity (S/cm) at 298K	Ionic Conductivity (S/cm) at 298K
Li_2O[113]	10^{-14}	10^{-12}
Li_3N[114]	10^{-12}	10^{-4}
Li_3PO_4[37,115]	10^{-9}	10^{-8}
LiF[116,117]	$<10^{-12}$	$<10^{-8}$
LiCl[118,119]	10^{-6}	$<10^{-7}$
Li_2S[120,121]	10^{-9}	10^{-8}
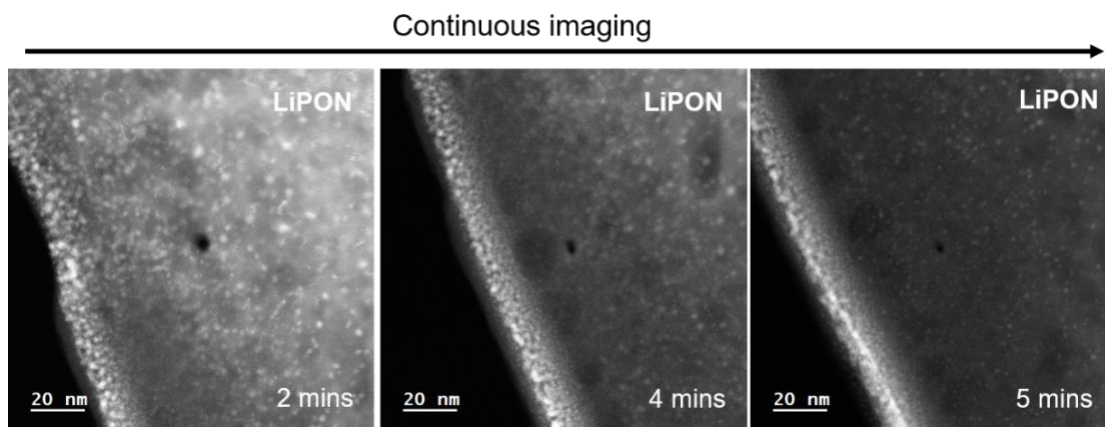
Figure 4.3 Beam stability demonstration of LiPON under high-magnification cryo-STEM
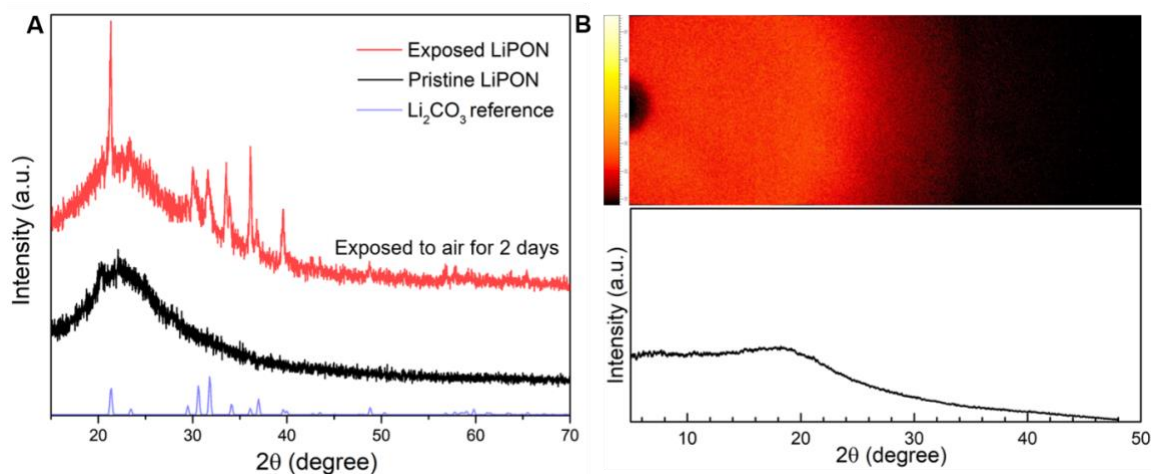
Figure 4.4 Room-temperature and cryo-temperature XRD of LiPON. (A) The XRD pattern of pristine LiPON (black) and LiPON exposed in air for 2 days (red). The peaks on the exposed LiPON can be indexed to the peaks from Li_2CO_3 as shown at the bottom. (B) The cryo-XRD pattern of pristine LiPON showing the amorphous phase of LiPON at 100 K.

4.3.2 Concentration gradient across the Li/LiPON interface

Figure 4.1D shows the cryo-STEM dark field (DF) image of the Li/LiPON interface where the Li metal and LiPON regions are approximately distinguished by the contrast difference. Regions were further identified by energy dispersive x-ray spectroscopy (EDS) mapping results of the elemental distribution of P (Figure 4.1E) and N (Figure 4.1F). Interestingly, P and N content were both observed in the Li metal region. To quantify the chemical evolution across the interface, an EDS line-scan was carried out at the region indicated by the black dashed line in Figure 4.1D, where the concentration evolution of P and N were captured and plotted in Figure 4.1G. From the
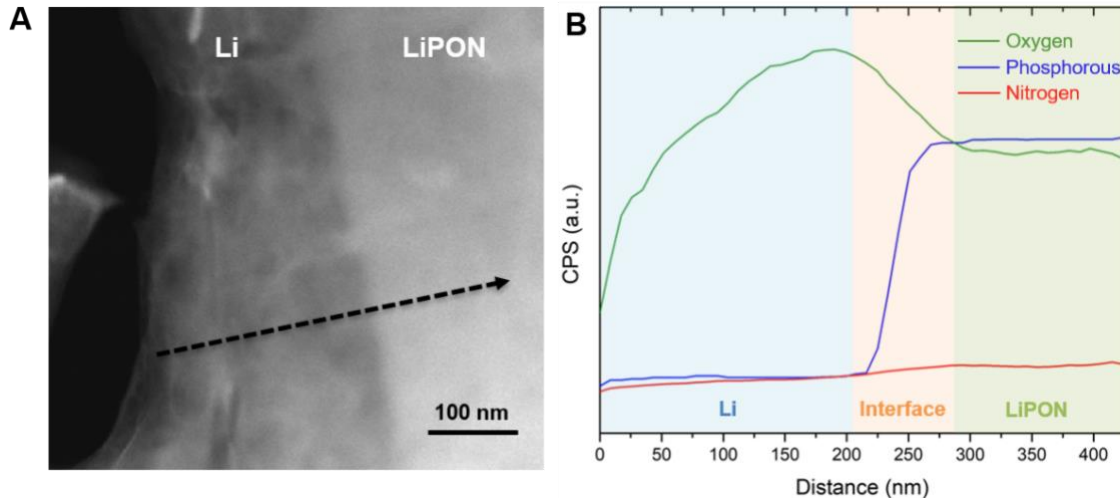
Figure 4.5 EDS linescan at the interphase. (A) Cryo STEM DF image of Li/LiPON interphase. (B) EDS linescan CPS of O, P and N signals with respect to distance along the black dashed arrow in (A). The Li metal region, interphase region and LiPON region are indicated by the blue, orange and green background, respectively.

Li metal to the LiPON, both concentrations of P and N had a clear increase and reached their maximum in the bulk LiPON region, where elemental P and N were uniformly distributed in the bulk of LiPON. Interestingly, the presence of P and N was not directly correlated to the contrast difference associated with the Li/LiPON interface. Instead, the concentration changes began from Li metal region, with a gradient of P and N increasing across the interphase. Furthermore, N signal was detected from a much deeper region into the Li metal side than P signal, indicating a further

diffusion of N species into the Li metal region compared with P. Based on the concentration gradient in Figure 4.5, the width of Li/LiPON interphase region was about 76 nm.

4.3.3 High resolution observation of a nanostructured interphase

To probe the structural evolution associated with the observed concentration gradient, cryo-high-resolution TEM (HRTEM) was performed at the Li/LiPON interface (Figure 4.6A). The inset fast Fourier transform (FFT) pattern in Figure 4.6A first illustrates the coexistence of Li metal, Li_2O, Li_3N and Li_3PO_4 species distributed in the probing area by matching the lattice spacings of corresponding species with the pattern, hereby identifying this interface as a complex, nanostructured interphase. The compositional evolution from the Li metal region to LiPON region was then investigated stepwise, with FFTs taken from region 1 to region 4 as highlighted by the orange squares in Figure 4.6A, corresponding to Figure 4.6B, D, F & H respectively. In the region near the Li of the Li/LiPON interphase (Region 1), the presence of Li metal and Li_2O were identified based on the FFT spots of (110) plane of Li metal and (111) plane of Li_2O shown in Figure 4.6B. Region 1 represents the beginning of the interphase, with a mixing of Li metal and Li_2O, due to the extreme susceptibility of Li metal to oxygen to form Li_2O. Moving further inside to Region 2, the FFT (Figure 4.6D) identified the appearance of Li_2O, Li_3N and small amount of Li metal, according to the lattice spacings. The (001) FFT spot of Li_3N demonstrated an earlier appearance of N at the interphase, which was likely related to the diffusion of N species within Li metal. Approaching closer to LiPON region (Region 3), no Li metal was observed and Li_2O, Li_3N and Li_3PO_4 species were identified by FFT shown in Figure 4.6F. All of the species present at Region 3 are considered decomposition products of the LiPON, in part predicted by DFT

thermodynamic calculation.[25] Figure 4.6H demonstrates the amorphous structure of LiPON in the bulk region (Region 4).

As for the nanostructures, Figure 4.6C was acquired from Region 1 in Figure 4.6A, where the nanostructures of Li metal and Li_2O were found to be surrounded by amorphous region. The size of these nano crystals was about 3-5 nm. Figure 4.6E, G & I display the nanostructures at the Region 2-4 in Figure 4.6A, respectively. Notably, all the nano crystals were found to be embedded in an amorphous matrix, with a mosaic-like SEI distribution. However, a layered distribution of decomposition products was also indicated as discussed previously from Region 1 to Region 4, which will be further discussed in the following sections. All the nanostructures at the interphase being embedded in an amorphous matrix maintained the fully dense nature of Li/LiPON interphase even after decomposition. From the cryo-TEM and STEM EDS analyses, thus, we observe that (1) the width of Li/LiPON interphase was about 76 nm, (2) the interphase exhibits concentration gradients of P and N, and (3) the interphase consisted of the decomposition products as predicted in the form of nanostructures embedded in a dense amorphous matrix. The presence of Li_3N at the Li/LiPON interphase is analogous to successful liquid-electrolyte SEIs which have enabled stabilized Li metal.[25,122,123] To obtain the statistics of the interphase distribution, the thicknesses of different layers ($Li+Li_2O$, $Li+Li_2O+Li_3N$ and $Li_2O+Li_3N+Li_3PO_4$ layers) within the interphase was extracted from ten different regions, where the depth of each layer was recorded and plotted in Figure 4.6J. The averaged thicknesses of each layer are summarized in Figure 4.6K, where the thickness of $Li+Li_2O$, $Li+Li_2O+Li_3N$ and $Li_2O+ Li_3N+ Li_3PO_4$ layers are 21.1 nm, 11.6 nm and 43.7 nm in average, constituting a interphase with an average thickness of 76.4 nm, consistent with the observations from EDS line-scans.
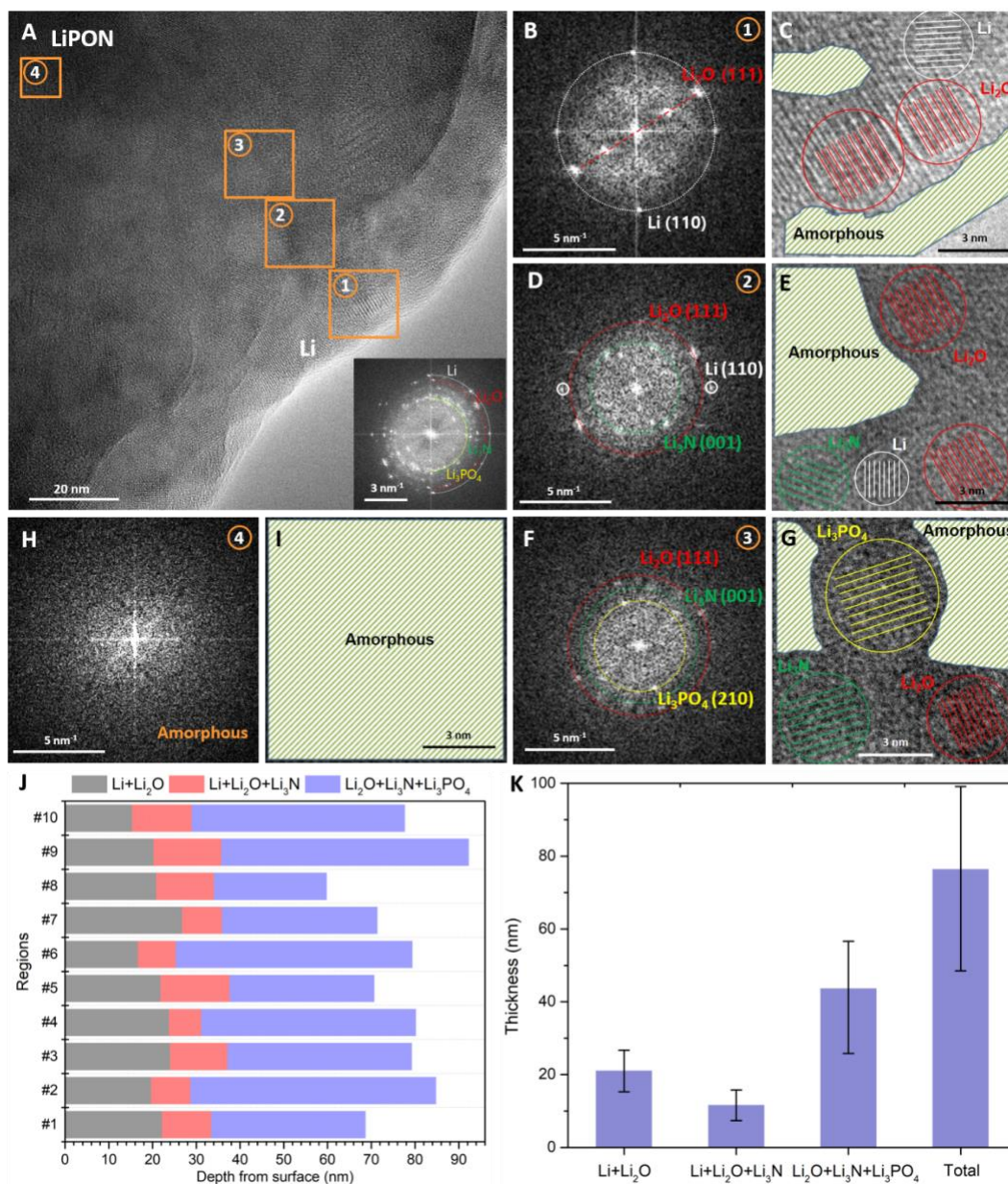
Figure 4.6 Nanostructures of Li/LiPON interphase and statistics of cryo-TEM results. (A) HRTEM image of the interphase where four regions (region 1-4) are highlighted by orange squares to indicate different stages of the multilayered structure across the interphase. Inset image is the FFT result of the whole area in (A). (B, D, F & H) FFT patterns corresponding to region 1-4. (C, E, G & I) Nanostructure schematic corresponding to region 1-4. (J) Depth distribution of different layers within the interphase extracted from 10 different regions. (K) The thicknesses of different layers averaged from the results in (J).

53

4.3.4 Cryo-STEM-EELS uncovers local chemical environment

Cryo-STEM-EELS was conducted to obtain further insight of the chemical evolution across the Li/LiPON interphase. Figure 4.7A shows the cryo-STEM DF image of the sample where five spots highlighted within the green arrow were sampled to extract the EELS spectra of Li K-edge, P L-edge and O K-edge along the interphase shown in Figure 4.7B. EELS spectra were acquired every 12 nm with the lowest point located at the LiPON region. As comparison, EELS spectra for corresponding edges of Li_2O, Li_3PO_4, Li_3P and LiPON species were simulated by FEFF9 and shown in Figure 4.7C. The amorphous LiPON structure (shown in Figure 4.8) was generated by *ab initio* molecular dynamics (AIMD) following the protocol outlined by Lacivita *et al.*[52]

The experimentally measured EELS spectra for Li K-edge, P L-edge and O K-edge at LiPON region (black spectra in Figure 4.7B) agreed well with the simulated EELS spectra for corresponding edges of LiPON in Figure 4.7C. The consistency further corroborates the structural model used to generate LiPON EELS, which has been unclear until recently.[37,52,55] The two main peaks as labeled as peak I and peak II in the Li K-edge spectra in Figure 4.7B have brought intriguing insights. According to the simulation, peak I (located at around 59.5 eV) corresponded to the main peak in Li K-edge spectra of LiPON while peak II (located at around 63 eV) corresponded to the main peak of Li_2O (Figure 4.7C). As moving from the interphase towards LiPON region, the intensities ratio of peak I to peak II increased in the experimental spectra. This implied that both Li_2O and LiPON contributed to the experimental Li K-edge spectra (Figure 4.7B),
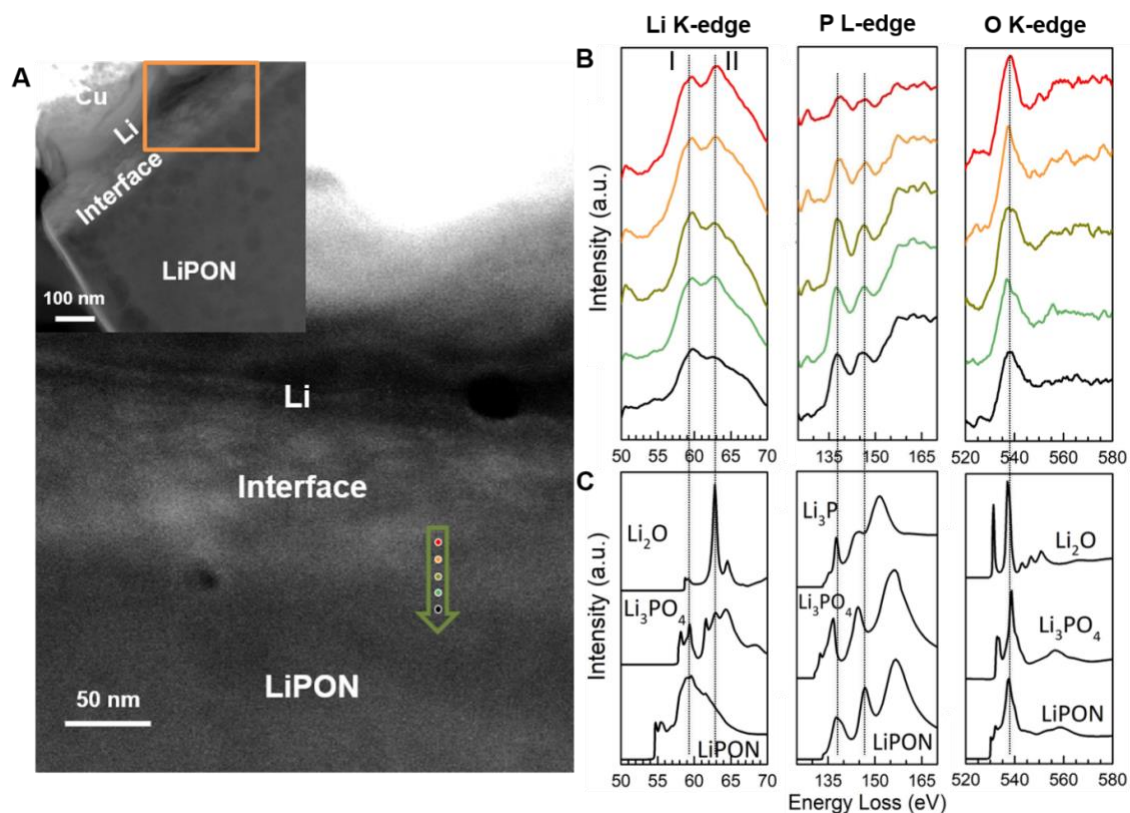
Figure 4.7 Cryo-STEM-EELS analysis of Li/LiPON interphase. (A) Cryo-STEM DF image of Li/LiPON interphase, where five spots highlighted in the green arrow are sampled to extract EELS spectra of Li K-edge, P L-edge and O K-edge shown in (B). The spacing between each sampling point is 12 nm. Inset is a low-magnification STEM DF image of the sample, where the orange rectangle indicates the sampling area shown in the main image. (C) Li K-edge, P L-edge and O K-edge EELS spectra of Li_2O, Li_3P, Li_3PO_4 and LiPON simulated by FEFF9.
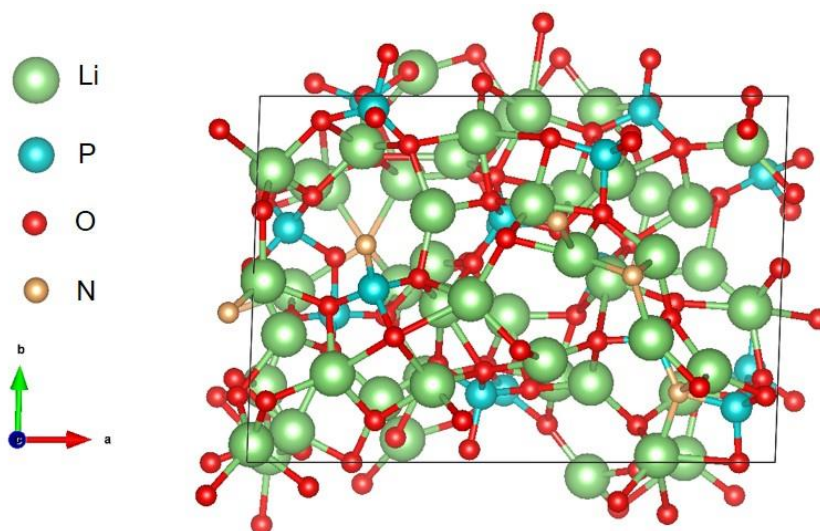
Figure 4.8 Amorphous LiPON structure generated by AIMD. This structure contains 46 Li atoms, 16 P atoms, 55 O atoms and 5 N atoms, with a stoichiometry of $Li_{2.88}PO_{3.44}N_{0.31}$.

and that the contribution from Li_2O was decreasing as approaching closer to LiPON region. This observation agreed with the cryo-TEM results, where the interphase was identified as nanocrystals distributed within an amorphous matrix that is likely to consist of structural units of LiPON. In terms of P L-edge spectra in Figure 4.7B, the two peaks located around 138 eV and 141 eV originated from the P-O polyhedral structure, which were consistent with peak features in the simulated P L-edge from Li_3PO_4 and LiPON in Figure 4.7C, as both have P-O/N polyhedra as the primary structural units. No obvious changes of the edge features were observed except the peak intensities for the P L-edge from interphase to LiPON, indicating the presence of P-O polyhedra at the interphase, emphasizing its structural stability. Similarly for the O K-edge, the experimental spectra did not exhibit notable changes in the edge features through the interphase, indicating the persistence of the local structure in the form of P-O polyhedra. Thus, cryo-STEM-EELS confirmed that the decomposition products were embedded in the amorphous matrix, which was likely to be a mixing of P-O tetrahedrons.

4.3.5 Chemical evolution confirmed by XPS depth profiling

Cryo-EM analysis revealed the structure and chemistry of the nanoscale Li/LiPON interphase, though locally. To complement the observation from cryo-EM in a larger scale across the interphase and confirm the structural distribution within the SEI structure, X-ray photoelectron spectroscopy (XPS) depth profiling was conducted on Li/LiPON thin films samples with 100-nm-thick Li metal evaporated on the top of the LiPON. Since the etching rate was non-quantitative, the etching depth was linearly converted from the etching time and thus shown with an arbitrary unit. Figure 4.9 illustrates the chemical evolution of O 1s, N 1s, P 2p and Li 1s regions of the Li/LiPON sample with etching through the interphase layer. For comparison, reference XPS

spectra of a LiPON thin film sample was shown in Figure 4.10. Before etching started, only O 1s

and Li 1s signal were obtained, which can be attributed to the surface Li_2CO_3 and interphase Li_2O

species. At an etching depth of 54, signal from N 1s appeared. As the N 1s peak became stronger,

the spectra could be assigned to Li_3N, appearing at a binding energy of 394.4 eV. Note that no P

2p signal was detected at this stage. However, when the etching depth reached 138, the presence

of P 2p peak located at 132.8 eV implied the existence of P-containing species, which was mainly

attributed to phosphate groups at the interphase. The composition content changes of O 1s, N 1s

and P 2p were plotted in Figure 4.11, showing that after the C signal was mostly eliminated at the

etching depth of 54, the content of Li and O almost remained the same along the interphase. The

concentration gradient of N and P species were also present where N 1s signal appeared first during

etching and P 2p signal started to emerge after. The unique sequential distribution of O-, N- and

P- containing species identified by XPS depth profiling provided another evidence of the

multilayered structure of such interphase, where mosaic structures were present in each layer,

according to the cryo-EM findings.
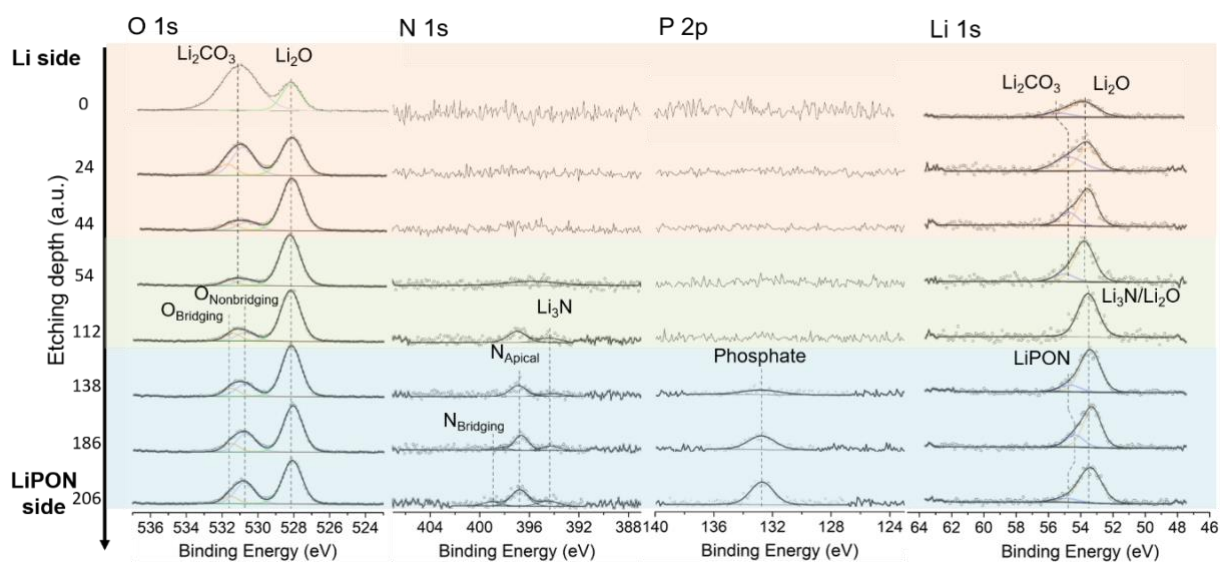
Figure 4.9 XPS analysis. Chemical evolution of O 1s, N 1s, P 2p and Li 1s along Li/LiPON interphase by XPS depth profiling.
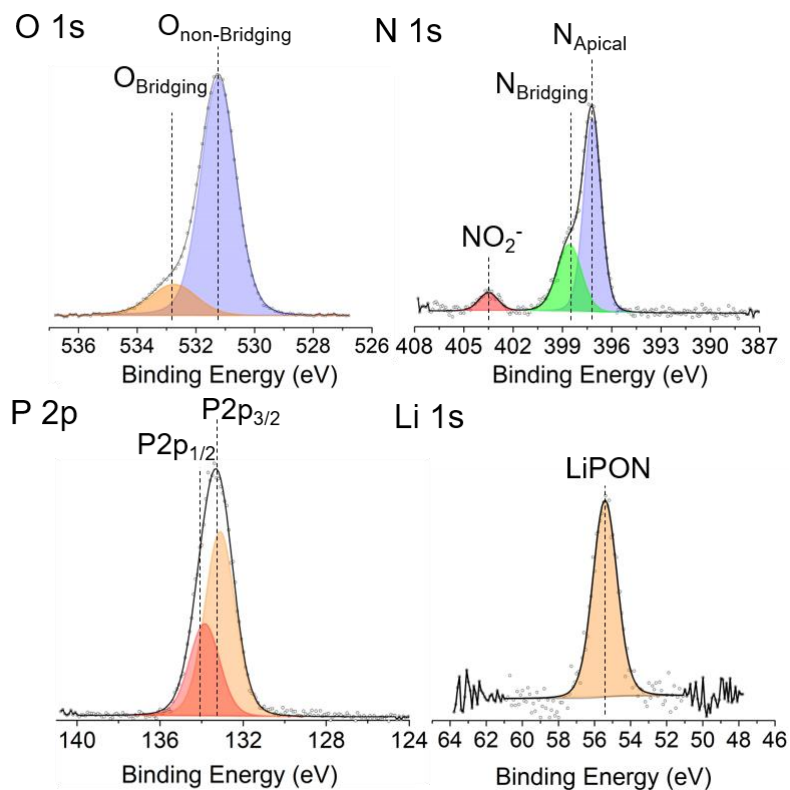
Figure 4.10 Reference XPS spectra of LiPON for O 1s, N 1s, P 2p and Li 1s regions.
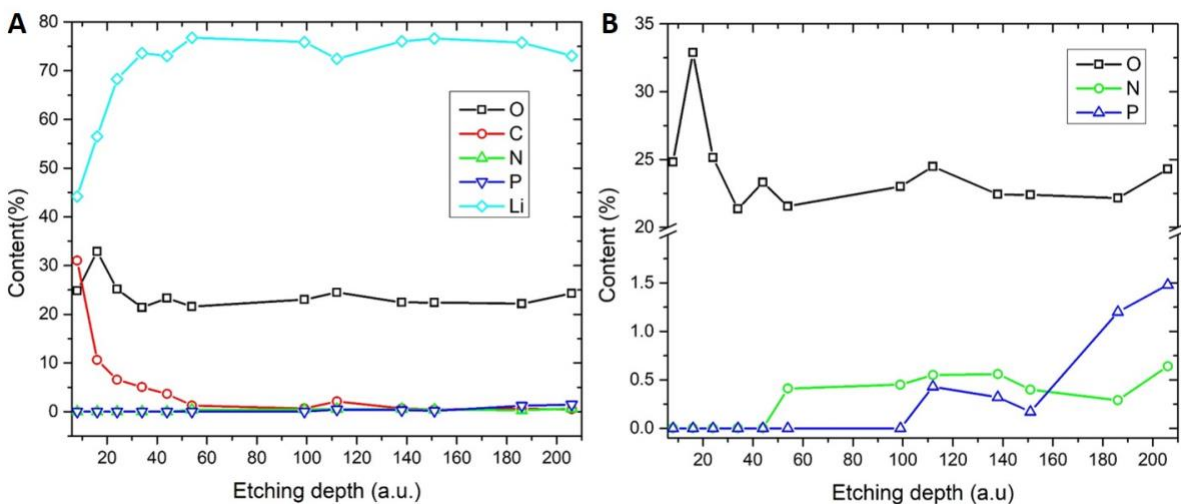
Figure 4.11 Chemical evolution of O 1s, N 1s, P 2p and Li 1s along Li/LiPON interphase by XPS depth profiling. (A) Composition content evolution of O, C, N, P and Li elements through the interphase. (B) zoomed-in content evolution plot of O, N and P elements from (A), where gradients of N and P are observed and N signal appears first at the interphase.

4.4 Discussion

4.4.1 On the formation of a stable interphase

Through cryo-EM, spatially resolved characterization of a solid-solid interphase on the order of 100 nm was achieved, highlighting the importance of precise control of temperature and environment when observing buried interfaces. The formation of such a fine interphase requires consideration of potential mechanistic pathways for decomposition, but also stabilization. A primary consideration, recent literature has described RF-sputtered LiPON as a dense, stable glass. Sputtered glassy films are desirable for their uniformity, but also their high density, potentially exhibiting characteristics of a glass annealed on extremely long time-scales. So-called ultrastable glasses exhibit high kinetic stability and are speculated to be one source of the remarkably small interphase.[124]

Despite the potential for kinetic stability, the high reduction potential of Li metal will drive decomposition of a pristine SSE interface, predicted by DFT. By alternating the composition and chemical potential of Li, one can compute a grand potential space where a convex hull can be constructed. Compounds that sit on the convex hull at a given lithium chemical potential are considered stable against Li metal.[26] These DFT results suggested a decomposition reaction between Li and LiPON will result in the formation of Li_3P, Li_2O and Li_3N as the equilibrium constituents, which has been complemented by *in situ* XPS findings.[25,31] At high potentials alternate phase equilibria are predicted, forming P_3N_5, $Li_4P_2O_7$, and N_2 at the oxidation potential;[25] these results are counterintuitive, provided the cyclability of cells including the Li/LiPON interface, and suggest other considerations are lacking, particularly compositional variability.

Converse to calculated phase equilibria, we observe the Li/LiPON interphase to consist of Li_3PO_4, Li_2O, Li_3N within an amorphous matrix, lacking a clear signature of Li_3P. While

predicted[26] and observed,[30,125] Li_3P is unlikely to be stable at an interphase at equilibrium. The metastability of Li_3P is further corroborated by its absence at the Li-metal/$Li_7P_3S_{11}$ interphase.[126] These observations highlight the potential difference between metastable, transient states, as likely observed via *in situ* XPS, and equilibrium structures achieved by thick layers of Li. These differences may be brought on by the modified activity of reduced volumes of Li metal. Diffusivity of decomposed ions also provides chemical flexibility in stable phase formation, here, driven by the low formation energy of Li_3PO_4 relative to Li_3P (-2.769 eV and -0.698, respectively).[127]

Further deviation from the predicted phase equilibria exist as a function of spatial distribution of the nanocrystals. This is likely enabled by the surprisingly wide distribution of N and P signatures through the interface, suggesting the concurrent dissociation via the reductive potential of Li and elemental diffusion due to the presence of elemental concentration gradients. Under-coordinated apical N (N_a) sites are most susceptible to bond dissociation, exhibiting bond strengths nearly half as low as P-O bonds.[128] Cleavage energy calculations of P-N_a and P-O bonds from isolated phosphate tetrahedra similarly show P-O bonds in isolated PO_4 polyhedra to be approximately three times stronger than P-N, with N bridging (N_b); this is consistent with previous literature showing that P-N_b bond tends to be the first chemical bond to break when LiPON is reduced by Li metal.[129] After the cleavage of P-N_b bond, the remaining undercoordinated PO_3 either give way to further decomposition or contribute to the formation of the amorphous matrix.

The presence of the N and P gradients through the interface (as determined by dark field contrast) indicates that there is significant diffusivity of the decomposed species within the Li metal. To corroborate the potential for diffusion through Li metal, complimentary transition state calculations show a low energy barrier for interstitial diffusion (Figure 4.11A) for both P and N (0.42 eV and 0.5 eV, respectively, as shown in Figure 4.11B), a likely contribution to gradients

observed via EDS. While it is known that nitrogen incorporation into Li_3PO_4 structure enhances the ionic conductivity by two orders of magnitude[37], previous computation efforts using either bulk crystalline LiPON structure [33] or LiPON chains [129] against Li metal, showed that P-N-P bond at the bridging-N site is the most thermodynamically and kinetically unstable in LiPON structures.
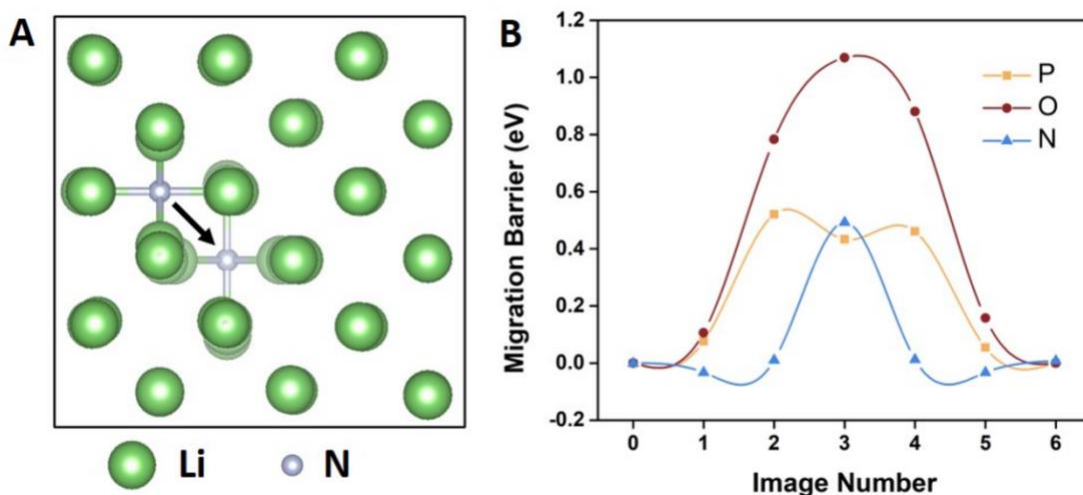
Figure 4.12 Interstitial diffusion. Decomposed LiPON components may (A) diffuse through Li metal via interstitial diffusion. Transition state calculations show (B) diffusion barriers of P, O and N in Li metal to be 0.42 eV, 0.5 eV and 1.08 eV, respectively, indicating the low diffusion barriers of N and P.

It should become apparent that the presence of a complex, stable interphase enabling stability against Li metal in part by the modification of the phase diagram associated with decomposition. At a very early stage, Li metal first reacts with LiPON and diffuses into LiPON region in the form of Li^+ ions. With the proceeding of the interphase equilibration, decomposed structural units or ions will remain mobile within Li metal either diffusing through the bulk of Li metal or crystalizing when a critical concentration is achieved. Diffusion gradients observed result in the gradual shielding of the SSE, ultimately reducing the reductive potential of Li acting on the LiPON. As concentrations of dissociated atoms increase at the interface, further structural reconfiguration may occur, where P combines with surrounding undercoordinated Li, O to form a more stable Li_3PO_4 instead of Li_3P, as the XPS gives primarily the phosphate signal in P 2p region

at the interphase. The interfacial decomposition and reconfiguration result in the formation of an 80-nm-thick interphase with N and P gradients between Li metal and LiPON. *In situ* approaches are required for validating the proposed formation mechanism.

In short, the formation of this stable interphase is likely a unique combination of kinetic stability of the glassy electrolyte and the decomposition of highly diffusive species within Li metal that form a variety of nanocrystals within an amorphous matrix. Evolution of this interphase under electrochemical stimuli will be reported in follow up work.

4.4.2 A distinctive SEI structure found at Li metal/LiPON interphase

Characterization results obtained from cryo-EM methodology have raised some intriguing insights from the Li/LiPON interphase. Concentration gradients of P and N are present across the interphase. The decomposition products, Li_2O, Li_3N, Li_3PO_4 and an amorphous matrix, were clearly identified at the interphase with a length of about 76 nm and a multilayer-mosaic SEI component distribution. Since Li_2O, Li_3N and Li_3PO_4 appear as equilibrium phases at the interface of Li metal, such a thin interphase with ionically conductive but electronically insulating components in a gradient configuration is capable of reducing the effective activity of the Li metal anode, shielding the solid electrolyte from further decomposition, as demonstrated in Figure 4.13. Such an eminent passivating effect cannot be realized when the decomposition products from SSEs are mixed electronic and ionic conductors. For instance, $Li_{10}GeP_2S_{12}$ and $Li_{0.5}La_{0.5}TiO_3$ produce electronically conductive Li-Ge alloy and titanates upon being reduced by Li metal that are not able to alleviate the continuous decomposition.[25] In contrast, a similar passivation layer that consists of LiCl, Li_2S and reduced phosphorous species has been identified between Li metal and Li_6PS_5Cl to account for the good cyclability of Li_6PS_5Cl against Li metal anode.[126] However, given

the physical properties of different SEI components (Table 3.1), Li_3N and Li_3PO_4 are likely to be more suitable for constituting a good SEI than LiCl or Li_2S, due to their higher ionic conductivity and lower electronic conductivity.
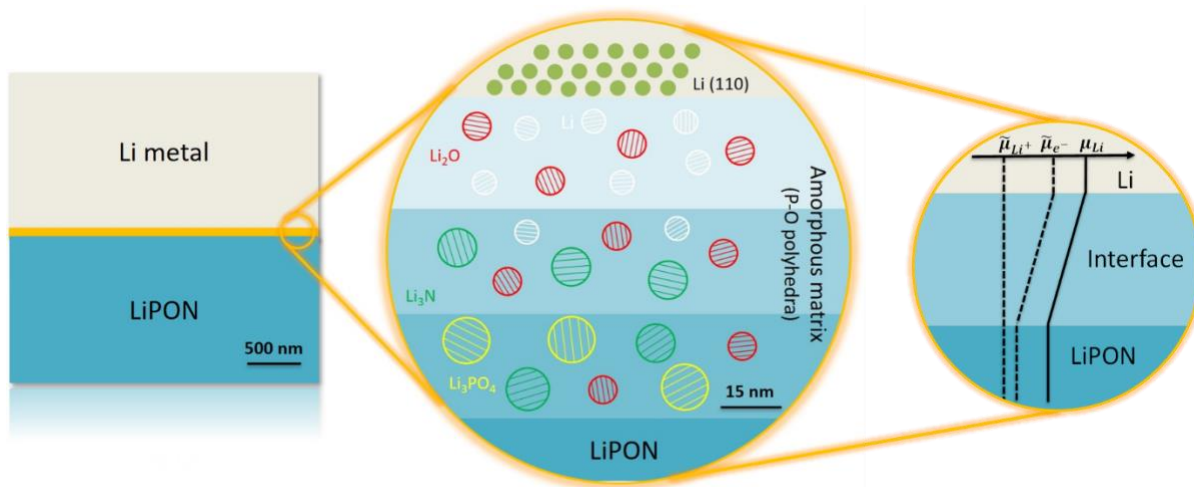
Figure 4.13 Li/LiPON multilayered interphase schematic. $\tilde{\mu}_{Li^+}$, $\tilde{\mu}_{e^-}$ and μ_{Li} are the electrochemical potential of Li ion, the electrochemical potential of electron and the chemical potential of Li, respectively.

From a perspective of successful SEI composition, major components within SEIs formed in liquid electrolytes consist of Li_2O, Li_2CO_3, LiF and other alkyl lithium species that are partially reduced by Li metal during SEI formation. The prevalent belief in the passivating effects of such SEIs has driven numerous research efforts to elucidate the passivation mechanism of these species. Nevertheless, the poorly understood alkyl lithium species within the SEIs makes the exact roles of inorganic species including Li_2O, Li_2CO_3 and LiF unclear. As one of the most popular SEI components that has been extensively studied, LiF, is known for its low electronic conductivity and high thermodynamic stability against Li metal as to explain its passivation effects against Li metal.[25] However, its view as the dominant contribution in Li stabilization has been questioned in a recent work.[69] In the SEI known for its good electrochemical stability, there are only inorganic

species present at Li/LiPON interphase, which could also raise concerns regarding truly validating the roles of LiF on constructing a good SEI when all the alkyl lithium species are absent. As has been proposed previously, Li_3N is one of the most promising candidates as an SEI component, due to its thermodynamic stability against Li metal, high ionic conductivity and extremely low electronic conductivity.[114,122] Consequently, the presence of Li_3N at Li/LiPON interphase accounts for the good cyclability of LiPON against Li metal to some extent. From a perspective of SEI structure, the fact that the decomposition products exist as nanostructures and are embedded in a dense amorphous matrix in a mosaic form brings another important perspective of a good interphase for Li metal, where there are no porosity or grain boundaries present that may become nucleation sites for dendrite growth.

4.5 Conclusion and outlook

In summary, we successfully preserved and characterized the Li/LiPON interphase by developing the cryo-lift-out methodology and combining cryo-FIB and cryo-S/TEM. The observed 76-nm-thick Li/LiPON interphase consisted of SEI components including Li_2O, Li_3N and Li_3PO_4, which remained fully dense after decomposition. We discovered the concentration gradients of N and P species along the interphase, consistent with the structural evolution identified by cryo-HRTEM. A multilayer-mosaic SEI model was proposed based on these observations. We further proposed the reaction mechanism for Li/LiPON interphase, stressing the diffusion of decomposition product species and structural reconfiguration during equilibration. The comparison with SEIs formed in liquid electrolyte raised questions regarding the roles of alkyl lithium species and LiF in stabilizing Li metal. We caution that electrochemical stability of the Li/LiPON interface, while of utmost importance, explains only some of the high voltage cyclability

and LiPON remains one of the few SSEs that can withstand the oxidative potential present in cycling with high voltage cathodes, in stark contrast to liquid electrolyte counterparts and emphasizing the importance of complementary cathode-electrolyte interphase characterization. Nevertheless, the observed structure and proposed mechanistic pathway provide valuable insights for further study on other solid interphases in battery systems by both computational and experimental efforts, raising the importance of kinetics in the modification of phase diagrams, and giving rise to a better understanding of the stability of such interphases. A good interphase needs to fulfill several requirements to obtain exemplary cyclability - formation of a stable passivation layer, uniform coverage, fully dense and thermodynamic stability with Li metal. While an ideal SEI has yet to be demonstrated with liquid electrolytes, LiPON fills these requirements and exemplifies stable Li metal cycling, paving the way towards high-energy long-standing batteries.

Chapter 4, in full, is a reprint of the material, as it appears in: **D. Cheng**, T. A. Wynn, X. Wang, S. Wang, M. Zhang, R. Shimizu, S. Bai, H. Nguyen, C. Fang, M. Kim, W. Li, B. Lu, S. J. Kim and Y. S. Meng, "Unveiling the Stable Nature of the Solid Electrolyte Interphase between Lithium Metal and LiPON via Cryogenic Electron Microscopy", *Joule*, 2020, 4, 11, 2484-2500. The dissertation author was the primary investigator and first author of this paper.

Chapter 5. Unraveling the Stable Cathode Electrolyte Interface in All Solid-State Thin-Film Battery Operating at 5V

Spinel-type $LiNi_{0.5}Mn_{1.5}O_4$ (LNMO) is one of the most promising 5 V-class cathode materials for Li-ion batteries that can achieve high energy density and low production costs. However, in liquid electrolyte cells, the high voltage causes continuous cell degradation through the oxidative decomposition of carbonate-based liquid electrolytes. In contrast, some solid-state electrolytes have a wide electrochemical stability range and can withstand the required oxidative potential. In this work, a thin-film battery consisting of a LNMO cathode with a solid lithium phosphorus oxynitride (LiPON) electrolyte is tested and their interface before and after cycling is characterized. With Li metal as the anode, this system can deliver stable performance for 600 cycles with an average Coulombic efficiency > 99%. Neutron depth profiling indicates a slight overlithiated layer at the interface prior to cycling, a result that is consistent with the excess charge capacity measured during the first cycle. Cryogenic electron microscopy further reveals intimate contact between LNMO and LiPON without noticeable structure and chemical composition evolution after extended cycling, demonstrating the superior stability of LiPON against a high voltage cathode. Consequently, we propose design guidelines for interface engineering that could accelerate the commercialization of a high voltage cell with solid or liquid electrolytes.

5.1 Introduction

Li-ion batteries (LIBs) are dominant battery technologies for portable electronic devices and electrical vehicles due to their high energy density, thermal stability, and long cycle life.[130,131] However, a wider adoption of LIBs requires gravimetric energy densities in excess of 350 Wh kg^{-1} (1 Wh = 3,600 Joules) at the cell level, and up to 500 Wh kg^{-1} for more than 1000 cycles.[17,132] At present, the energy densities of mass-produced LIBs are limited to 200 Wh kg^{-1} - 250 Wh kg^{-1} at

the cell level.[133,134] The cathode is regarded as a critical component in improving the capacity of commercial cells. With a high operating voltage (4.7 V vs. Li^+/Li^0),[135,136] a spinel-type cathode material $LiNi_{0.5}Mn_{1.5}O_4$ (LNMO) could potentially empower industrial producers to achieve these high energy density goals. Recently, the strong desire to eliminate cobalt in cathode materials has sparked a renewed interest in this class of oxides.[137] Various attempts to fabricate LNMO/graphite batteries that exhibit high voltage, relatively high energy density, and fast charging capabilities using organic liquid electrolyte have been carried out worldwide,[138–140] but they all suffered from excessive degradation and limited cycle life, especially when stored or cycled at a highly charged state.[141] The primary reason is that most common liquid electrolytes (e.g., carbonic ester solvent combinations with lithium hexafluorophosphate ($LiPF_6$) solute) are prone to oxidization and subsequent decomposition on the cathode surface as a cell's voltage rises over 4.5 V during charging. This is caused by a lack of an effective passivation layer[141–143], which helps prevent decomposition of the liquid electrolyte, and can cause a cell to continuously degrade.

All-solid-state batteries (ASSBs) may provide a viable pathway to use LNMO and achieve the desired high energy density and cycling stability. ASSBs have received enormous attention over the last few decades as they have good intrinsic safety, high packing density, and a relatively large electrochemical stability window with the potential to enable both high voltage cathodes and metallic lithium anodes.[25,144] A key factor in successful integration of LNMO in ASSBs will be pairing the electrode material with a compatible electrolyte. Solid state electrolytes (SSEs) prevent catalytic dissolution of transition metals from the cathode into the electrolyte, which leads to capacity loss and graphite anode degradation when liquid electrolytes are used.[142,145] Lithium phosphorus oxynitride (LiPON) is one of the most promising candidates for this application as it has a wide electrochemical stability window up to 5.5 V,[55] a modest ionic conductivity ($\approx 10^{-6}$ S

67

cm^{-1}),[55] suitable mechanical properties,[53,146] and has demonstrated cycling stability against LNMO cathodes and lithium metal anodes.[40] The prevailing form of LiPON material as a thin film synthesized by physical vapor deposition provides an ideal platform for investigating interfaces against highly oxidative/reductive electrodes.

LiPON as a solid-state electrolyte has been studied with various types of cathode materials, including $LiCoO_2$ (LCO),[41,45,57] $LiMn_2O_4$,[147] and $LiNi_{0.6}Mn_{0.2}Co_{0.2}O_2$ (NMC622).[148] Nevertheless, the underlying mechanism that provides such exceptional stability remains elusive, largely due to a lack of available characterization tools that can access the buried interfaces and tackle the air-/beam-sensitivity of LiPON.[42] Meanwhile, tremendous research efforts have also been invested in the study of the cathode electrolyte interface (CEI) in liquid electrolyte systems, which may hint at the potential origin of the LNMO/LiPON interface stability. The interfacial phenomena in liquid electrolyte systems have been widely characterized through spectroscopic and microscopic methods. X-ray photoelectron spectroscopy (XPS)[138,141] and attenuated total reflectance Fourier transform infrared spectroscopy (ATR-FTIR)[141] were employed to identify the chemistry of the CEIs. After cycling with a carbonate-based electrolyte, a CEI layer forms on the LNMO surface which includes decomposition products of $LiPF_6$ solute and the organic solvents LiF, Li_2CO_3, $Li_xPO_yF_z$ and polymerized ethylene carbonate (PEC). Continuous electrolyte decomposition occurrs due to the non-uniformity of the CEIs and an insufficient passivation effect. Cryogenic electron microscopy (cryo-EM) has shown that an uneven CEI layer can form after 50 cycles within a conventional carbonate electrolyte. Improved cycling and a uniform CEI was observed by the same technique but for a sulfone-based electrolyte.[87] Another factor to be considered is the addition of binders and conductive agents in composite cathodes for liquid electrolyte systems. These additives result in parasitic reactions with an electrolyte and can make deconvolution of

interfacial reactions between active materials and electrolytes challenging. As such, an ideal interface between LNMO and LiPON must limit electrolyte decomposition, result in conformal CEI formation, minimize cathode structural change, and be free of conductive agents.

An all-solid-state thin film format was employed in this study to examine the origin of the stable interface between LNMO and LiPON. The samples consisted of dense electrode layers without binder, conductive carbon, or coating materials. NDP was utilized to delineate the lithium concentration profile across the LNMO/LiPON interface. Results from this measurement were coupled with first-principles computation and cryogenic electron microscopy (cryo-EM) to investigate interfacial chemistries and textures. Based on these findings, crucial characteristics of the solid electrolyte that impact the interfacial stability are discussed and a proposal is made of key factors that facilitate the design of stable, high voltage cells by rational interface engineering.

5.2 Experimental Methods

5.2.1 Thin film sample preparation

LNMO thin-films were deposited on platinum-coated alumina substrate (Valley Design) by pulsed laser deposition (PLD) system (Excel Instruments PLD STD-12 chamber and 248 nm KrF Lambda Physik-Pro 210 excimer laser) with a laser energy fluence of ≈ 2.0 J cm^{-2} and 24000 pulses at a frequency of 10 Hz. The substrate temperature was heated to 600 °C, and partial pressure of O_2 was controlled at 200 mTorr (1 mTorr = 133.322 Pa, SI unit) during the deposition. The LNMO target used for PLD was prepared using LNMO powder (NEI corporation, USA). 12 g of LNMO powder and 0.47 g of LiOH (Sigma-Aldrich) were used to achieve a 30% Li excess LNMO target. The materials were ball milled and pelletized onto a 28.6 mm dye press at a pressure of 10 Mg for 10 min. Following this step, the pellet was sintered at 900 °C for 2 h with a heating

ramp rate of 3 °C min^{-1}. The resulting target surface was polished by sandpaper (Grit 320 and 600, Aluminum oxide, Norton abrasives) before every deposition. LiPON thin films were deposited by radio-frequency (RF) sputtering. A Li$_3$PO$_4$ target that was ≈ 50 mm in diameter (Plasmaterials, Inc.) was used as a sputtering target. The sputtering power was set at 50 kg·m^2·s^{-3} (W). Nitrogen gas (Matheson, ultra-high purity grade) and the partial pressure at 15 mTorr for deposition. LNMO was deposited to a thickness of ≈ 650 nm and an active area of 4.9 mm^2, corresponding to an active material loading of 0.03 mAh cm^{-2} for the full cell fabrication. LiPON was then sputtered on LNMO to a thickness of 1 μm. A Li metal anode and Cu current collector were then deposited on to the LiPON by thermal evaporation (LC Technology Solutions Inc.) under a base pressure below 3×10^{-11} mTorr. The average deposition rate of Cu and Li were controlled at 0.1 nm s^{-1} and 0.15 nm s^{-1}, respectively. Deposition was monitored by a quartz crystal microbalance. The thickness of Li metal anode was 570 nm and corresponds to a 203% excess capacity compared to that of the cathode. The thickness of the LNMO and LiPON were controlled at 2.6 μm and 2.2 μm thick, respectively, for the NDP measured samples.

5.2.2 Grazing incidence angle X-ray diffraction (GIXRD)

XRD pattern of the fabricated thin film was taken by Rigaku Smartlab X-ray diffractometer with Cu Kα source (λ = 1.5406 Å; 1 Å = 0.1 nm, SI Units) with a working voltage and current of 40 kV and 44 mA, respectively, and a scan step size of 0.04°. The scan speed was 0.12° min^{-1}, and the scan range was from 15° to 80°.

5.2.3 Liquid cell fabrication

The LNMO thin films were also tested with liquid electrolyte in a coin cell. An LNMO thin film deposited on a Pt-coated alumina substrate (1 cm^2 surface area, cathode) was coupled with ≈ 100 μL of 1M LiPF$_6$ in EC:EMC (3:7 wt%) electrolyte and a Li metal chip as an anode. The coin cell consisted of a CR2032 type casing and one piece of a Celard 2325 separator. The cell was cycled between 3.5 V and 4.85 V with a 10 μA constant current.

5.2.4 Electrochemical measurement

Two LNMO/LiPON/Li full cells were cycled with a Biologic SP-200 potentiostat. For the first cell, the voltage range of the cycling was set at 3.5 V - 5.1 V and the applied current was 150 nA and 3.0 μA. This is equivalent to a ≈ C/10 and ≈ 5C charging rate, respectively. The cell was cycled at C/10 during the first 2 cycles and the last 3 cycles (1st, 2nd, and 533rd to 535th cycle) and cycled at 5C for the remaining cycles. The electrochemical cycling data of this cell has already been published in our past study[42] and its characterization by (S)TEM were conducted, shown in this paper. The other full cell was cycled for 600 cycles in the same voltage range with the current at 100 nA for 1st, 2nd, and 600th cycles and 1.7 μA for the remaining cycles, which are almost equivalent to ≈ C/7 and ≈ 4C charging rate, respectively. The second cell was fabricated for the purpose of confirming reproducibility of the cell performance, demonstrated in this paper. The areal capacity of the cells was calculated based on the assumption that only part of LNMO above Pt current collector (≈ 3 mm in diameter) was involved in the electrochemical reaction.

5.2.5 Neutron depth profiling and fitting

Neutron depth profiling (NDP) data was collected at the National Institute of Standards and Technology (NIST) Center for Neutron Research (NCNR) at the end position of the cold Neutron Guide 5. The ^{6}Li atoms in the sample were of interest for these experiments and measured through detection of the ^{3}H$^+$ (triton) charged particle products from the n,^{6}Li reaction:

$$^6Li + n_{cold} \rightarrow {}^4He^{2+}(\alpha, 2055.55\ keV) + {}^3H^+({}^3H, 2727.92\ keV) \qquad (3.1)$$
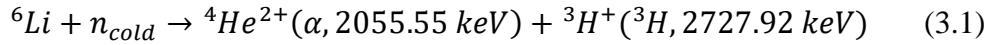
Following reaction ^{4}He^{2+} and ^{3}H$^+$ particles are promptly produced and immediately begin to lose energy due their interactions with the nuclear and electronic properties of the sample material. However, the ^{4}He particles were blocked from the detector in this experiment by the polyimide cover that was added to the surface of the sample to protect the battery material from the ambient atmosphere. Only the ^{3}H$^+$ particles were analyzed for all the samples measured.

The sample was mounted behind a 0.5 mm thick Teflon sheet with a ≈ 3.0 mm circular aperture. This aperture was fixed to an Al support frame and placed facing the primary transmission-type silicon surface barrier detector (Ametek) inside the NDP chamber. The energy spectra of the detected particles were collected and transmitted to a Lynx^{TM} Digital Signal Analyzer (Canberra) with a setting of 4092 channels. Data were acquired for ≈ 5 h per sample. Each sample area was irradiated at a neutron fluence rate of ≈ 1.2×10^9 neutrons cm^{-1} sec^{-1}. A high-vacuum chamber was used for the measurements of the sample, background profiles (Teflon, Si wafer), and a ^{10}B concentration reference material (in house). Li atom concentrations were calculated using the natural abundance of ^{6}Li for sample and ^{10}B as a reference. Li concentration was calculated by equation (3.2):

$$D_{Li} = \frac{D_{10B} \times \sigma_{10B}[barns]}{n_{6Li} \times C_{10B}[counts\ sec^{-1}] \times \sigma_{6Li}[barns]} \times C_{6Li}[counts\ sec^{-1}] \qquad (3.2)$$

D_i is the areal concentration of ^{10}B, ^6Li, or Li (i) in i atoms cm^{-2}, σ_i is the thermal neutron cross-section for the isotope i (1 barn = $1\mathrm{x}10^{-28}$ m^2), n_{6Li} is the natural abundance of ^6Li, and C_i is the normalized particle counts detected in the measurement. The calculated data was binned according to energy resolution of the NIST NDP system ($\approx$ 22 keV for a ^3H at 2727 keV). More details of the data processing can be found in the SI. The uncertainties of both LNMO/LiPON and LNMO are <6% and reported to 1 sigma, which are estimated from the propagation of the experimental counting statistics from the sample, reference, and background materials.

5.2.6 First-principles calculations

LNMO at various charged/discharged states were studied by density functional theory (DFT) with the Vienna Ab initio Simulation Package (VASP). Periodic plane-wave DFT+U static calculations were performed for the LNMO bulk structure. Supercell models, $Li_8Ni_4Mn_{24}O_{32}$, were used as $Li_xNi_{0.5}Mn_{1.5}O_4$ at x = 1. To simulate Li removal from x = 1 to 0 a corresponding number of Li atoms were removed at each state. Li atoms were inserted into tetrahedral sites between octahedral sites containing Ni or Mn atoms to simulate the overlithiation of the cathode material. A 3×3×3 k-point mesh and an energy cutoff of 520 eV were employed at the calculation. U_{eff} values were chosen as 5.96 eV and 4.5 eV for the +U augmented treatment of Mn and Ni 3d orbitals, respectively. The initial MAGMOM parameters were set as follows: Li*(0), Ni*(-2), Mn*(+4), O*(0). Partial density of states (PDOS) at pristine state (x =1) and Overlithiated state (x = 2) were extracted from DOSCAR and analyzed by wxDragon software. PDOS plots were smoothed by a 10-point adjacent average function.

5.2.7 Cryogenic focused ion beam/scanning electron microscopy (cryo-FIB/SEM)

A FEI Scios DualBeam FIB/SEM with a cooling stage was used to prepare the TEM samples of pristine LNMO/LiPON and cycled LNMO/LiPON/Li samples. The operating voltage of the electron beam was 5 kV and emission current of the beam was 50 pA. These setting were used to mitigate potential beam damage on Li and LiPON. A Ga ion beam source was used to mill and thin the sample with an operating ion beam voltage of 30 kV. Emission currents of the ion beam were selected depending on purposes: 10 pA for ion beam imaging, 0.1 nA for cross-section surface cleaning and lamella thinning, and 3 nA for pattern milling. The sample stage temperature was maintained at -185 °C during pattern milling, cross-section cleaning, and lamella thinning processes to preserve the Li metal and LiPON components. A cryo-liftout methodology was applied for the TEM sample lift-out process where sample materials were redeposited between the lamella and the probe for connection. Detailed procedures with illustration were described in our past study.[42]

5.2.8 Cryogenic transmission electron microscopy (cryo-TEM)

The prepared lamellas were transferred from the FIB chamber though an air-free quick loader and stored in an Ar-filled glovebox. Cryo-HRTEM images were collected on a JEOL JEM-2100F TEM at 200 kV with a Gatan Oneview camera. Cryo-STEM/ EELS results were collected on a JEOL JEM-ARM300CF TEM at 300 kV. A TEM cryo-holder (Gatan 626 cryo-transfer holder) was used to load the samples where TEM grids were immersed in liquid nitrogen and then mounted onto the holder via a cryo-transfer workstation.[42] Uncertainty of the energy loss in EELS spectra are 1 eV, which is attributed to the energy resolution of the detector.

5.3 Results and Discussions

5.3.1 Electrochemical behavior of LNMO/LiPON/Li full cell over long-term cycling

The presence of a stable interface was first demonstrated by a thin film battery consisting of a high-voltage spinel LNMO cathode, a LiPON solid electrolyte, and a lithium metal anode. The detailed architecture of the cell is shown in Figure 5.1, where the deposited LNMO thin film displays a well crystallized structure with (111)-plane-orientated texture in Figure 5.2A. This is in good agreement with the films produced by Xia et al.[149,150] Figure 5.3 illustrates the cycling performance of the full cell. As shown in Figure 5.3A, the 1st cycle charge profile displays an excess capacity compared with the subsequent cycles, while the voltage profiles at the 2nd cycle and 600th cycle resemble each other, implying an irreversible reaction during the 1st cycle and a superior cyclability afterwards. The cycling stability is further demonstrated by a Coulombic efficiency of $\approx$ 99.6% for 600 cycles in Figure 5.3B. Compared with the LNMO cathode performance in liquid electrolyte such as Figure 5.2B, two characteristic features are observed in the thin film battery with the LiPON solid electrolyte: *i*) an excess capacity during the first charge and *ii*) cycling stability observed for the course of 600 cycles. Note: 1 mAh is equal to 3.6 C (SI units).
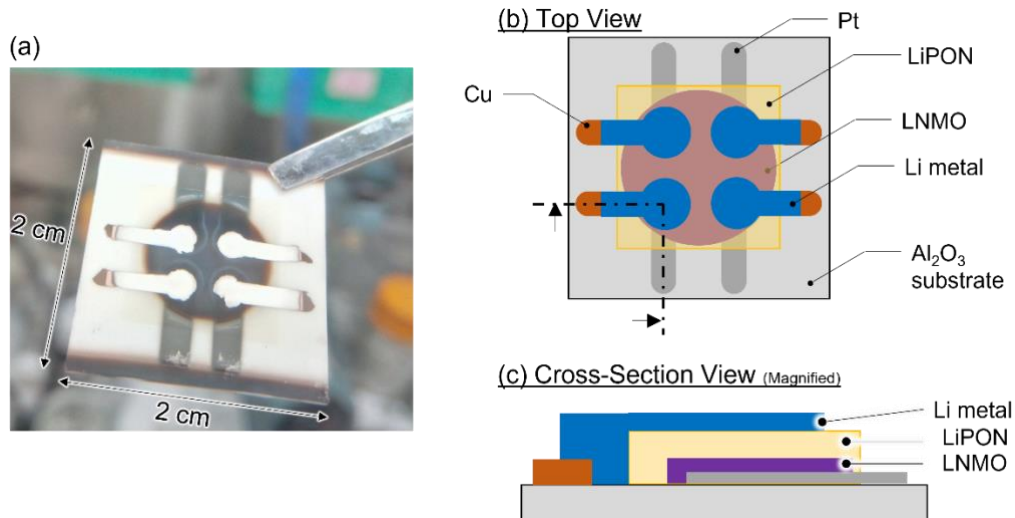
Figure 5.1 LNMO/LiPON/Li full cell configuration. (A) Photo image of LNMO/LiPON/Li thin film full cell and (B, C) schematic of the cell configuration
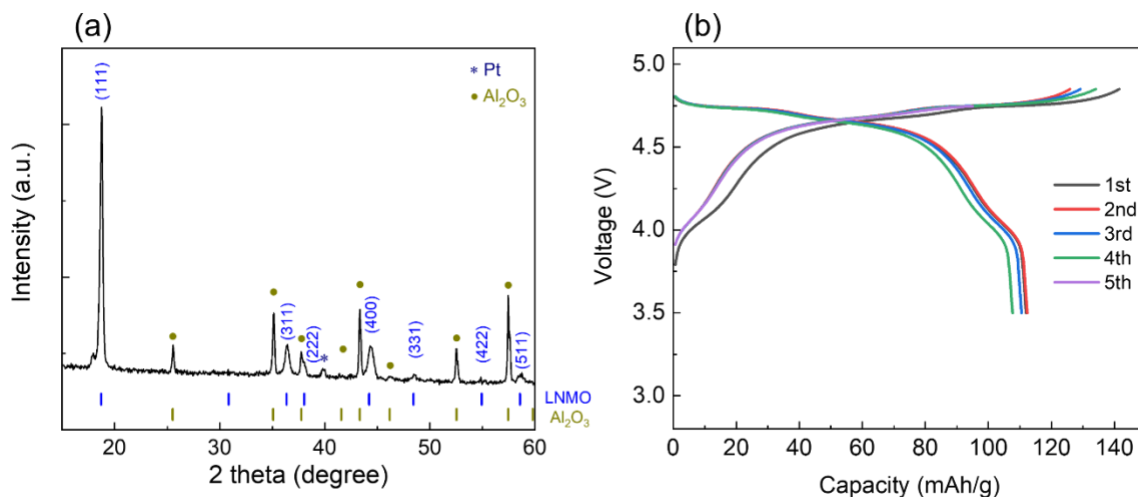
Figure 5.2 Properties of bare LNMO thin film. (A) XRD pattern of LNMO deposited on Pt-coated alumina substrate. (B) Voltage profiles of LNMO/Li half-cell with carbonate-based electrolyte. Uncertainty of the capacity is about 25%, which comes from the estimation of LNMO active mass.
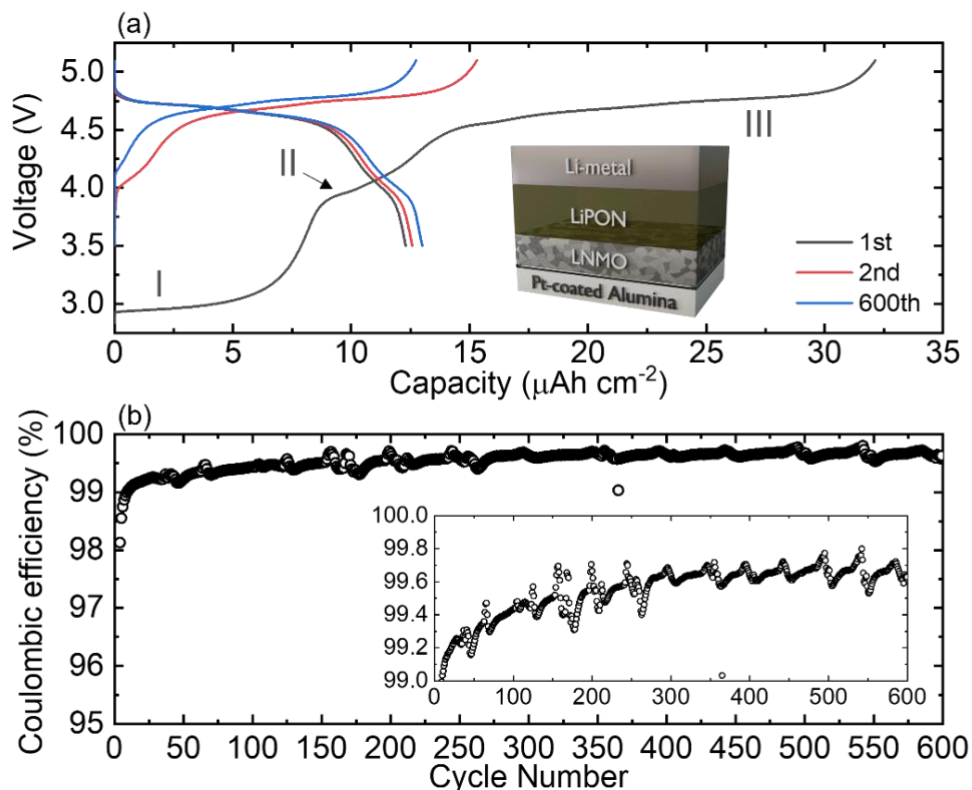
Figure 5.3 Electrochemical performance of LNMO/LiPON/Li full cell. (A) Voltage profiles of LNMO/LiPON/Li thin film full cell at 3.5 V - 5.1 V at the 1st, 2nd, and 600th cycle. (B) Coulombic efficiency of the cycled cell, which was charged/discharged at a about C/7 for the 1st and 2nd cycles, and 4C for the rest of cycles. The C rate was set back to C/7 at the 600th cycle. Uncertainty of the areal capacity in the voltage profile is ~3%, attributed to the estimation of the cell active area. Periodic fluctuation of the Coulombic efficiency comes from temperature change in a day during the measurement.

The voltage profiles indicate that the dominant redox reactions in the LNMO cathode are 4.7 V vs. Li^+/Li^0 (shown as plateau region III in Figure 5.3A) and correspond to the Ni^{2+}/Ni^{3+} and Ni^{3+}/Ni^{4+} redox couples during the initial charging process.[151,152] A small amount of Mn^{3+}/Mn^{4+} redox couple occurring near 4 V (plateau region II in Figure 5.3A) contributes to the nominal capacity when part of the Mn species in a pristine LNMO thin film has an oxidation state lower than 4+. The LNMO thin film is likely overlithiated chemically during the full cell fabrication, which leads to a lower Mn oxidation state in the surface region of LNMO. This is apparent in regions I and II (Figure 5.3A), where an excess of charge capacity during the first cycle is caused

by a plateau at 2.9 V and 4 V. Note that the pristine LNMO thin film cycled in liquid electrolyte does not exhibit an overlithiated feature as indicated by Figure 5.2B and previous studies.[150,153] The overlithiation of LNMO is proposed to be caused by LiPON deposition and chemical reactions between LNMO and LiPON during or after the deposition.

5.3.2 Li concentration gradient across LNMO/LiPON interface

Neutron depth profiling (NDP), is a robust method by which select light elements (e.g., Li) can be quantified.[154] Unlike XPS depth profiling technique, NDP is a nondestructive approach,[155,156] which enables the quantification of the average Li concentration through the sample along the thickness direction. There have been numerous studies over the last several years, where NDP has been applied to the study of Li-ion battery materials.[154,157–159] In this study, NDP was utilized to examine the Li concentration profile of a pristine LNMO/LiPON sample to investigate the possibility of LNMO overlithiation.

Figure 5.4A is a schematic of NDP measurement setup, where samples are mounted in a vacuum chamber and cold neutrons are directed at a sample. Along the pathway, neutron may react with ^{6}Li and generates charged particles, ^{4}He^{2+} (alpha) and ^{3}H$^+$ (triton), with characteristic kinetic energies. Note that alpha particles are filtered out by the thin polyamide film cover and only the triton particles are detected. The energy loss of the charged particles as they pass through the material is due to the stopping power of the material. Li concentration as function of depth is obtained by plotting the detected number of triton particles as a function of final kinetic energy. During this experiment, a LNMO/LiPON thin film sample was measured by NDP, with a LNMO thin film measured as a reference for the interface sample. Figure 5.4B exhibits triton-based Li areal concentration depth profiles from the LNMO/LiPON sample (black), LNMO sample (red),

and their subtraction (blue) in Li atoms cm^{-2}. The subtracted profile represents variations in Li across the bulk and interface regions of sample after the LiPON layer is added to the LNMO.

To estimate the contributions from the bulk LiPON and interface regions, the subtracted curve (blue dots in Figure 5.4B & C) is fitted with a Weibull function as shown by eq. (3.1) in the energy range between 2551 keV and 2358 keV, where bulk LiPON is dominant in the LNMO/LiPON sample.

$$y = a_0 \left(\frac{a_3-1}{a_3}\right)^{\frac{1-a_3}{a_3}} \left(\frac{x-a_1}{a_2} + \left(\frac{a_3-1}{a_3}\right)^{\frac{1}{a_3}}\right)^{a_3-1} \exp\left[-\left(\frac{x-a_1}{a_2} + \left(\frac{a_3-1}{a_3}\right)^{\frac{1}{a_3}}\right)^{a_3} + \frac{a_3-1}{a_3}\right] \quad (3.3)$$

Here, a_0, a_1, a_2, and a_3 are amplitude, center, width (> 0), and shape (>1.01). The fitting results are summarized in Table 4.1. The quality of the fitting is estimated from the R^2 value and is calculated to be 0.9993. The Weibull curve with using the parameters below is extrapolated down to 2140 keV (Figure 5.4C (magenta)).

Table 5.1 Fitting results of subtracted NDP profile by Weibull function

Parameters	Fit results	Errors
a_0	5.08103×10^{16}	$\pm 3.75795 \times 10^{14}$
a_1	2412.46	± 0.72979
a_2	279.079	± 73.2746
a_3	7.79389	± 1.96886
R^2	0.9993	–

The fit model is then extrapolated to the lower energy region to estimate the Li concentration contributed from pure LiPON (magenta curve in Figure 5.4C). Lastly, the subtraction of the extrapolated model (magenta curve in Figure 5.4C) from the calculated curve (blue curve in Figure 5.4C) is plotted as a green line in Figure 5.4C, which represents the interfacial

effect from the LNMO/LiPON sample. As shown in the inset of Figure 5.4C, a noticeable difference in Li concentration between the subtracted (blue) and the extrapolated curve (magenta) can be observed. The positive difference (green) suggests a slight increase of Li concentration at the interface between LNMO and LiPON. Such Li concentration increase (atoms cm^{-3}) in LNMO is further estimated by integrating areal Li concentration in atoms cm^{-2} from the energy range between 2358 keV to 2200 keV, which falls into LNMO region. The integration gives a Li concentration increase of $\approx 4.00 \times 10^{20}$ atoms cm^{-3} at the LiPON/LNMO interface, which is ca. 3% of the concentration compared with the designed stoichiometry of LiNi$_{0.5}$Mn$_{1.5}$O$_4$ cathode. It is worth noting that there is a difference on the amount of overlithiation between NDP and electrochemical testing. This comes from the different quantities that are measured in each characterization – NDP detects all the Li in the film while electrochemical testing solely measures the activated Li ions. It should be emphasized that NDP measures Li concentration across open aperture area centered on the film and demonstrates a 3% Li increase relative to all the cathode materials in the thin film sample. In contrast, the difference between 1st and 2nd charge capacity measured by electrochemical testing only represents how much activated Li in the first cycle is reversible. Considering a higher discharge voltage cutoff (3.5 V) than the open circuit voltage of pristine Li$_{1.0}$NMO (≈ 2.8 V) is used, the difference is attributed to the sum of overlithiated Li and irreversible capacity during cycling. Furthermore, electrochemical testing does not necessarily activate all the materials inside the sample, suggesting the observed capacity would not always match actual Li amount in cathode.[160] One possible source of this increase is overlithiation of the LNMO surface. Different lithiation states of LNMO were therefore investigated with first-principles calculations to further understand the impact of overlithiation on LNMO material. The L$_x$NMO modeling structure was altered from $x = 0$ to $x = 2$ to represent the delithiated state and

overlithiated state of LNMO, respectively. (Figure 5.4D. Figure 5.4E displays the average magnetizations of Mn and Ni species calculated at each lithiation state; this can be used as an indicator of the oxidation state(s) of transition metals.[161,162] The magnetization number of Ni decreases from 1.7 μ_B to 0.5 μ_B (1 μ_B = 9.274×10^{-24} J T^{-1}, SI units) during the delithiation (charging) process (x = 1 to 0). This indicates that the Ni redox changes from Ni^{2+} to Ni^{4+} for the charging process.[161,162] The magnetization number of Ni does not vary due to overlithiation (x = 1 to 2). In contrast, Mn magnetization changes from 3.2 μ_B to 3.7 μ_B when the structure is overlithiated, suggesting a Mn reduction as more Li is inserted into LNMO.
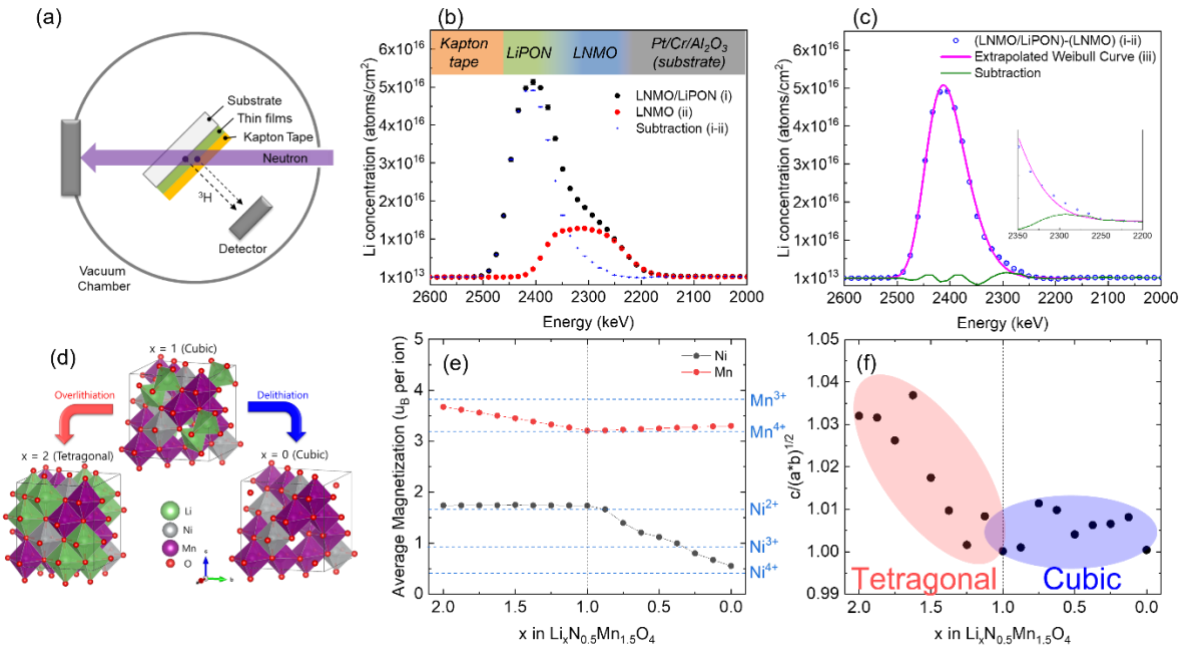
Figure 5.4 Li concentration across LNMO/LiPON interface. (A) Schematic image of neutron depth profiling (NDP) setup. (B) Li concentration profile (atoms/cm^2) of LNMO/LiPON (black), bare LNMO (red), and subtraction of bare LNMO from LNMO/LiPON as a function of detected triton energy. (C) Li concentration profile of subtraction of bare LNMO from LNMO/LiPON (blue, same data in (B)), Li concentration of bare LiPON simulated with Weibull function (magenta), and subtraction of simulated curve from (LNMO/LiPON)-(LNMO) curve (green). (D) Structures of Li$_x$Ni$_{0.5}$Mn$_{1.5}$O$_4$, which are used for DFT calculation, at x = 1 (pristine), x = 0 (delithiated), and x = 2 (overlithiated). (E) Averaged magnetization of Ni (black) and Mn (red) at each lithiated state of LNMO. (F) Relative c length of the supercell at each lithiation state from x = 0 to x = 2 in LxNMO.

Along with the change in magnetization numbers, the relative lattice parameter evolution of the supercell at each lithiation state is plotted in Figure 5.4F. When x in the L_xNMO structure exceeds 1, the lattice parameter in c direction becomes relatively longer than the a and b directions. This leads to a distortion of the lattice in the c direction and, consequently, a phase transformation to a tetragonal phase. Such Jahn-Teller (J-T) distortion is attributed to the presence of Mn^{3+}. The Mn cation is normally located at octahedral site bonded with O anions. This causes the classical ligand field splitting (crystal field splitting) and, as a result, d-electron states can be split into triplet (t_{2g}) and doublet (e_g) states, which stabilizes the Mn-O bonding configuration. In the case of Mn^{3+}, three of the four 3d electrons are in d_{xy}, d_{yz} and d_{zx} orbitals of the t_{2g} state and leaves one d_{z2} electron in e_g state (high spin state). The Mn-O octahedral structure becomes elongated in the c direction to minimize Coulombic repulsion between the electrons in Mn d_{z2} orbital and the electrons in O 2p orbital as the d_{z2} electron orbitals are parallel to the c direction of the octahedron. Therefore, the presence of J-T distortion when $x > 1$ implies the reduction of Mn from 4+ to 3+. This matches with the average magnetization results in Figure 5.4E.

5.3.3 Mn oxidation state evolution at LNMO/LiPON interface

Scanning transmission electron microscopy/electron energy loss spectroscopy (STEM/EELS) were then conducted to experimentally verify the oxidation state of Mn across the LNMO/LiPON interface. Cryogenic protection was applied on the TEM specimens during STEM measurements, given the beam sensitivity of LiPON as reported in the past study.[42] Figure 5.5A displays the cryo-STEM high-angle annular dark field (HAADF) image of the pristine LNMO/LiPON interface, where LNMO and LiPON regions can be identified based on differences in contrast. The highlighted spots represent the region where EELS spectra were extracted. Mn L-

edge spectra are plotted in Figure 5.5B. The low signal intensity detected in the Mn L-edge spectrum at spot 0 indicates the absence of Mn in this region and that the major component is LiPON. The characteristic peaks of Mn L-edge appear in the spectrum from spot 1 to spot 5, suggesting the range of the LNMO/LiPON interface region. The L_3 and L_2 peaks of Mn L-edge correspond to electron transition from $2p_{3/2}$ and from $2p_{1/2}$ to unoccupied d orbitals, respectively.[163] The oxidation states of the transition metal species can be identified by analyzing the intensity ratio between L_3 and L_2 peaks and comparing it to the values collected on standard Mn compounds in which the oxidation states of Mn are known. A step function is commonly used to fit these spectra (Figure 5.6) so that the intensity ratio of L_3 peak to L_2 peak can be calculated and plotted,[163] as shown in Figure 5.5C. In Figure 5.5C, Mn at spot 1 shows a L_3/L_2 intensity ratio $\approx$ 2.9, while the ratio decreases to $\approx$ 2.4 for the Mn from spot 2 to spot 5. According to Wang et al., L_3/L_2 intensity ratio of 3.85, 2.6, and 2.0 corresponds to Mn^{2+}, Mn^{3+}, and Mn^{4+} oxidation states,[163] respectively. Therefore, the oxidation state of Mn at the starting of the LNMO/LiPON interface is likely to be between Mn^{3+} and Mn^{2+}. This Mn oxidation state at the interface was more reduced than the one found within the LNMO bulk, which is comparable with a bare LNMO thin-film sample (Figure 5.7). The computational results reveal that Mn oxidation state is reduced from 4+ to 3+ when LNMO is overlithiated and form L_xNMO ($x > 1$), as shown in Figure 5.4D. The combination of Mn L-edge intensity ratios, computational results and electrochemistry indicate that Mn at LNMO/LiPON interface (spot 1) shows an oxidation state of 3+, which is likely attributed to the overlithiation of LNMO, while bulk LNMO shown at spot 2 to spot 5 has mixed states of Mn^{3+} and Mn^{4+}. Another possible cause of Mn reduction is the bombardment of LiPON during sputtering. Song et al. has shown that oxygen vacancy can trigger Mn^{3+} generation from Mn^{4+} for charge compensation, and cathodes with more oxygen vacancy can deliver a longer

plateau at 4.0 V in the voltage profile.[151] The Mn^{3+} ions should be oxidized to Mn^{4+} during the charge in the 1st cycle and remain above 3+ after the discharge to 3.5 V as the electrochemical lithiation voltage corresponding to $Mn^{4+} \rightarrow Mn^{3+}$ is at 2.8 V.[151,163]
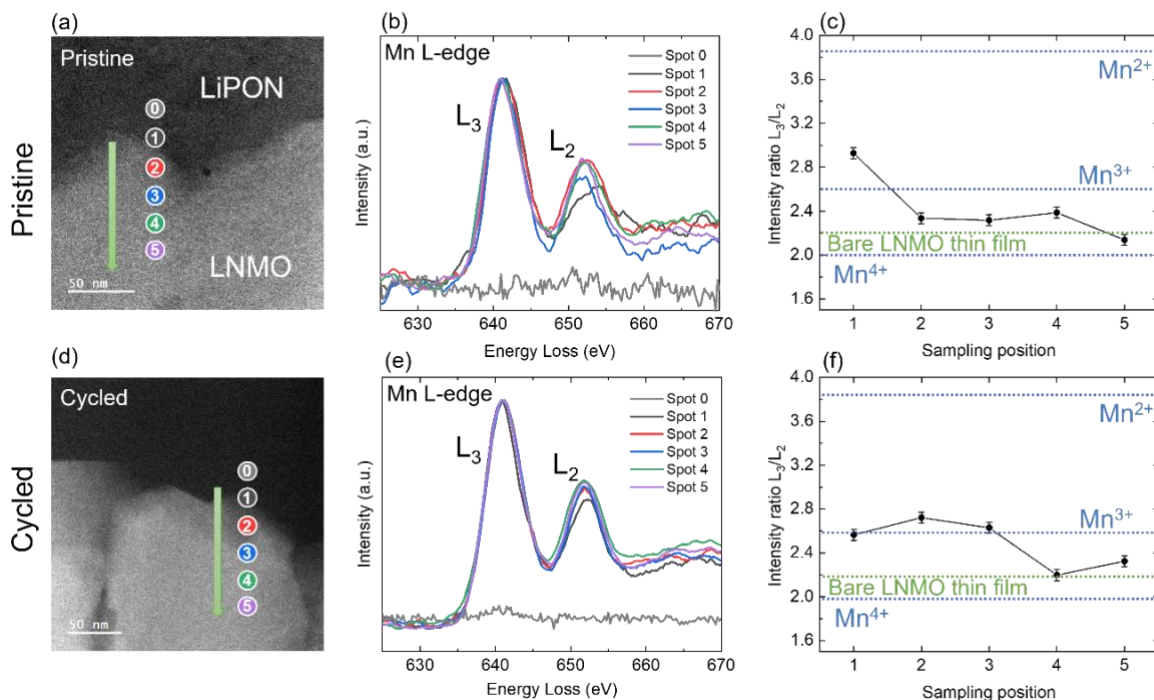
Figure 5.5 Mn oxidation state changes across the pristine and cycled interface. (A-C) Analysis of pristine LNMO/LiPON interface and (D-F) cycled LNMO/LiPON interface. Cryo-STEM image (A) at pristine interface and (D) at cycled interface. (B) Mn L-edge EELS spectra at each point of pristine interface and (E) cycled interface. Intensity ratio of Mn L3 peak to L2 peak with error bars (C) for pristine interface and (F) cycled interface. Details of intensity integration method are illustrated in Figure 4.6.

Figure 5.5D-F shows the Mn oxidation states at LNMO/LiPON interface after 500 cycles. As can be seen in Figure 5.5E, the absence of Mn signal at spot 0 in the STEM image (Figure 5.5D) demonstrates there is no Mn migration from LNMO to LiPON region, in stark contrast to the Mn dissolution phenomena in liquid electrolyte system. Compared to the pristine interface (Figure 5.5C), the cycled interface has much decreased L_3/L_2 intensity ratio at spot 1 in Figure 5.5F, indicating a less reduced Mn environment. During the charging process in the 1st cycle, excess lithium atoms that caused overlithiation of the LNMO are extracted, a process manifests as a

plateau at 2.9 V in the electrochemical measurement. Reduced Mn (Mn^{3+}) due to overlithiation and LiPON deposition is also oxidized in the 1st charge, rationalizing the measured increased Mn oxidation state in subsequent cycles.
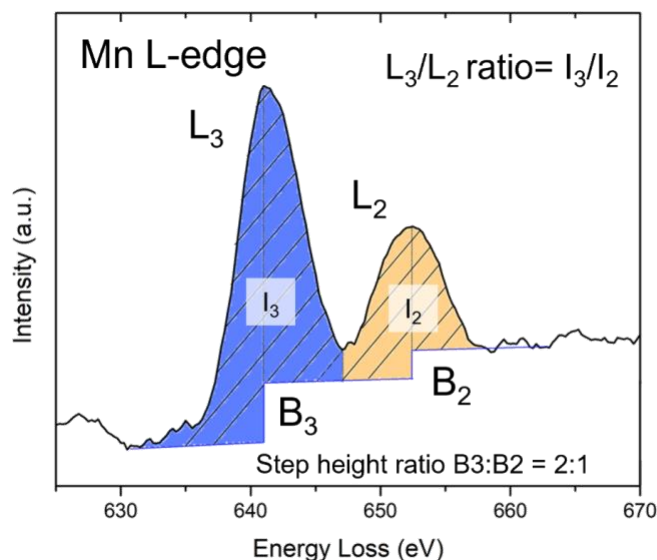
Figure 5.6 EELS spectrum analysis. L3 to L2 ratio calculated by an areal integration and a 2-step background function.
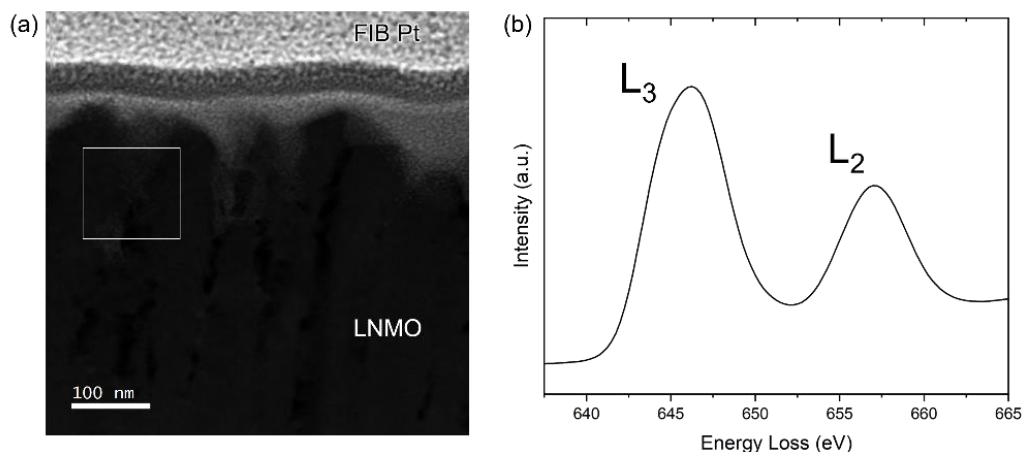
Figure 5.7 STEM/EELS analysis of bare LNMO. (A) STEM image of bare LNMO surface. (B) Mn L-edge EELS spectra at surface region of bare LNMO.

5.3.4 Nanostructure and morphology at LNMO/LiPON interface

The nanostructure and morphology of the layers were additionally characterized to elucidate the interfacial stability and to compliment the above discussed chemical analyses. Cryo-

TEM images at the LNMO/LiPON interface before and after cycling were obtained and summarized in Figure 5.8. Figure 5.8A shows the high-resolution TEM (HRTEM) image of pristine LNMO/LiPON interface. No voids or cracks are formed when LiPON is deposited on LNMO. Detailed nanostructure was also inspected and shown in Figure 5.8B & C. Lattice fringes observed in these images match well with (111) lattice plane of LNMO[164,165] and indicates that LNMO maintains its crystal structure after the full cell preparation. Note that LNMO structure should be slightly distorted due to the lithiation and Mn reduction as aforementioned, while the lattice spacing change due to distortion is significantly small and was not detectable with HRTEM. A cycled LNMO/LiPON interface is shown in Figure 5.8D. It displays surprisingly intimate contact between the LNMO and LiPON layers and an absence of voids or cracks, even after 500 cycles. Figure 5.8E & F demonstrate that the crystal structure of LNMO is maintained in both the bulk and interface regions. Although the cell was cycled at a rate of 5 C, which can be considered as fast cycling and results in the cell having 40% of its original capacity, the LNMO/LiPON interface remains intact and shows no signs of structural change or defect formation. In Figure 5.8G-K, a clear difference between crystalline region and amorphous region is highlighted by the yellow curve along the cycled LNMO/LiPON interface. Very little CEI is observed in this region. These observations provide good evidence for the long-term structural stability of the LNMO/LiPON interface.

An interesting phenomenon was observed in the LiPON after 500 cycles. Cryo-HRTEM imaging of the LiPON in a pristine LNMO/LiPON sample (Figure 5.9A) indicates nanocrystal formation in areas highlighted by the yellow dot lines. These nanocrystalline species are identified as Li_3PO_4 and Li_2PO_2N through the features in Fast Fourier transform (FFT) patterns shown in Figure 5.9B & C. These are likely to be decomposition products of LiPON based on past

computational results.[26] Such partial decomposition occurs only at a small portion of the interface. Similar phenomenon is observed at the cycled LNMO/LiPON interface (Figure 5.10 with lattice patterns displayed in A and FFT analysis displayed in C-E). The presence of LiPON partial decomposition in both pristine and cycled LNMO/LiPON interfaces implies that such decomposition is driven chemically instead of electrochemically. This is discussed further in the following section.
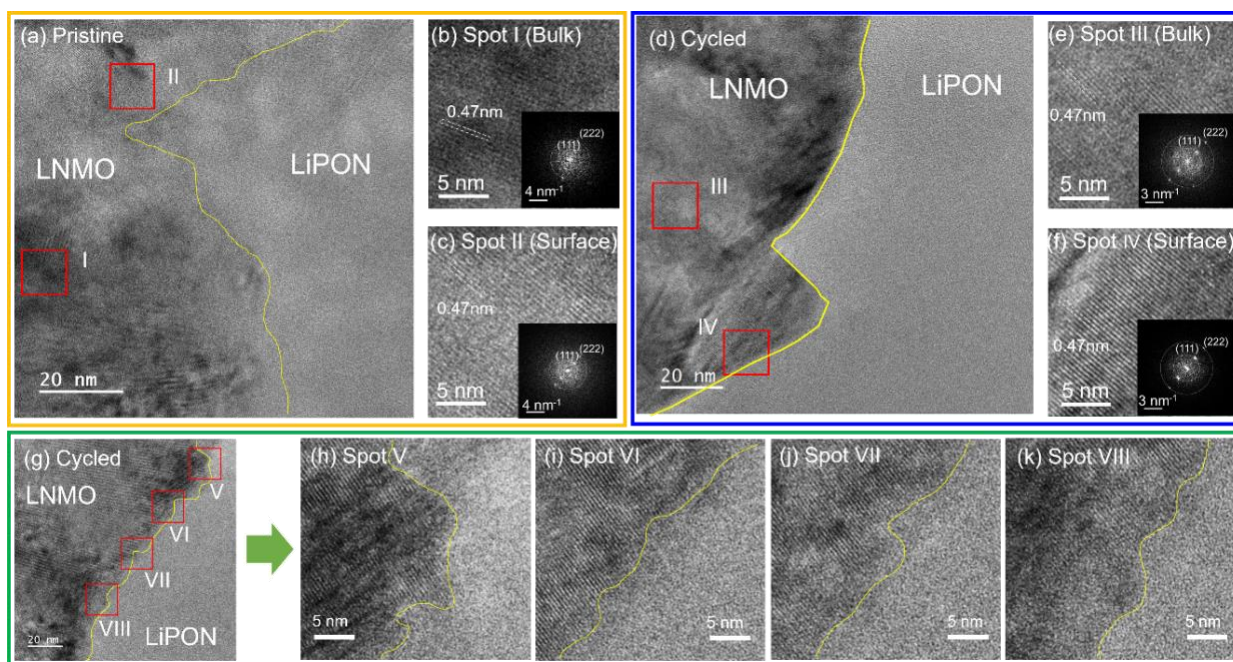
Figure 5.8 Interfacial nanostructure and morphology at the LNMO/LiPON interface. (A) Cryo-TEM image of pristine LNMO/LiPON interface and (B) zoomed LNMO images of bulk (inset; FFT image) and (C) surface (inset; FFT image). (D) Cryo-TEM image of cycled LNMO/LiPON interface and (E) zoomed LNMO images of bulk (inset; FFT image) and (F) surface (inset; FFT image). (G) Another cryo-TEM image of cycled LNMO/LiPON interface and (H-K) zoomed interface images at different spots.
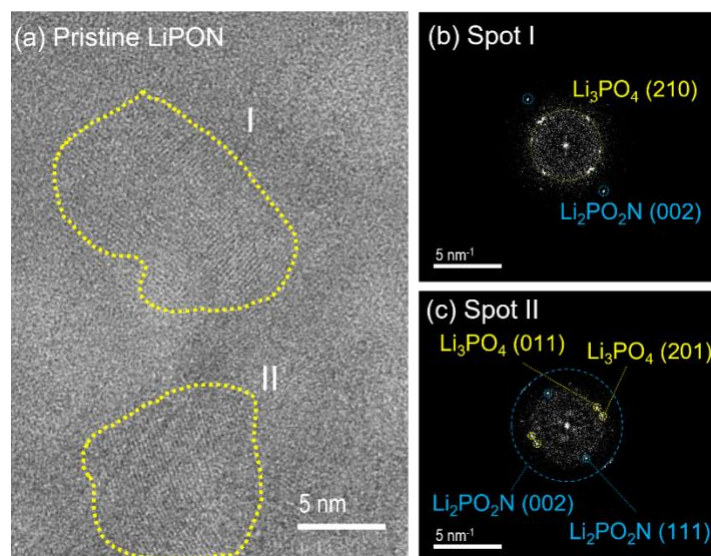
Figure 5.9 Cryo-TEM of pristine LNMO/LiPON. (A) Cryo-TEM image of LiPON in pristine LNMO/LiPON. FFT images of (B) spot I and (c) spot II.
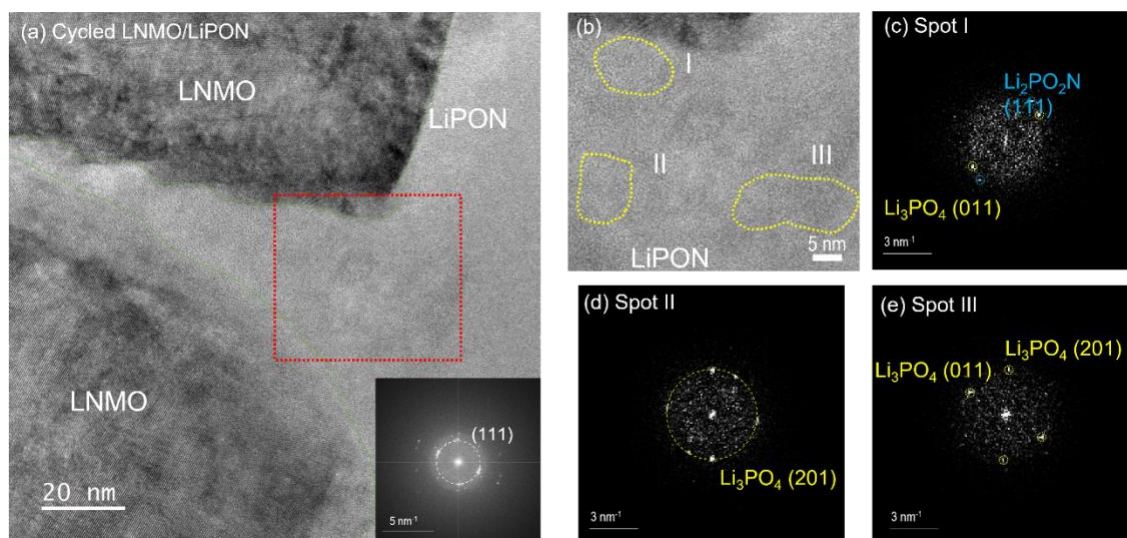
Figure 5.10 Cryo-TEM of cycled LNMO/LiPON. (A) Cryo-TEM image of cycled LNMO/LiPON and (B) magnified image of the area surrounded by red dot lines in (A). FFT images of (C) spot I, (D) spot II, and (E) spot III.

5.3.5 An electrochemically stable and mechanically compatible solid-solid interface

The stability at LNMO/LiPON interface stems from two separate perspectives: *i*) the intrinsic structural resilience of LNMO, and *ii*) the unique characteristics of LiPON. The LNMO material's spinel crystal structure determines its ability to accommodate excess Li. Upon

overlithiation, LNMO experiences a phase transformation from cubic to tetragonal structure while it homes extra Li in the structure without sabotaging the cyclability and interface stability. Spinel analogue anode material, $Li_4Ti_5O_{12}$ (LTO), undergoes a similar phase transformation when extra Li is inserted into the structure while maintaining LTO's highly reversible cycling performance.[166] Contrary to spinel oxides, layered oxides are prone to unfavorable changes with excess Li. LCO suffers from the formation of a disordered phase that comprise of a mixture of Li_2O and CoO between ordered LCO and LiPON during sputtering process. This results in an extra interfacial impedance and can inhibit cycling performance.[45,167] $Li_xNi_{0.8}Mn_{0.1}Co_{0.1}O_2$ (NMC811), another layered cathode material, experiences a 45.5% capacity loss in subsequent cycles after deep discharging to 0.8 V vs. Li/Li^+ in the initial cycle in the liquid electrolyte system.[168] The ability of spinel oxides to withstand surface overlithiation renders LNMO suitable for coupling with LiPON electrolyte, and serves to increase the surface Li chemical potential of the cathode for better interfacing with solid electrolytes.

Three aspects can be considered regarding the uniqueness of LiPON material. The overarching factor is the electrochemical stability of LiPON. Partial decomposition of LiPON is observed after its deposition onto LNMO surface. This indicates a certain extent of chemical incompatibility. However, long-term cycling does not result in additional decomposition of LiPON. Rather, most of the LiPON remains amorphous along the interface. This implies that LiPON is electrochemical stable against a high voltage LNMO cathode. Further EELS analysis at the cycled LNMO/LiPON interface shows no noticeable changes in the P and N chemical environments, which suggests the stability of LiPON's chemistry against highly oxidative potential (Figure 5.11). Such electrochemical stability could be influenced by the increased Li concentration estimated from the NDP results. The ascending Li content across the interface from

LNMO to LiPON region represents a gradually ramping chemical potential, which mitigates the oxidative potential from high voltage LNMO and protects LiPON from further decomposition.[25] Coupling with the analogous chemical gradient feature observed at Li/LiPON interface elsewhere,[42] the presence of gradient interfaces, which exhibits exemplary electrochemical stability, hint on the plausibility of engineering solid-solid interfaces so that drastic chemical potential differences between electrode and electrolyte can be diminished to achieve desired stability. Such features also serve to eliminate the possible effect from space charge at the interface, even though the impact from Li deficient layer in SSE, as proposed in space charge theory, on interfacial transport properties remain inconclusive.[169–171]
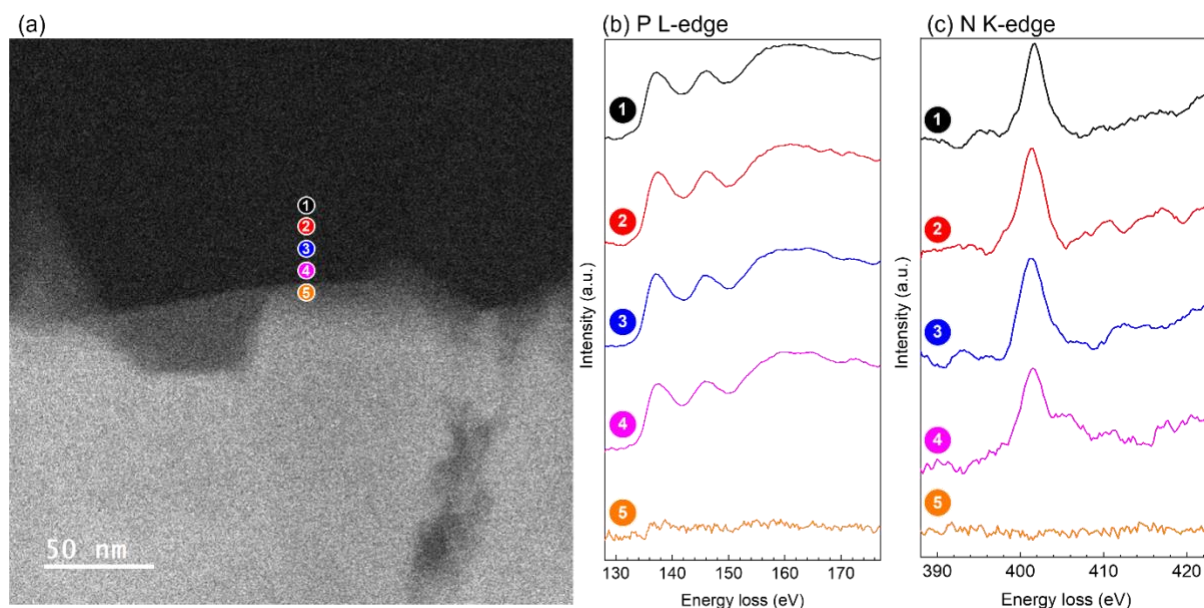
Figure 5.11 Compositional analysis of the cycled LNMO/LiPON interface by EELS. (A) STEM HAADF image of cycled LNMO/LiPON interface. (B) P K-edge and (C) N K-edge EELS spectra at each spot as highlight at the cycled interface in (A).

Another aspect of LiPON being stable against LNMO ties into its mechanical characteristics. Herbert et al. measured the Young's modulus of LiPON by nanoindentation and obtained a value of 77 GPa.[146] This high modulus provides LiPON a rigid characteristic. However,

90

Lee et al. reports a 11% - 13% volume change of L_xNMO cathode upon lithiation from x = 0 to x =2.[152] Given the polycrystalline feature of LNMO cathode, anisotropic stress generated at the interface during such repeated volumetric changes can cause catastrophic impact on LiPON's bulk structural integrity such as cracking or delamination, while none of these issues were observed to occur at the LNMO/LiPON interface. The fact that LiPON retains an intact contact with LNMO after long-term cycling suggests that the LiPON in this study may be a relatively soft material. This is consistent with some observations on the flexibility of LiPON in literature,[53,172] yet further experimental validation is needed.

The last aspect of LiPON's stability against LNMO correlates with its morphological characteristics. LiPON is known for its amorphous structure and dense, pinhole-free feature. Such merits of LiPON give rise to its even coverage over LNMO after deposition and facilitates a uniform overlithiation on an LNMO surface, namely a conformal interface. In the case of a liquid electrolyte system, the CEI tends to be non-uniform in both composition and thickness, due to the hardly controllable mass transfer in a liquid environment, which diminishes the passivation effect of such interfaces. Compared to studies with other solid electrolytes (i.e., $Li_7La_3Zr_2O_{12}$ and Li_6PS_5Cl, etc.), roughness at the pelletized cathode/electrolyte interface can incur inhomogeneity in terms of contact and pressure, resulting in interface non-uniformity.[72,173] Given the compatibility of LiPON against varieties of cathodes, an artificial LiPON layer deposited on a cathode surface could serve as a simple protection strategy to alleviate the interfacial reaction between a less electrochemically stable solid electrolyte and highly oxidative cathode material. Alternatively, employing methodologies for producing glassy material (e.g., via fast quenching) to amorphize conventionally crystalline solid electrolytes through the creation of defects could well steer the morphological features and enhance interfacial stability.

It should be noted that the absence of a carbon conductive agent also helps to achieve the stable cycling performance. Although carbon additives improve electronic conductivity of a cathode or an anode composite electrode, past researches has indicated that carbon additives can accelerate the decomposition of an electrolyte and form CEI on a cathode's surface[174,175] and SEI on an anode's surface,[176] causing capacity degradation of cells. The high electronic conductivity of the carbon also creates an electronic pathway for electrolyte redox reactions to occur. Therefore, it is critical to avoid carbon or minimize its surface area to suppress the kinetics of the electrolyte decomposition.
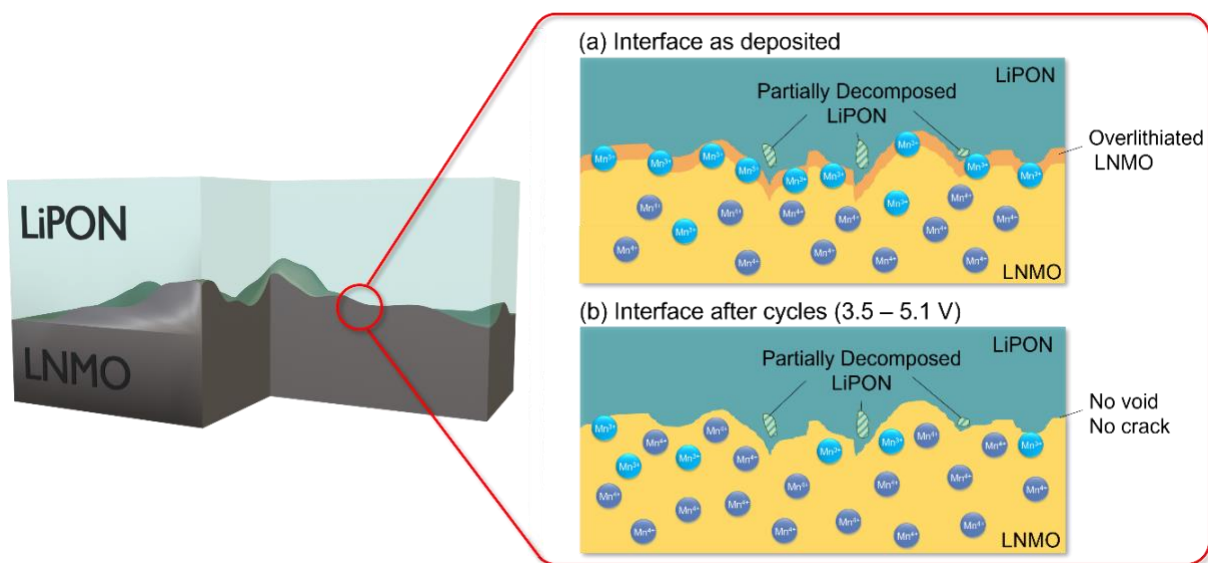
Figure 5.12 Schematic illustration of microscopic LNMO/LiPON interface. At the LNMO/LiPON interface (left), microscopically LNMO/LiPON contact without void and cracks both (A) as deposited and (B) after cycling between 3.5 V - 5.1 V. As deposited interface in (A), overlithiated regions is likely to exist in LNMO, where Mn oxidation state is reduced to 3+. After cycling (B), such area disappears and Mn^{4+} is dominant in overall LNMO. In both interface, partial decomposition of LiPON is observed.

To better illustrate the interface configuration between LNMO and LiPON, a schematic is shown in Figure 5.12 Examinations of an LNMO/LiPON interface using NDP, DFT and cryo-EM yields intriguing results that are closely related to the stability of the materials' interface. An ideal

cathode electrolyte interface requires the electrolyte to remain either chemically or electrochemically stable against the cathode and mechanically robust. An as-formed CEI ought to be uniform and conformal, consisting of species that are electronical insulating and ionically conductive to prevent further decomposition of electrolyte. Finally, the cathode should be able to retain the crystal structure after extended cycling.

5.4 Conclusions

New insights into the interface between LNMO cathode and LiPON solid electrolyte have been gained by combining targeted spectroscopic, microscopic, and computational tools. An overlithiation layer of LNMO at the LNMO/LiPON interface due to LiPON deposition is revealed by NDP, which accounts for the excess capacity during the 1st charge of LNMO. Overlithiated LNMO exhibits a Mn oxidation state change from 4+ to 3+ as confirmed by both DFT prediction and cryo-STEM/EELS examination. The cathode structure is intact under the overlithiation and is not significantly impacted after electrochemical activation. Cryo-TEM further shows a LNMO/LiPON interface with intimate contact that is free of voids and cracks over the course of 500 cycles. STEM/EELS demonstrates that major elements across the interface keep their original chemical bonding environment. The observed conformal and stable interface contributes to the electrochemical stability of LiPON against LNMO. The knowledge gained from additive-free electrodes and its close contact to mechanically and electrochemically compatible SSE demonstrate that the long-term cycling stability of 5 V-class cathode materials is achievable with dedicated interface engineering.

Chapter 5, in full, is a reprint of the material, as it appears in: R. Shimizu*, **D. Cheng***, J. L. Weaver, B. Lu, T. Wynn, M. Kim, G. Zhu, M. Zhang and Y. S. Meng, "Unraveling the stable

cathode electrolyte interface in all solid-state thin-film battery operating at 5V", *Adv. Energy Mater.* 2022, 2201119. The dissertation author was the co-primary investigator and co-first author of this paper.

Chapter 6. Freestanding LiPON: from Fundamental Study to Uniformly Dense Li Metal Deposition Under Zero External Pressure

Lithium phosphorus oxynitride (LiPON) is a well-known amorphous thin film solid electrolyte that has been extensively studied in the last three decades. Despite the promises to pair with Li metal anode and various cathode materials, the presence of rigid substrate and LiPON's unique amorphous, air-sensitive nature set limitations to comprehensively understand its intrinsic properties for future development and applications. This work demonstrates a methodology to synthesize LiPON in a freestanding form that exhibits remarkable flexibility and a Young's modulus of ~33 GPa. Solid-state nuclear magnetic resonance (ss-NMR) and differential scanning calorimetry (DSC) results with unprecedented high signal-to-noise ratio could be obtained with such freestanding LiPON (FS-LiPON), revealing the Li/LiPON interface bonding environments quantitatively and a well-defined glass transition temperature for LiPON. Combining interfacial stress and a seeding layer, FS-LiPON demonstrates a uniform and fully dense Li metal deposition without the aid of external pressure. Such a FS-LiPON film offers new opportunities for fundamental study of LiPON material and associated interfaces, and provides perspectives for interface engineering in bulk solid-state battery.

6.1 Introduction

Recent work has extended beyond bulk structure toward the interfacial stability between electrode materials and LiPON. Despite the knowledge on cathode-associated interfaces in early work[41,45,57] and recent insights gained on Li metal/LiPON interface via the advances of cryogenic electron microscopy (cryo-EM),[42,177] the electro-chemo-mechanical properties of SSE/electrode interfaces have yet to be explored. These are also regarded as critical metrics to determine the mechanical behavior at the interface during cycling, which can alter the stability and the cycle life

of solid-state batteries.[178] However, literature studying the mechanical properties of LiPON has been limited. Herbert et al. measured the Young's modulus of LiPON by nanoindentation and obtained a value of 77 GPa.[146] A similar Young's modulus was documented by Xu et al. using picosecond ultrasonics measurement.[179] Such a modulus could account for its ability to suppress Li dendrite protrusion during cycling and contribute to its remarkable cyclability. Nevertheless, the long-term air exposure of LiPON during nanoindentation measurements and many approximations made during picosecond ultrasonics data analysis create some ambiguity. LiPON's film format also excludes mechanical testing beyond indentation (i.e. tensile, bending) due to presence of a substrate.

Such dilemma associated with the substrate and insufficient active material amount for measurements originates from the conventional synthesis methods of LiPON thin film. In fact, a variety of existing methods are available to synthesize LiPON, including RF sputtering,[37] pulsed laser deposition (PLD),[51] atomic layer deposition (ALD),[180] ammonolysis, inductively coupled plasma (ICP) and ball milling. Despite the diverse compositions of the LiPON variants yielded by different methods (Table 5.1), most of these processes require the use of a solid substrate (i.e., silicon, glass, alumina, or sapphire, etc.) for LiPON to be deposited on, especially for vacuum deposition techniques. Those methods getting around the use of substrate such as ammonolysis, ICP or ball milling suffer either from the altered LiPON properties or the introduction of interfacial impedance between LiPON powders.[181–183] For the sake of enabling further fundamental characterizations, the removal of the substrate during LiPON synthesis will serve as a sound solution. Furthermore, substrate removal will also improve the energy density of thin film solid-state battery, as the substrate usually weighs several to hundreds of times more than the active materials.

Table 6.1 Existing methods for LiPON production.

Synthesis method	Source/precursors	Substrate needed?	Ionic conductivity (25°C)	Notes
Radio Frequency Sputtering[1]	Li_3PO_4	Yes	2.6×10^{-6} S/cm	
Pulsed Laser Deposition[2]	Li_3PO_4	Yes	1.6×10^{-6} S/cm	Rough surface
Atomic Layer Deposition[3]	lithium tert-butoxide, H_2O, trimethylphosphate	Yes	1.45×10^{-7} S/cm	Low growth rate
E-beam Evaporation[4]	Li_3PO_4	Yes	6.0×10^{-7} S/cm	
Ion Beam Sputtering[5]	Li_3PO_4	Yes	2.0×10^{-7} S/cm	Low growth rate
Metal-organic Chemical Vapor Deposition[6]	$Li(C_{11}H_{19}O_2)$, $(C_2H_5)_3PO_4$	Yes	2.95×10^{-7} S/cm	
Ammonolysis[7]	$Li_2O \cdot P_2O_5$ glass, NH_3	No	$10^{-7} \sim 10^{-9}$ S/cm	
Inductively Coupled Plasma[8]	Li_2O, $Li_4P_2O_7$, Li_4SiO_4, Si_3N_4	No	1.0×10^{-6} S/cm	Low LiPON purity, in nanopowder form
Ball Milling[9]	$LiPO_3$ and Li_3N	No	3.0×10^{-7} S/cm	Crystalline LiPON

Inspired by the semiconductor industry, where a photoresist is commonly used as a mask material that can withstand plasma-assisted deposition while being easily removed by organic solvents, herein we introduce a different methodology to synthesize a LiPON thin film that is in freestanding form without a rigid solid substrate. This freestanding LiPON (FS-LiPON) thin film exhibits transparency and a remarkable flexibility. The proposed methodology shows no modification to the LiPON structure, chemical bonding environments, and electronic properties, compared with the substrate-based analogues in literature. Leveraging this form factor, solid-state NMR of Li metal/FS-LiPON sample provides fresh quantitative insights on the interphase formation towards a better understanding of associated stability of Li/LiPON interface. Differential scanning calorimetry (DSC) on FS-LiPON sample gives a more accurate measurement on the glass transition temperature of 207 °C for LiPON. Mechanical testing demonstrates a Young's modulus of ~33 GPa and the remarkable flexibility of FS-LiPON films, opening up the chance of comprehensively studying LiPON's intrinsic mechanical properties using it freestanding form. All the above measurements benefit from the enhanced S/N ratio due to the removal of the

substrate, illustrating the advantage and potential use of FS-LiPON for fundamental studies. With the aid of interfacial stress between at Cu/FS-LiPON and the presence of an Au seeding layer, we further demonstrate electrochemical deposition of uniform and fully dense Li metal under zero external pressure. The combination of interfacial stress and metal seeding layer for enabling uniform Li metal deposition provides new insights on interface engineering in bulk Li metal solid-state batteries.

6.2 Experimental Methods

6.2.1 Photoresist Spin Coating

AZ1512 photoresist (from EMD Performance Materials Corp.) is coated on clean glass substrate by spin coating. The heater temperature for prebake and postbake was set as 100°C. The spinning recipe includes 500 RPM for 20s, 1000 RPM for 20s and 2000 RPM for 60s. The resulting photoresist layer thickness is about 1.7 μm.

6.2.2 Thin Film Deposition

LiPON thin film was deposited on photoresist-coated glass substrate by RF sputtering using a crystalline Li_3PO_4 target (2″ in diameter, from Plasmaterials, Inc.) in UHP nitrogen atmosphere. The base pressure of the sputtering system was 3.0×10^{-6} Torr. LiPON deposition used a power of 50W and nitrogen gas pressure of 15 mTorr. The as-deposited LiPON thin film was 3.7 μm in thickness with a growth rate of ~0.46 Å/s. The copper pads for EIS tests and current collector were deposited by thermal evaporation using copper pellets (from Kurt J. Lesker, 99.99% purity). Growth rate is 1 Å/s. Li metal anode for the Li-Cu cell was deposited by thermal evaporation with a base pressure of 2.5×10^{-8} Torr and growth rate of 3-4 Å/s. The Au seeding layer was deposited

by thermal evaporation using gold pellets (from Kurt J. Lesker, 99.99% purity). Growth rate is 1.5 Å/s.

6.2.3 X-Ray Diffraction

The powder crystal X-ray diffraction was carried out on a Bruker micro focused rotating anode, with double bounced focusing optics resulting in Cu $K_{\alpha1}$ and $K_{\alpha2}$ radiation (λ_{avg} =1.54178 Å) focused on the sample. A sample of FS-LiPON was mounted onto a four circle Kappa geometry goniometer with APEX II CCD detector.

6.2.4 Microscopic Morphology and Chemical Analysis

Scanning Electron Microscopy (SEM) was performed using an FEI Apreo SEM with an electron beam energy of 5 keV and an electron beam current of 0.1 nA. The energy dispersive spectroscopy X-Ray spectroscopy (EDS) was collected using an electron beam energy of 5 keV by the Pathfinder EDS software from Thermo Scientific.

6.2.5 X-ray Photoelectron Spectroscopy

X-Ray photoelectron spectroscopy (XPS) was performed in an AXIS Supra XPS by Kratos Analytical. XPS spectra were collected using a monochromatized Al Kα radiation (hυ = 1486.7 eV) under a base pressure of 10^{-9} Torr. To avoid moisture and air exposure, a nitrogen filled glovebox was directly connected to XPS spectrometer. All XPS measurements were collected with a $300 \times 700\ \mu m^2$ spot size. Survey scans were performed with a step size of 1.0 eV, followed by a high-resolution scan with 0.1 eV resolution, for lithium 1s, carbon 1s, oxygen 1s, nitrogen 1s, and phosphorous 2p regions. A 5 keV Ar plasma etching source was used for surface etching with a

pre-etching for 5 s, etching for 60 s and post-etching for 10 s. All spectra were calibrated with adventitious carbon 1s (284.6 eV) and analyzed by CasaXPS software.

6.2.6 Electrochemical Measurements

A Biologic SP-200 potentiostat was used to measure the electrochemical impedance spectroscopy (EIS) and DC polarization of FS-LiPON. The frequency range for EIS was 3 MHz to 100 mHz with an amplitude of 10 mV and the obtained data fitted with a linear least square fitting method. The constant voltage used for DC polarization is 1V. The setup for electrochemical measurements is shown in the schematic in Supplementary Figure 6.7A and Figure 6.13. To apply external pressure on Li-Cu FS-LiPON cell, a rigid stainless-steel plate ($2\times2\times0.03$ mm^2) was placed between the active region of the cell and the probe during measurements.

6.2.7 Solid-state Nuclear Magnetic Resonance

The NMR measurements performed on Sub-LiPON and FS-LiPON were collected using a 4 mm X/H channel Revolution probe on a 400 MHz (9.4 T) Bruker Biospin Avance Neo, operating at 161.97 MHz for ^{31}P. The samples were packed within a 4 mm pencil-type ZrO$_2$ rotor and spun at 10 kHz. The ^{31}P spectra were collected as a rotor synchronized Hahn echo experiment with a 90° pulse of 2.4 µs (B$_1$ field strength ~104 kHz). Hahn echo experiments were processed from the top of the echo to remove the effects of ring down from the FID. The recycle delays used for the 1D experiments was 25 s.

6.2.8 Differential Scanning Calorimetry

The Differential Scanning Calorimetry (DSC) measurement was conducted with DSC 214 Polyma (Netzsch). The temperature range was from 50°C to 500°C with a heating rate of 10°C /min. The DSC measurement was conducted under N_2 environment. All samples were sealed in aluminum pans in an Argon-filled glovebox to reduce contamination.

6.2.9 Cryogenic Focused Ion Beam/Scanning Electron Microscopy

A FEI Scios DualBeam FIB/SEM equipped with cryo-stage was used to observe the surface and cross-section morphology of plated Li metal in FS-LiPON Li-Cu cell. The operating voltage of electron beam was 5 kV. Emission current of electron beam was set to 25 pA to minimize potential damage of electron beam. A gallium ion beam source was used to mill and thin the sample. The operating voltage of ion beam source was 30 kV. Emission currents of ion beam were chosen for different purposes, i.e., 10 pA for imaging by ion beam, 0.1 nA for cross-section cleaning and 3 nA for pattern milling. To preserve the Li metal pristine morphology, a cryo-stage was used during pattern milling and cross-section cleaning processes, where the temperature of cryo-stage was maintained at around -185°C due to heat exchanging with cooled nitrogen gas.

6.2.10 Nanoindentation

Nanoindentation was performed inside of a Thermo Fisher Scientific Scios 2 DualBeam FIB/SEM using a FemtoTools FT-NMT04 nanoindenter equipped with a Berkovich tip. Measurements of hardness and reduced modulus employed the continuous stiffness measurement (CSM) technique using a displacement-controlled test. Mechanical property values were averaged between displacements of ~60 nm and ~200 nm. Several five-by-five indent arrays were performed

at various locations on FS-LiPON films that were bonded to SEM stubs using epoxy. Tests were performed using a 4 s load-ramp time and a 0.2 s unload-ramp time. When transferring samples from an inert environment to the Scios 2 SEM, samples were exposed to <120s of atmosphere prior to the vacuum conditions inside the SEM.

6.3 Results and Discussions

6.3.1 A Flexible Freestanding LiPON Thin Film

Figure 6.1A depicts the fabrication procedure of FS-LiPON. Before employing RF sputtering, a spin-coating method was used to coat a clean glass substrate with photoresist. Details about the spin coating recipe can be found in the experimental procedure section. LiPON thin film was then deposited onto the coated glass substrate by RF sputtering under N_2 plasma. After RF sputtering, LiPON sample was transferred into a container filled with Dimethyl carbonate (DMC) solvent in an argon-filled glove box. The substrate and LiPON film were fully immersed in DMC for overnight. Photoresist was then dissolved by DMC, after which LiPON film delaminated from the glass substrate and ready for pickup. Unlike the common way of producing LiPON thin film on a solid substrate, this method yields LiPON film in a freestanding form and exhibits transparency and remarkable flexibility as shown in Figure 6.1B. Such characteristics indicate LiPON being a soft material, in stark contrast with previous observations in literature.[146,179] Depending on the substrate size, deposition area and deposition time, the area, thickness and sample amount of FS-LiPON can be controlled following this procedure (Figure 6.2).
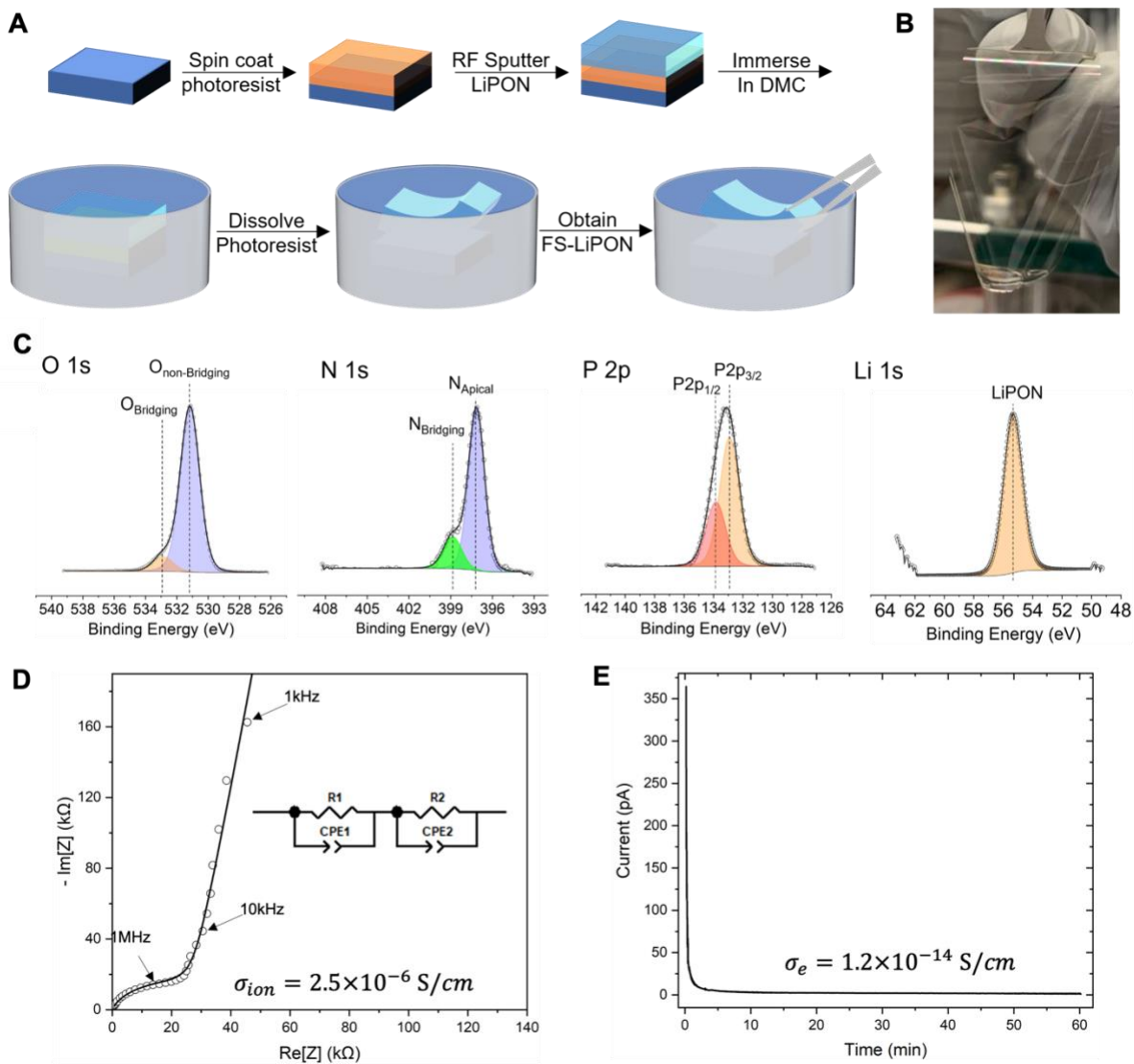
Figure 6.1 (A) Schematic of synthesis procedure for FS-LiPON. (B) Optical photo of a transparent and flexible FS-LiPON thin film. (C) XPS spectra of O 1s, N 1s, P 2p and Li 1s regions of FS-LiPON thin film. (D) EIS plot and (E) DC polarization plot of FS-LiPON.
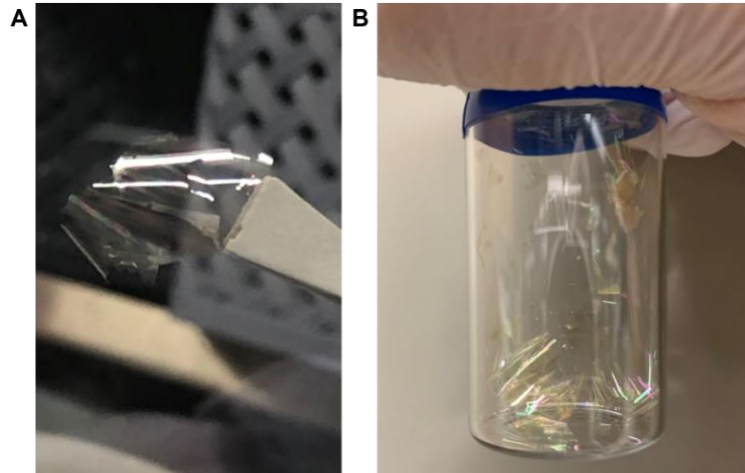
Figure 6.2 The photos of (A) a transparent and flexible FS- LiPON film and (B) FS-LiPON pieces in a capped battle.

A variety of characterizations are performed to ensure that the structure, chemical bonding environments and electrical properties of FS-LiPON are not affected during the above synthesis procedure. The cross-sectional scanning electron microscopy (SEM) and energy-dispersive X-ray spectroscopy (EDS) elemental mapping, shown in Figure 6.3, demonstrate that FS-LiPON retains its fully dense nature in this 3.7-μm-thick film and that P, O, and N elements are uniformly
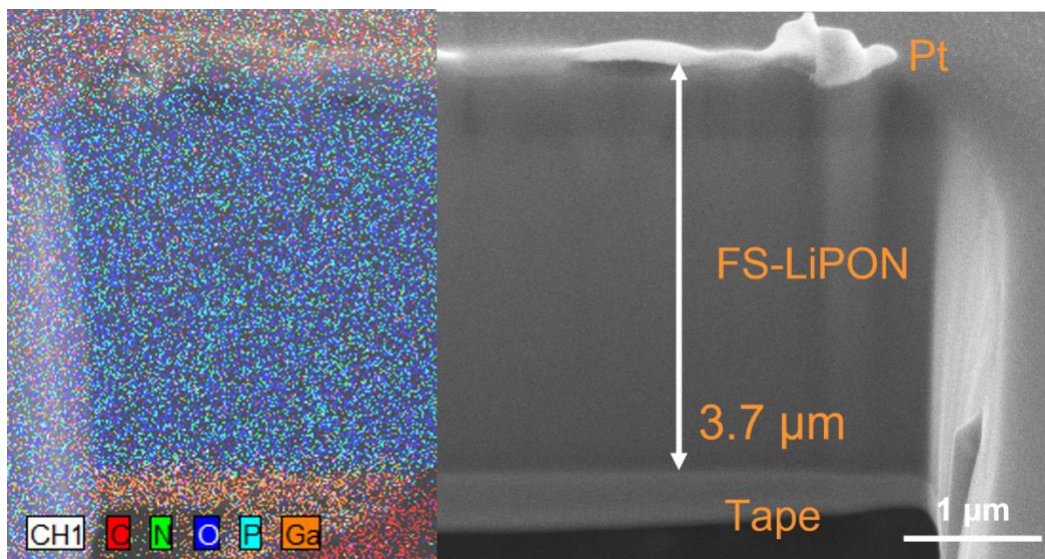
Figure 6.3Cross-section image and EDS mapping of FS-LiPON.

distributed across the sample. Figure 6.4A shows the X-ray diffraction (XRD) results of FS-LiPON, where no diffraction spot is present in the top diagram, and the integrated signal at the bottom only exhibits an amorphous feature around 23 degrees in 2θ, indicating the amorphous characteristic of FS-LiPON. Figure 6.1C displays the XPS result of FS-LiPON thin film, where O 1s, N 1s, P 2p and Li 1s regions manifest consistent features with substrate-based LiPON (Sub-LiPON) that are included in Figure 6.5, Figure 6.6 and in literature,[31,38] illustrating that the chemical bonding environments are retained in the freestanding film. Moreover, the elemental mapping results by
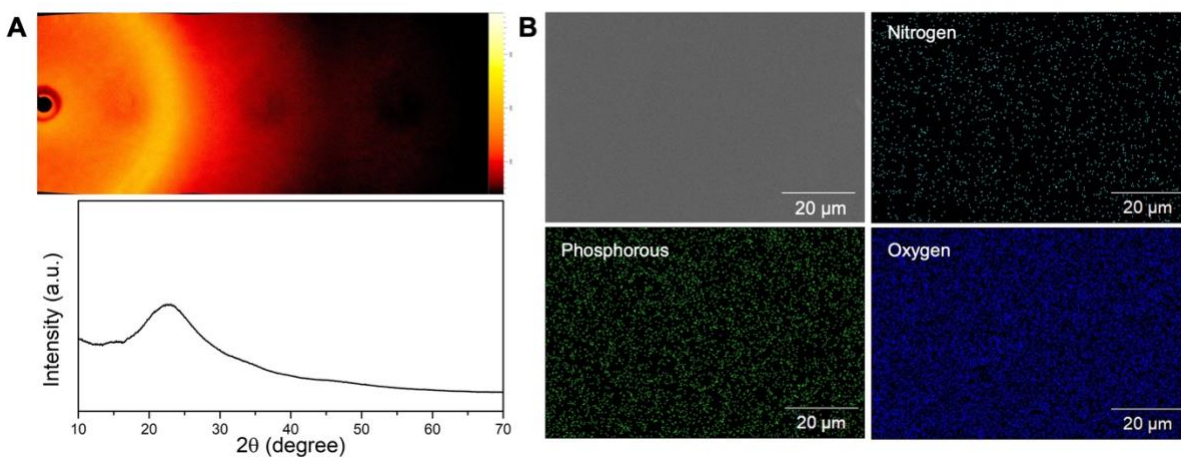
Figure 6.4 (A) XRD pattern of FS-LiPON thin film. (B) SEM image and EDS mapping on the surface of FS-LiPON.

EDS on FS-LiPON surface in Figure 6.4B confirm that N, P and O elements are uniformly distributed on the surface of the FS-LiPON film. Serving as an SSE, LiPON is an ionic conductor whilst an excellent electrical insulator. Electrochemical impedance spectroscopy (EIS) and direct-current (DC) polarization were subsequently employed to examine the electrical properties of FS-LiPON. The EIS spectrum in Figure 6.1D yields an ionic conductivity of 2.5×10^{-6} S/cm for FS-LiPON, consistent with that of Sub-LiPON shown in Figure 6.7 and is better than the LiPON analogues produced by PLD and ALD methods.[51,180] DC polarization plot in Figure 6.1E gives an electronic conductivity of 1.2×10^{-14} S/cm, on the order of Sub-LiPON as reported in literature.[38,184]

Based on above results, FS-LiPON exhibits consistent properties with Sub-LiPON regardless of its freestanding form.
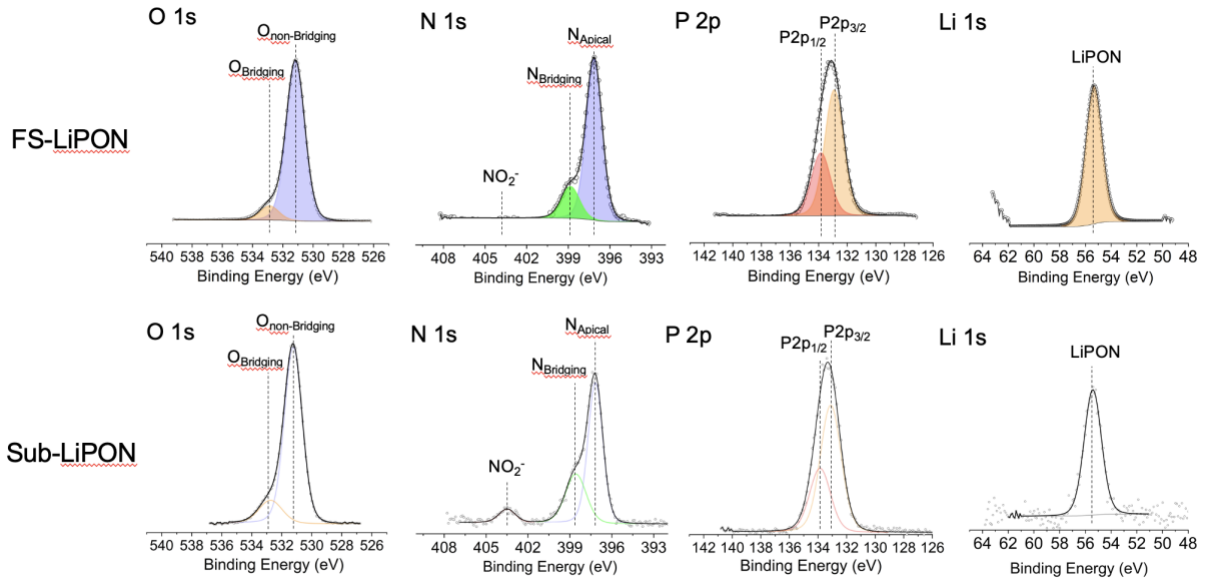
Figure 6.5 XPS spectra of O 1s, N 1s, P 2p and Li 1s regions collected on FS-LiPON and sub-LiPON thin film, respectively. Note that the peak located at 403.5 eV in N 1s region of sub-LiPON can be attributed to NO^{2-} species, which is not present in the FS-LiPON.
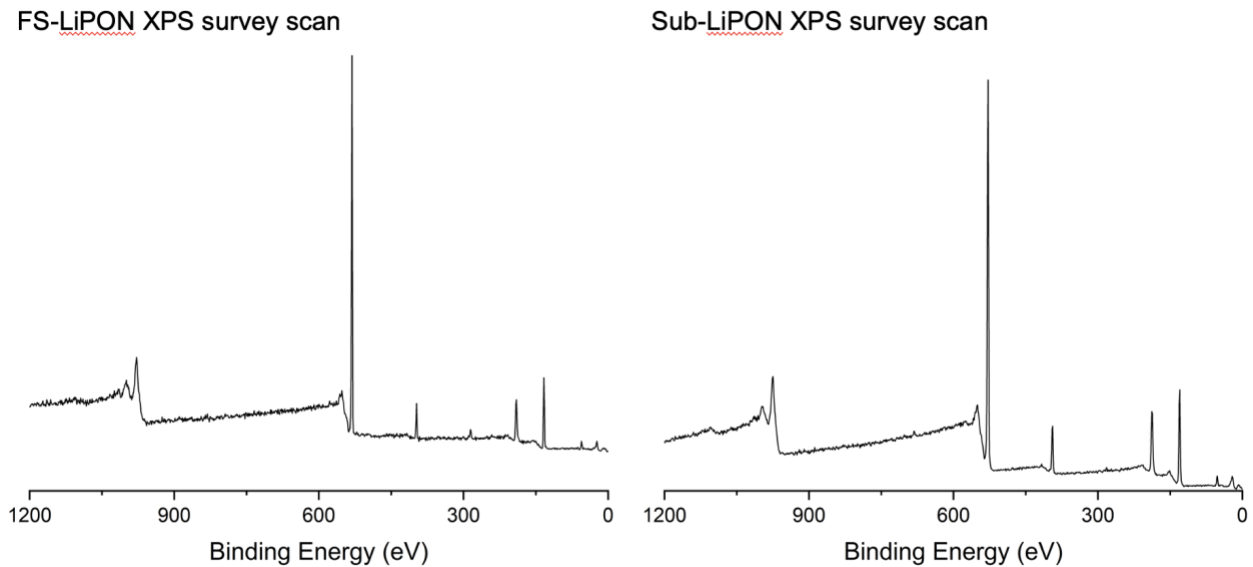
Figure 6.6 XPS survey spectra of FS-LiPON and sub-LiPON films, showing an identical chemical environment.
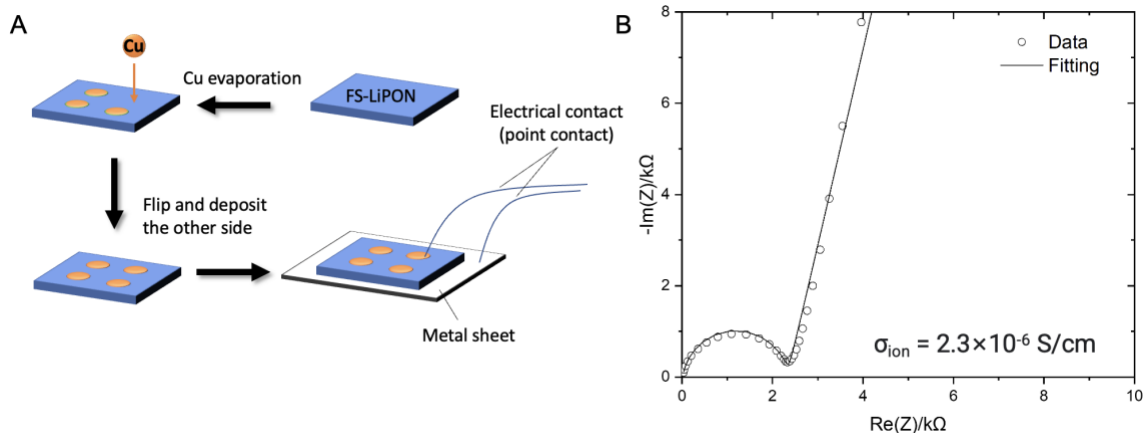
Figure 6.7 (A) Testing configuration for the EIS measurement. (B) EIS result collected on sub-LiPON.

6.3.2 New Opportunities for Fundamental Study of LiPON

The Li/LiPON interface remains one of the most important interfaces in solid-state battery field, demonstrating extraordinary electrochemical stability.[40,42] As a model example to demonstrate the advantage of applying FS-LiPON for spectroscopic characterization, ss-NMR was performed on Li/FS-LiPON sample and the results are shown in Figure 6.8A-C. The Li/FS-LiPON sample was prepared by depositing Li metal on FS-LiPON film using thermal evaporation. Figure 6.8A shows the ^{31}P magic angle spinning (MAS) NMR spectra of FS-LiPON and Li/FS-LiPON. A high signal-to-noise ratio of the NMR spectra was obtained, attributed to the increased sampling volume permitted by freestanding form of the samples. Based on the previous assignments on FS-LiPON,[53] four different structural units are identified in each spectrum, including orthophosphate tetrahedra PO_4^{3-} (Q^0_0), $P_2O_7^{4-}$ dimers (Q^1_0), bridging-N $P_2O_6N^{5-}$ dimers (Q^1_1) and apical-N PO_3N^{4-} units (Q^0_1). A clear difference regarding the content of these structural units is shown in Figure 6.8B. The Li/FS-LiPON sample shows an increase (13%) of Q^0_0 units relative to the FS-LiPON sample at the expense of PON units (Q^0_1 and Q^1_1). Such increase of PO_4^{3-} content indicates that a large amount of Li_3PO_4 components were generated between Li metal and LiPON as a result of

107

Units	Connectivity	FS-LiPON	Li metal/ FS-LiPON	Δ%
	Q^0_0	47%	60%	+13%
	Q^1_0	5%	3%	-2%
	Q^1_1	33%	26%	-7%
	Q^0_1	15%	11%	-4%
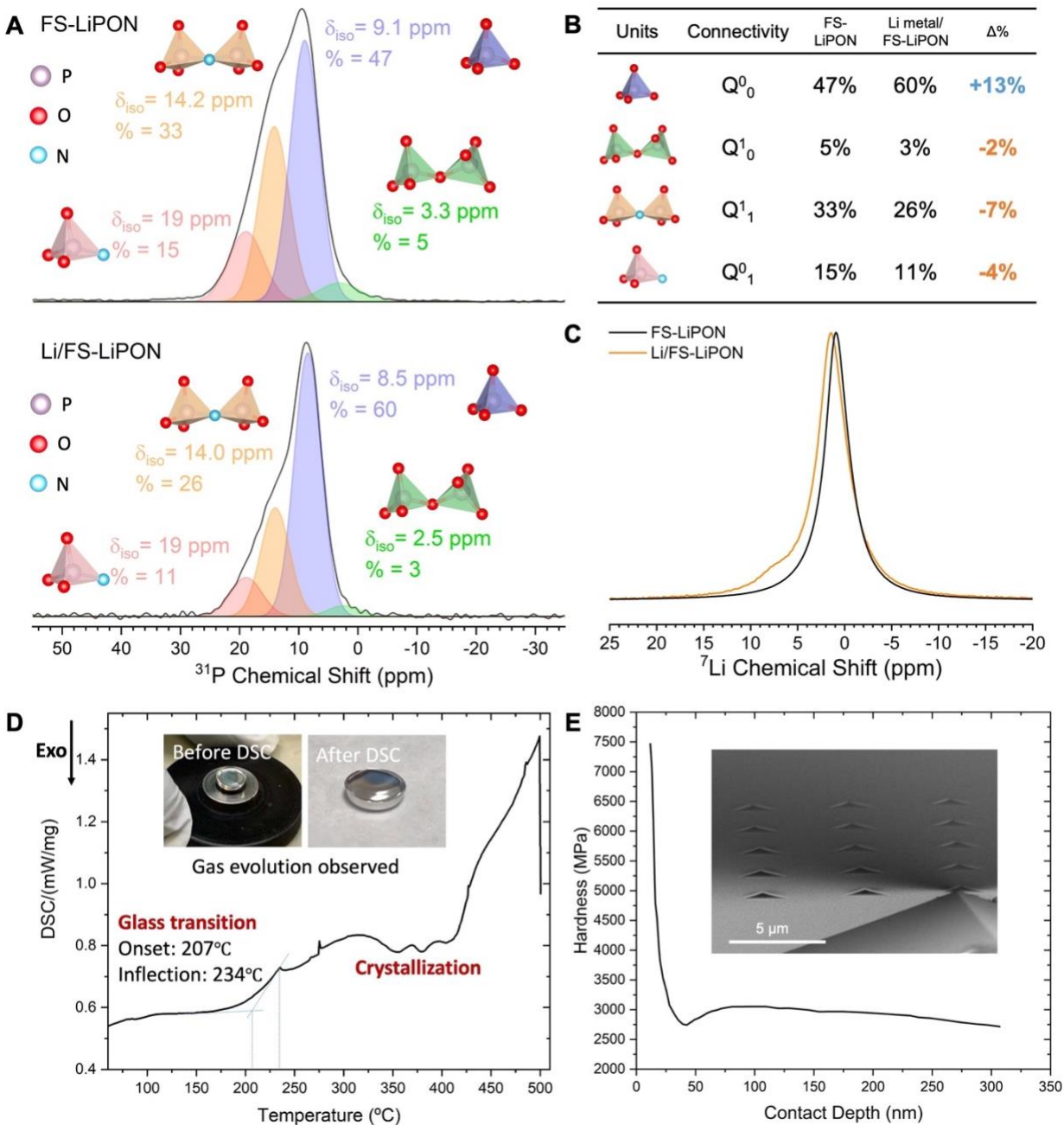
Figure 6.8 (A) ^{31}P MAS NMR spectra of FS-LiPON and Li/FS-LiPON films. The spectrum of FS-LiPON was a reprint of our previous work[53], used here for comparison. (B) Structural unit component differences based on NMR deconvolution. Q^0_0 stands for the orthophosphate tetrahedra PO_4^{3-} units, Q^1_0 stands for the bridging-O $P_2O_7^{4-}$ dimer units, Q^1_1 stands for the bridging-N $P_2O_6N^{5-}$ dimer units and Q^0_1 stands for the apical-N PO_3N^{4-} units. (C) ^7Li MAS NMR spectra of FS-LiPON and Li/FS-LiPON (D) DSC analysis of FS-LiPON film. The inset photos show the gas evolution due to DSC measurement. (E) Film hardness values measured via continuous stiffness measurement (CSM) indentation up to ~10% of the film thickness. Inset image shows the indents array on FS-LiPON during the nanoindentation experiment using a Berkovich indenter.

interface formation, consistent with our previous observation via cryo-EM.[42] The decrease of other structural units such as bridging-O configuration (Q^1_0), bridging-N configuration (Q^1_1) and apical-N configuration (Q^0_1) in turn facilitate the formation of interface components including Li_3N and Li_2O between Li metal and LiPON. ^{7}Li MAS NMR spectrum of Li/FS-LiPON in Figure 6.8C shows a clear shoulder around 7.5 ppm compared with FS-LiPON, indicating Li_3N formation at the interface.[185] The slight peak shift shown in Figure 6.8C may be due to dynamical heterogeneities between the interfacial Li ions and Li ions deep in LiPON. Li metal was also clearly observed at 264 ppm in Figure 6.9.
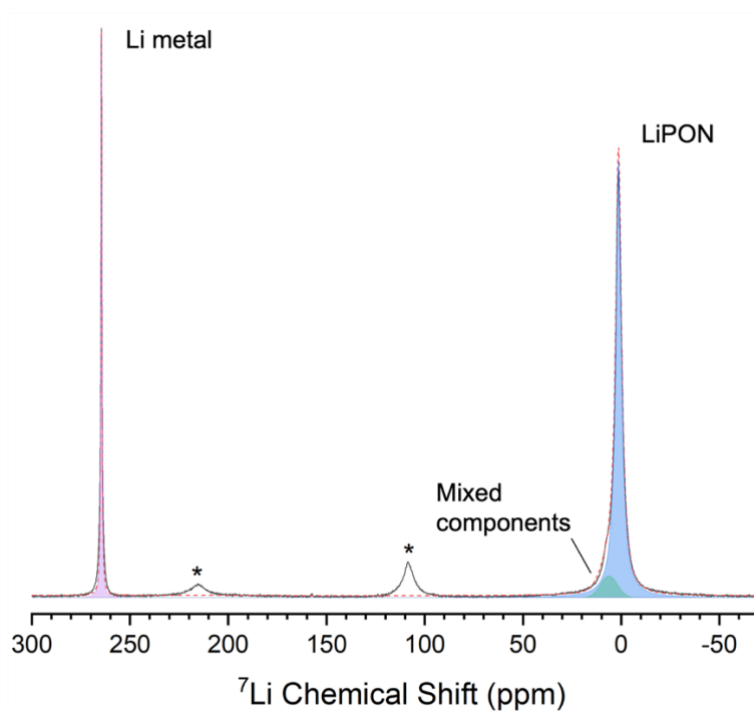
Figure 6.9 Li[7] MAS NMR spectrum showing the presence of Li metal in Li/FS-LiPON sample.

Previous observations by electron microscopy probed the spatial distribution of interface components between Li metal and LiPON,[42,177] while above ss-NMR results of Li/FS-LiPON sample provide quantitative insights on the content of interface components, revealing the amount of Li_3N and Li_3PO_4 formation as the interface products. The peak shift in ^{7}Li MAS NMR spectra

suggests an enhanced lithium kinetics in Li/FS-LiPON sample, likely contributed by the interface components such as Li_3N. The coupling of ss-NMR results with cryo-EM observation have depicted a more complete view of Li/LiPON interface both compositionally and spatially. As-formed interface components such as Li_3N, Li_2O and Li_3PO_4 not only serves as a passivation layer to prevent LiPON from being continuously reduced by Li metal, but also improves the kinetics at the interface to potentially facilitate uniform lithium transport and nucleation.

The format of FS-LiPON also permits thermal property analysis. LiPON is known to be a glassy material for which the glass transition temperature is one of the most important metrics to determine its metastable states and application environments. Nevertheless, due to the limitation of active material for measurement, previously documented trials using DSC to examine the glass transition temperature of Sub-LiPON failed to capture clear transition behaviors.[186] To this end, DSC was conducted on FS-LiPON. Results in Figure 6.8D show an obvious glass transition with an onset temperature of 207 °C and inflection around 234 °C, consistent with LiPON glass transition temperature studied using spectroscopic ellipsometry.[187] Subsequent thermal response further captured the crystallization process of LiPON, along with the gas evolution observed during heating (inset images in Figure 6.8D). DSC results suggest that a proper temperature range to handle LiPON falls below 325 °C. Extra consideration needed to be taken when heat treatment is performed on LiPON-related samples.

Outlooking the potential of FS-LiPON in the fundamental research, more chances are opened up to investigate the intrinsic properties of LiPON by mechanical tests. Note that it is essential to maintain an inert environment during the mechanical examination of LiPON, as Figure 6.10 shows that FS-LiPON went through stiffening due to air exposure after 3 days.
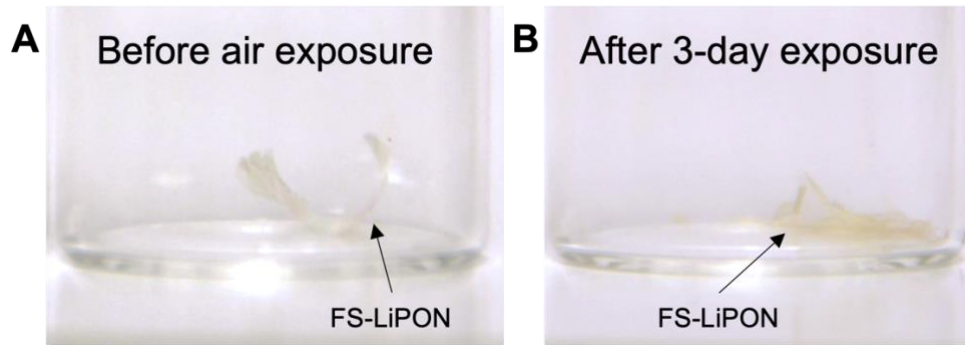
Figure 6.10 Photos of the same piece of FS-LiPON film before air exposure (A) and after air exposure (B), showing the film shape change due to stiffening.

Figure 6.8E display the nanoindentation results collected within a vacuum chamber. The hardness values were plotted against contact depth of the indenter into FS-LiPON from continuous stiffness measurement (CSM), with statistics collected from over 100 indentation locations (inset image in Figure 6.8E shows the indents array at one sampling region). Nanoindentation gives an average hardness value around 2.7 GPa of FS-LiPON in the displacement range from 50 nm to 200 nm. The hardness values below 50 nm were primarily surface effect and have been excluded when determining the film hardness. Such a hardness of FS-LiPON is lower than the previously reported value of 3.9 GPa on sub-LiPON.[188] Based on the mathematical methods developed by Ma et al.[189] to determine Young's modulus from hardness, we obtained an average Young's modulus of FS-LiPON around 33 GPa, in contrast to the previously reported value of ~80 GPa for sub-LiPON.[188] It has been documented that vacuum deposition process commonly generates residual stress within thin film since the substrate may experience thermal expansion, contraction, or lattice mismatch, etc. during the deposition.[190] Specifically, sputtering process tends to generate compressive residual stress in the deposited thin film, which can affect the mechanical properties of thin films, such as increased hardness and Young's modulus.[191] Therefore, the removal of substrate for FS-LiPON has potentially resulted in stress release within LiPON film, which leads to diminished

hardness and Young's modulus as seen. Such observation also suggests the importance to quantify residual stress in LiPON film before determining its mechanical properties.
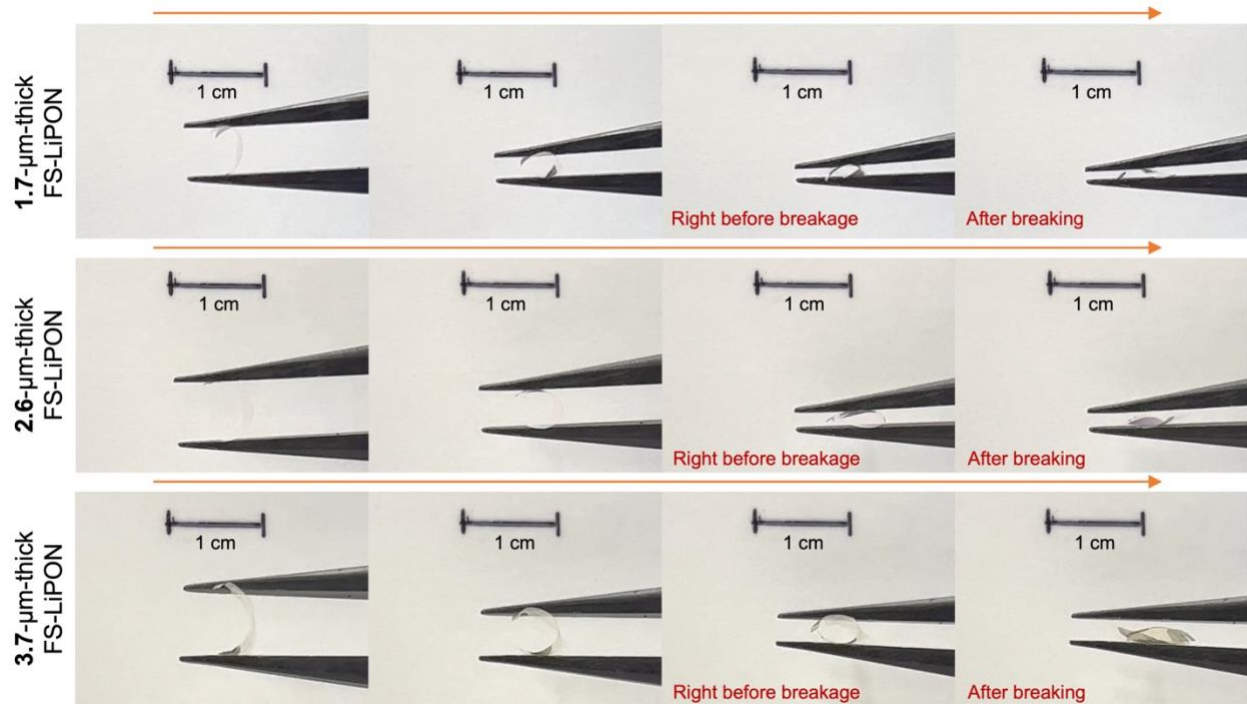
Figure 6.11 Time-lapse series of images during the flexibility test on FS-LiPON films with thicknesses of 1.7 μm, 2.6 μm and 3.7 μm, respectively.

As FS-LiPON film manifests a flexible feature, a series of flexibility testing were performed on FS-LiPON film to qualitatively understand the relationship between flexibility and film thickness. Results are shown in Figure 6.11, where films of varied thicknesses (1.7 mm – 3.7 mm) were taken for the bending test to examine the flexibility. A flathead tweezer was used to apply force on the FS-LiPON films whilst a video was taken to record the bending and breakage of the film. As the time-lapse series of images shown in Figure 6.11, all the FS-LiPON films exhibit remarkable flexibility upon bending. Right before film breakage, the 1.7-mm-thick film shows a high extent of bending compared with the 3.7-mm-thick film, indicating a higher flexibility.

Above results again illustrate the potential of using this freestanding film to obtain native properties of LiPON material itself. Regarding the mechanical properties, further tests such as

tensile test, compression test, etc. can be performed on this FS-LiPON, which would otherwise be impossible to conduct on Sub-LiPON.

6.3.3 Electrochemical Activity of FS-LiPON

Apart from the intrinsic properties, FS-LiPON is also demonstrated to be applicable in electrochemical devices. A FS-LiPON Li-Cu cell was fabricated using the configuration shown in Fiugre 4.12A, where Cu and Li electrodes with the same designed area were aligned across FS-LiPON film. As-fabricated Li-Cu cell harnesses the flexible nature of FS-LiPON as shown in Figure 6.12B. The flexibility of the cell was further demonstrated in Figure 6.12C, where the cell was bent by the tweezer while still able to sustain Li metal plating and stripping capability afterwards. After cell fabrication, the cell was tested using the configuration in Figure 6.13. Figure 6.12D shows the voltage curve of the Li-Cu cell during constant-current measurement. When a current of -50 nA is applied, the cell exhibits a voltage dip and reaches an overpotential of ~-1V, after which a stable plating process proceeds. When altering the current direction, a stripping curve feature is obtained. The cell demonstrated a stable plating and stripping over 13 cycles without short-circuiting, indicating the ability of FS-LiPON to shuttle lithium ions. The relatively high overpotential is likely caused by the resistance to deformation of the Cu current collector whist Li metal nucleates and grows. Apart from the nucleation barrier of Li metal, there is extra mechanical work needed to overcome the Cu deformation. It is noteworthy that owing to the unique configuration of FS-LiPON Li-Cu cell, no external pressure was applied to the cycled cell.
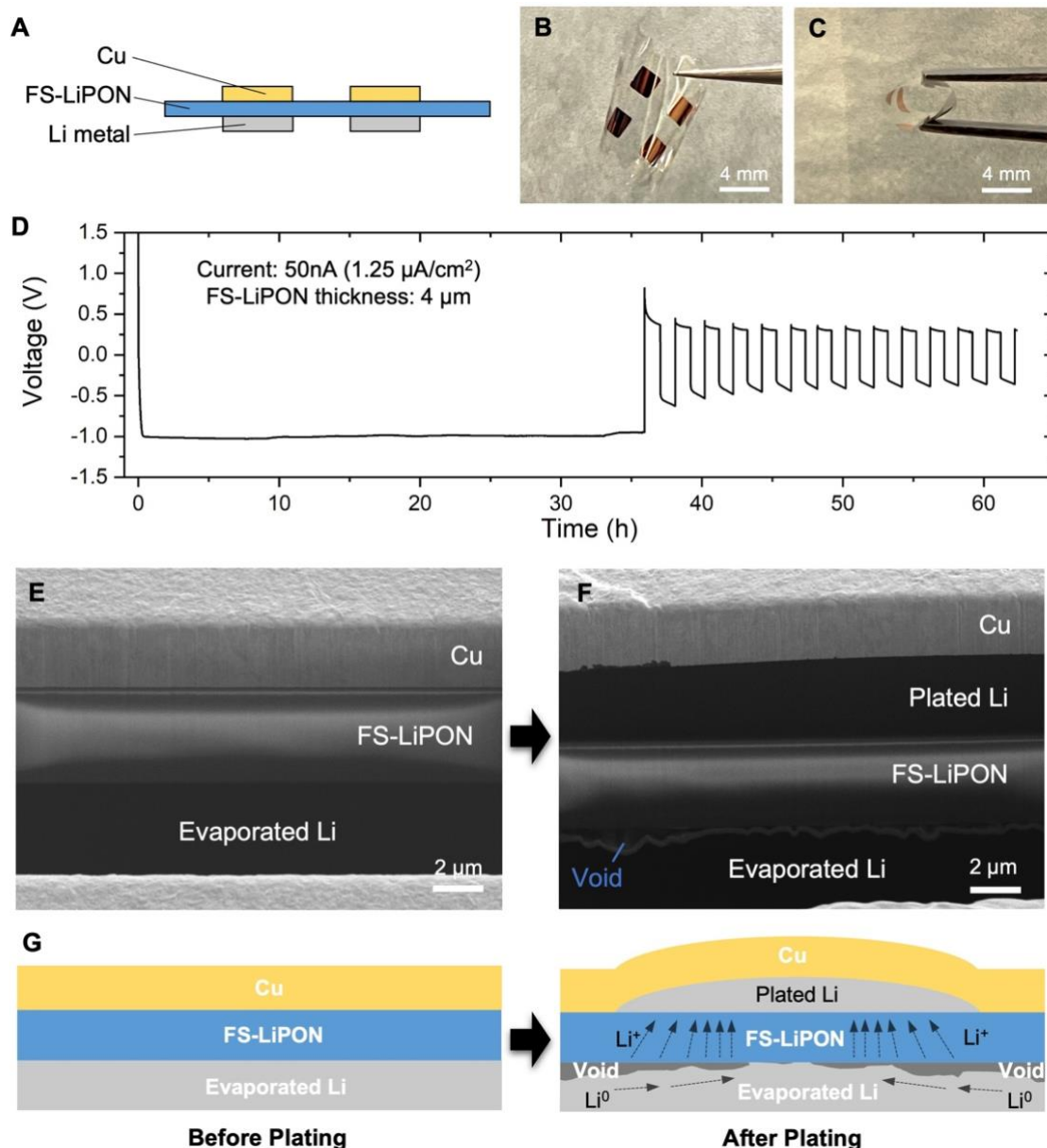
Figure 6.12 (A) Cross-section schematic of the FS-LiPON Li-Cu cell. Photos of FS-LiPON Li-Cu cell from top view (B) and upon bending (C). (D) Voltage curve of Li metal plating and stripping in a FS-LiPON Li-Cu cell. Cross-section cryo-FIB/SEM images of Li-Cu cell before Li metal plating (E) and after Li metal plating (F). The plated capacity in (F) is ~0.31 mAh/cm^2. (G) Schematic showing the proposed non-uniform void formation mechanism during Li metal plating.

The plated Li metal morphology in FS-LiPON system was then examined by cryogenic focused ion beam/scanning electron microscopy (cryo-FIB/SEM). Figure 6.12E displays the cross-section morphology of pristine Li-Cu cell, where no extra layer is observed between Cu and FS-

114

LiPON before plating and the evaporated Li metal on the other side of FS-LiPON appears fully

dense. Note that cryogenic protection during FIB milling is crucial to preserve the pristine

morphology and chemistry of Li metal, as reported elsewhere before[66] and demonstrated in Figure

6.14. After a constant current plating, Li-Cu cell shows a dense Li layer with dark contrast between
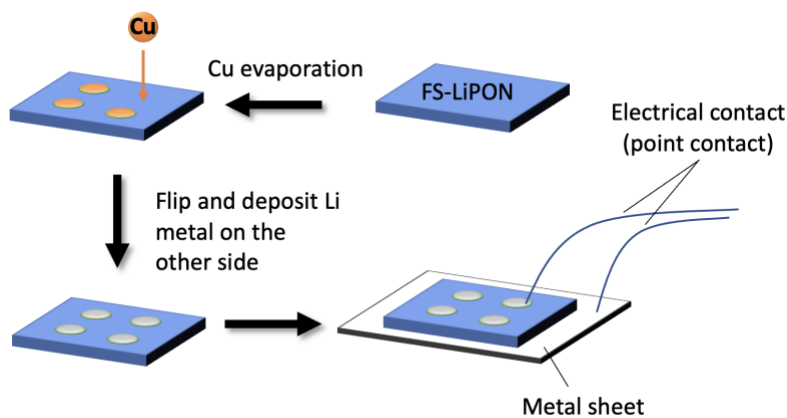
Figure 6.13 Schematic of testing configuration for Li-Cu FS-LiPON cell cycling.
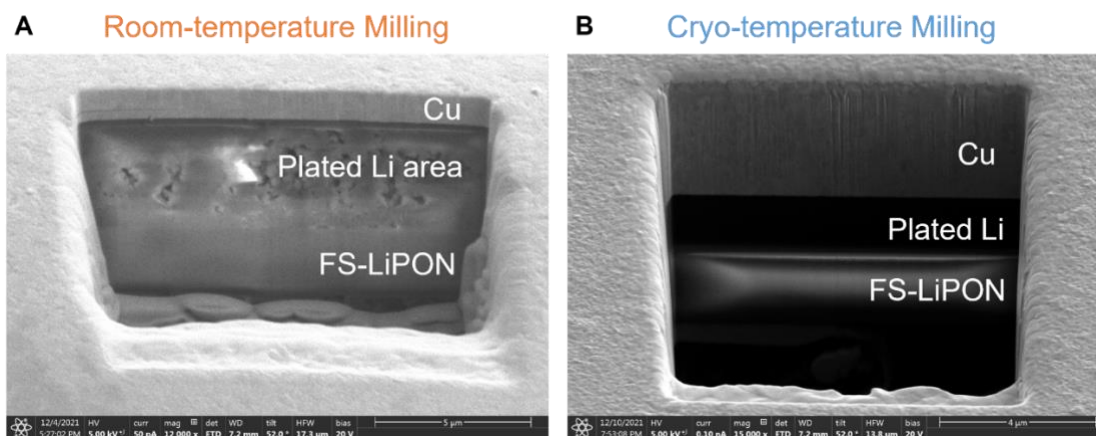
Figure 6.14 Cross-section FIB/SEM of the Li-Cu cell with ion milling performed at room
temperature (A) and cryogenic temperature (-180°C). Morphology and contrast of plated Li metal
in (A) have been changed due to the lack of cryogenic protection compared with (B).

Cu and FS-LiPON in Figure 6.12F. Associated Li-Cu cell voltage curve is plotted in Figure 6.15.

EDS mapping on a plated Li-Cu cell in Figure 6.16 illustrates the presence of Cu, P, O and Ga

over corresponding regions. Due to the inability of regular EDS detectors to distinguish Li signal,

the absence of EDS signal in the dense layers between Cu and FS-LiPON, and in the evaporated Li metal region suggests the existence of plated Li metal above FS-LiPON. Such features indicate a fully dense Li metal electrochemical deposition was realized by this FS-LiPON configuration when no external pressure was present.
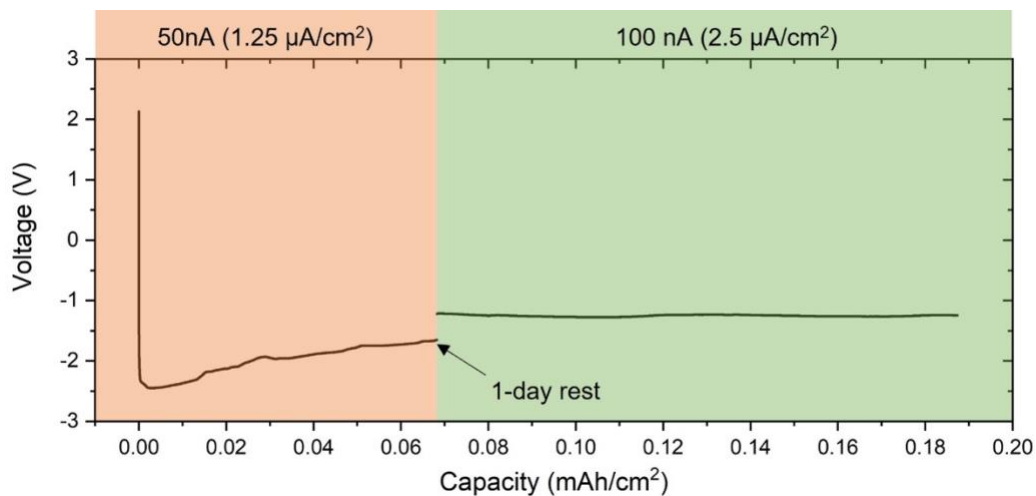
Figure 6.15 Voltage curve of Li metal plating with 1-day rest step.
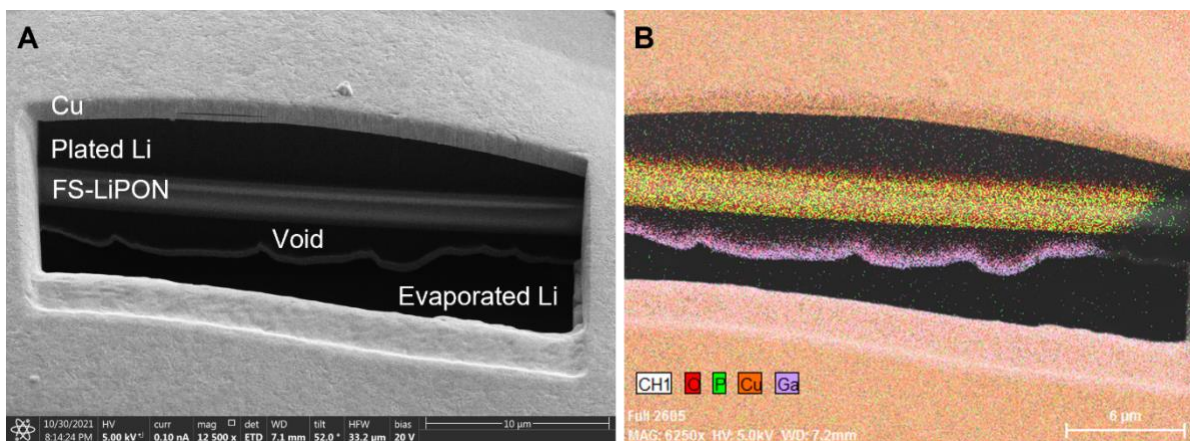
Figure 6.16 (A) Cross-section cryo-FIB/SEM image of the Li-Cu cell after plating. (B) EDS mapping of the corresponding area in (A).

Intriguingly, in Figure 6.16 a void region was observed between FS-LiPON and evaporated Li metal, as hinted by the aggregation of Ga signal that is commonly caused by redeposition during FIB milling and that is prevalently found at the bottom of void region after FIB milling.[42] A similar void feature is also observed in Figure 6.12F, where a gap presents between FS-LiPON and

evaporated Li. Though the theoretical thickness of plated Li metal is calculated to be 1.5 μm based on the areal capacity, the observing region shows a plated Li metal thickness around 4 μm in Figure 6.12F. Top-view SEM image in Figure 6.17 displays various bumps distributed over the Cu surface after plating. Figure 6.12G delineates the plating process occurring in Li-Cu cell without pressure control. Before plating, each constituent in the cell is distinguishable by the well-defined interfaces. After plating, plated Li metal forces up the Cu layer around the initial nucleation site, while the non-uniform lithium-ion flux within FS-LiPON drives lithium atoms around the vicinity of the nucleation site to migrate and compensate the metallic lithium reservoir right under the nucleation site. Therefore, void regions are formed around the nucleation site after plating is completed. Above results suggest that Li metal plating is non-uniform across the FS-LiPON when cycling without external pressure. However, wherever it is plated between Cu and FS-LiPON, Li metal remains fully dense.
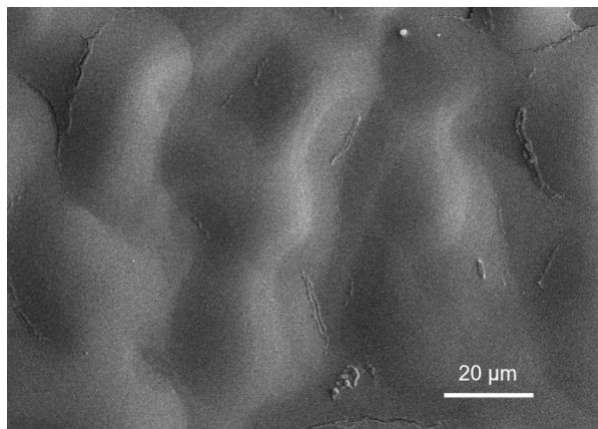
Figure 6.17 Top-view SEM image of Cu surface on the Li-Cu cell after Li metal plating.

From a side view, the electrochemical deposition of Li metal in liquid electrolyte has long been problematic due to the uncontrollable mass transfer, non-uniform nucleation, and continuous growth of solid electrolyte interphase (SEI), which render the deposited Li metal torturous and wisker-like.[84,192] The electrochemically deposited Li metal in other SSE systems (i.e. $Li_7La_3Zr_2O_{12}$

and Li₆PS₅Cl, etc.), however, appears fully dense regardless of dendrite formation issues. Such morphological differences are likely due to the presence of external pressure on the order of several MPa in SSE system.[47,193]

6.3.4 Enabling Fully Dense, Uniform Li Deposition Without External Pressure

Analogous to the cases of other solid electrolyte systems, fully dense Li metal plating has also been demonstrated in FS-LiPON system. Nevertheless, it is noteworthy that there is no external pressure applied on the LiPON system when the fully dense feature of plated Li is obtained, suggesting the possible presence of interfacial stress that could act as internal pressure to promote Li metal yielding and facilitate subsequent dense Li metal deposition. Previous work by Motoyama et al. proposed a model to simulate the interfacial stress between Li metal and Cu current collector after plating, where they used an imaginary Li metal sphere and estimated the radial stress on Li metal surface based on Hoop stress formula.[194]

Employing the similar stress analysis model shown in Figure 6.18A, we obtained the formula as follows:

$$P_i = \frac{\varepsilon_{Cu} E_{Cu}}{(1 - \nu_{Cu})} \cdot \left\{ \frac{3(r_i + t)^3}{2[(r_i + t)^3 - r_i^3]} - \frac{\nu_{Cu}}{1 - \nu_{Cu}} \right\}^{-1} \qquad (4.1)$$

where P_i is the interfacial stress between Li and Cu, ε_{Cu} is strain in the circumferential directions, E_{Cu} is Young's modulus of Cu, t is the thickness of Cu, r_i is the radius of Li metal imaginary sphere, κ is the curvature of Cu, ν_{Cu} is the Poisson's ratio of Cu. The input values of above parameters were extracted from Figure 6.19 and listed in Figure 6.20. Figure 6.18B shows the Cu strain and resulting interfacial stresses in the Li-Cu cells with different Cu thickness,

ranging from 0.151 GPa to 0.503 GPa as Cu strain ramps from 0.024 to 0.052. Obtained stresses

herein are hundreds of times higher than the external pressure applied on bulk SSE analogues.
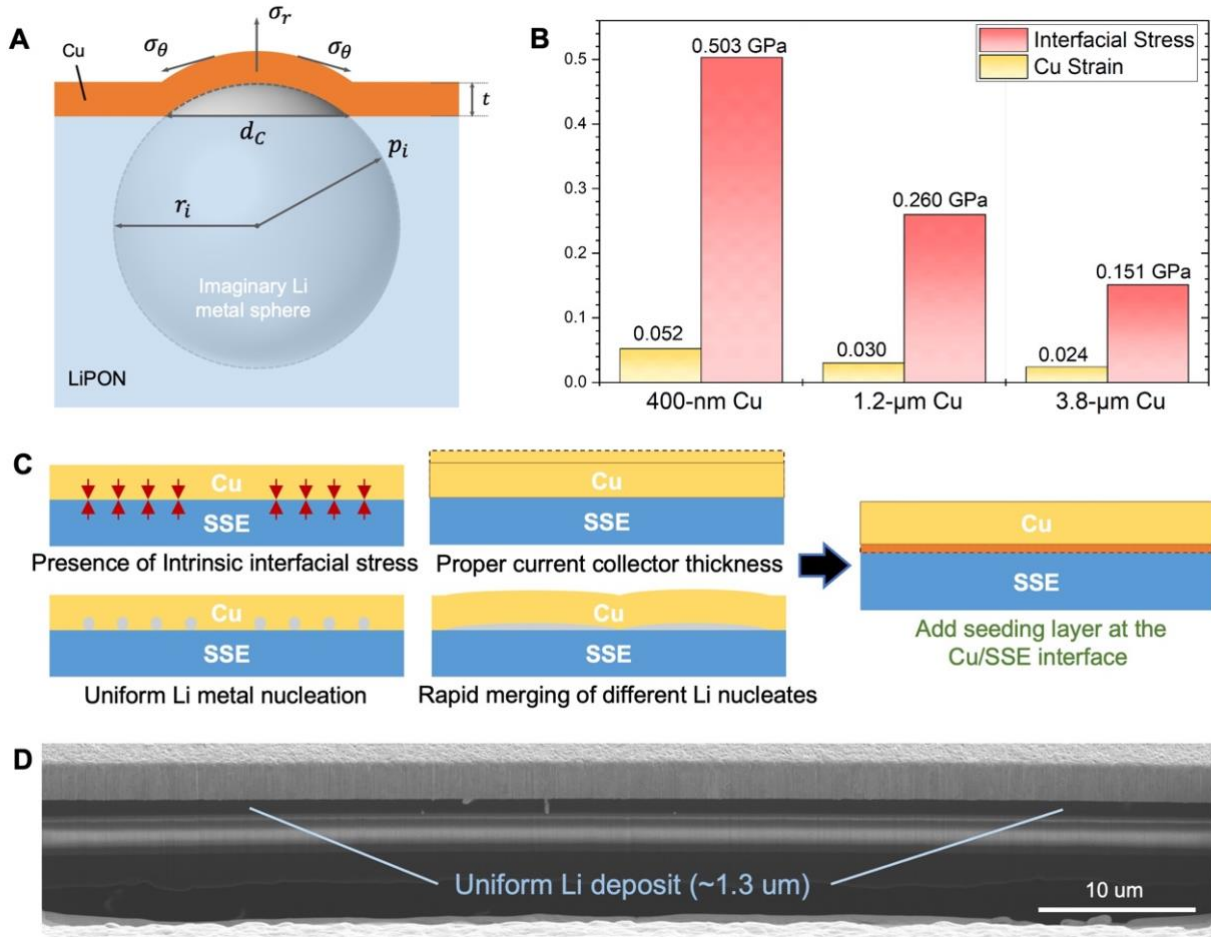
Figure 6.18 (A) Schematic of the interface model for interfacial stress simulation, where P_i is the interfacial stress between Li and Cu, σ_θ is the stress on Cu in the circumferential directions, σ_r is the stress on Cu in the radial direction, t is the thickness of Cu, d_c is the length of the chord marked in the Li sphere underneath the Cu dome region, r_i is the radius of Li metal imaginary sphere. (B) Cu strain and simulated interfacial stress in Li-Cu cell with regard to different Cu thicknesses. (C) Proposed principles and solution to achieve uniform Li metal deposition in solid system. (D) Cryo-FIB/SEM image showing uniform Li deposition realized by adding Au seeding layer in FS-LiPON Li-Cu cell.
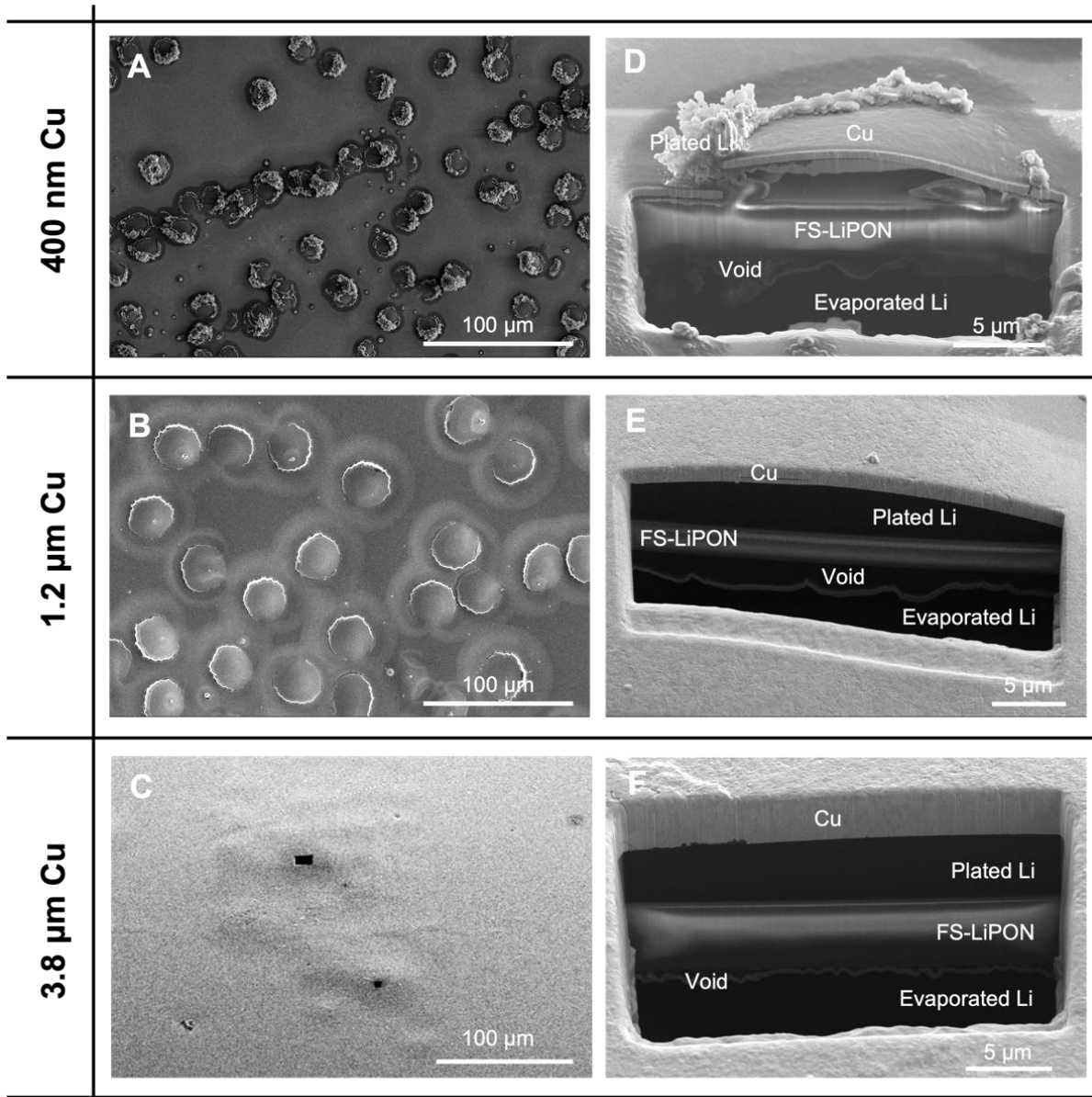
Figure 6.19 Top-view and cross-section SEM images of Li-Cu cell with different Cu thicknesses.

$$P = \frac{\varepsilon_{Cu}E_{Cu}}{(1-v_{Cu})} \cdot \left\{ \frac{3(r_i + t)^3}{2\left[(r_i + t)^3 - r_i^3\right]} - \frac{v_{Cu}}{1 - v_{Cu}} \right\}^{-1}$$

ε_{Cu}: Strain in the circumferential directions
E_{Cu}: Young's modulus of Cu CC
t: Thickness of Cu CC
d_C: Chord length inside Li sphere under Cu
r_i: Radius of Cu CC imaginary sphere
κ: Curvature of Cu CC
v_{Cu}: Poisson's ratio of Cu

	400 nm Cu	1.2 µm Cu	3.8 µm Cu
ε_{Cu}	0.052	0.030	0.024
E_{Cu} (GPa)	130	130	130
t (µm)	0.4	1.2	3.8
r_i (µm)	16.036	54.054	227.273
v_{Cu}	0.34	0.34	0.34
σ (GPa)	0.503	0.260	0.151
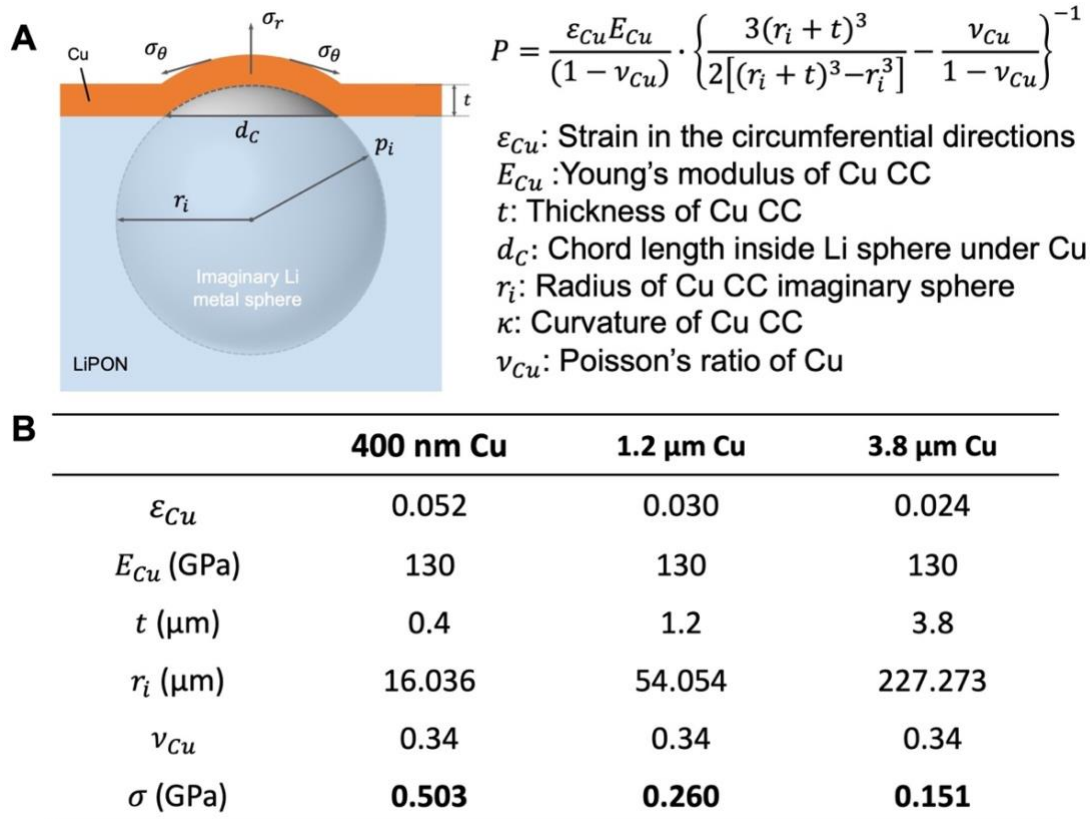
Figure 6.20 Stress analysis on Li-Cu cell with different Cu thicknesses. (A) Schematic of the model used for interfacial stress estimation and corresponding formula. (B) parameters and calculated stresses at Li/Cu interface with different Cu thicknesses.

Such high interfacial stress present at Cu/Li interface confines Li metal morphology to achieve fully dense feature. Based on aforementioned stress formula, interfacial stress is inversely proportional to the Li deposit diameter and proportional to Cu strain, suggesting that Li metal deposit tends to have plenary growth so that overall stress can be released, resulting in more uniform coverage of Li metal on LiPON and less chance of dendrite formation. As such, we propose several criteria that need to be considered while building ideal configuration for Li metal plating in solid state system. As shown in Figure 6.18C, intrinsic interfacial stress is essential to generate pressure during Li metal plating without the aid of external pressure; proper current collector thickness is needed to confine Li metal morphology while maintaining its own structural integrity; uniform Li metal nucleation and rapid merging of different Li nucleates helps reduce the

121

plastic deformation of current collector to prolong the cyclability. Consequently, one solution to achieve uniform Li metal deposition is adding seeding layer at Cu/SSE interface, as to facilitate uniform Li metal nucleation and subsequent uniform and dense Li metal growth. In this case, Au seeding layer was selected to demonstrate the hypothesis, since metal elements that alloy with Li metal tend to be lithiophillic and can regulate nucleation behavior.[195] Prior to depositing Cu on FS-LiPON, a 3-nm-thick Au layer was first evaporated on FS-LiPON. Surface SEM image and EDS results in Figure 6.21 validates the Au film formed on FS-LiPON before Li-Cu cell fabrication. After electrochemical plating with zero external pressure (Figure 6.22A),
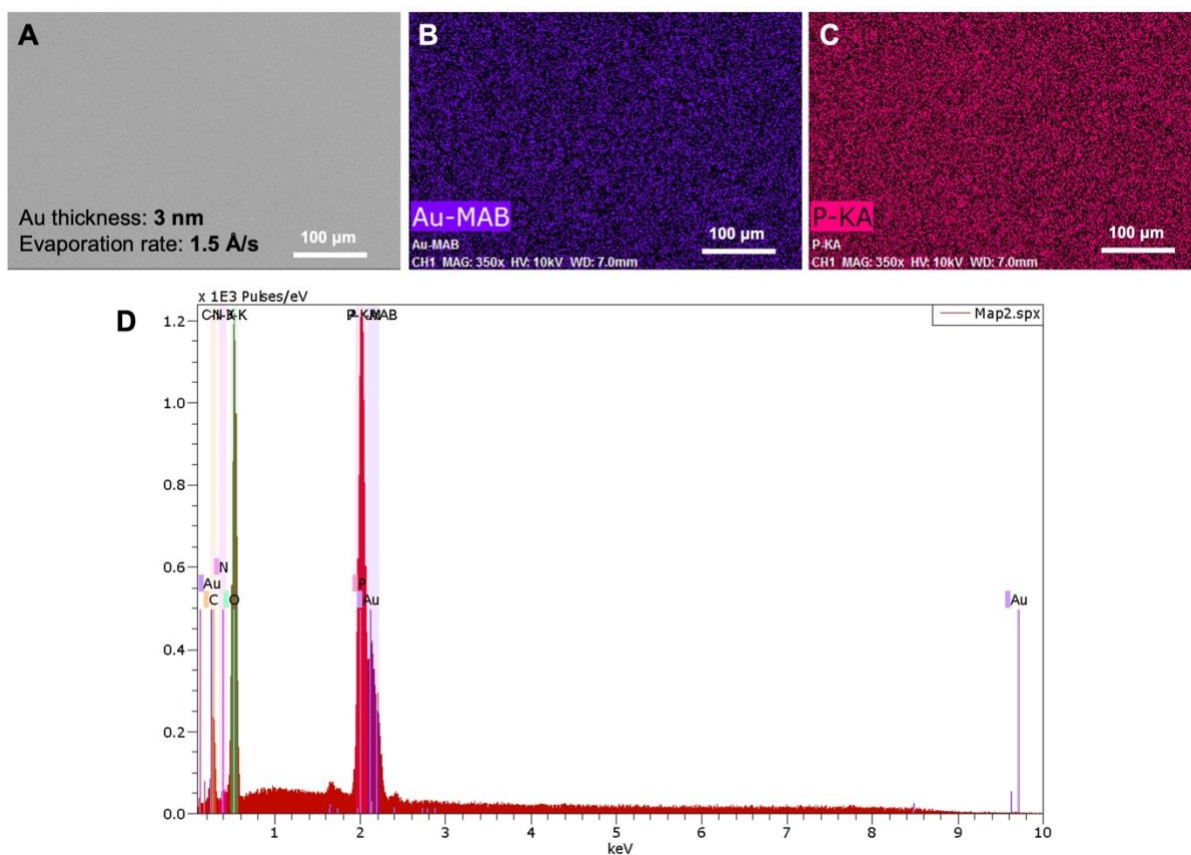
Figure 6.21 (A) Top-view SEM image of Au seeding layer on FS-LiPON. Au film thickness is 3 nm. EDS mapping results of Au signal (B) and P signal (C) in the same region, demonstrating the uniform evaporation of Au on FS-LIPON. (D) EDS spectrum collected from the region shown in (A).

Cu surface remains relatively smooth as shown in Figure 6.22B, suggesting a uniform Li metal deposition beneath. Figure 6.18D shows the cross-section image of the Li-Cu cell with Au seeding layer after plating. Measured thickness of Li metal deposit is ~1.3 μm, close to the thickness calculated from areal capacity (Figure 6.22A). Li metal deposit appears not only full dense, but also uniform across the whole region. Small inclusions found in plated Li metal layer are likely the Li-Au alloy based on cross-section EDS in Figure 6.23. Based on above results, with the aid of interfacial stress and seeding layer, uniform and fully dense Li metal deposition can be realized in solid-state system under zero external pressure.
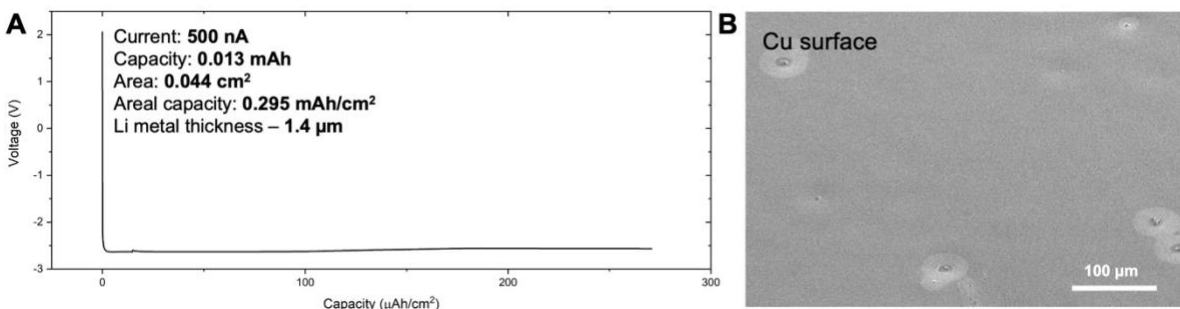
Figure 6.22 (A) Voltage curve of Li metal plating in Li-Cu cell with Au seeding layer. (B) Surface morphology of plated Li-Cu cell, showing a relatively smooth Cu surface and indicating uniform Li metal deposition.
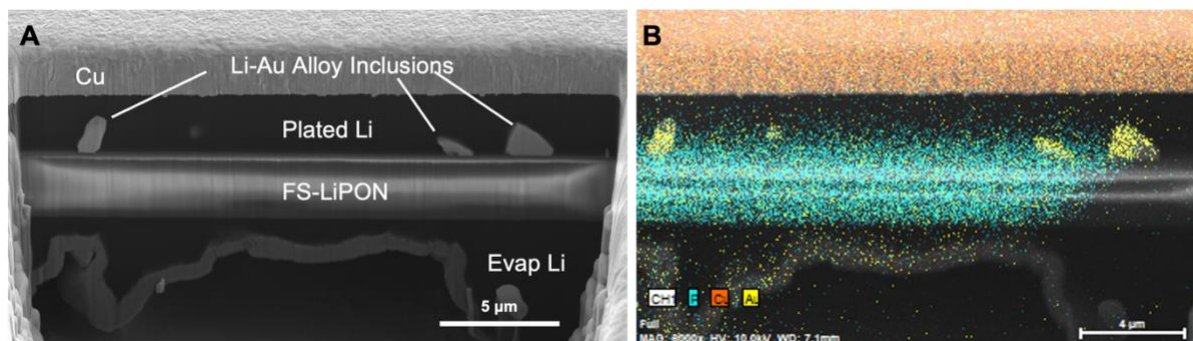
Figure 6.23 (A) Cross-section image of plated Li-Cu cell with Au seeding layer. Plated Li metal in this cell is ~3 μm in thickness. Inclusions within plated Li layer can be seen. (B) EDS mapping at the region shown in (A), suggesting the inclusions are Au-containing species.

Additionally, a further effort to demonstrate Li stripping in the Li-Cu FS-LiPON cell were summarized in Figure 6.24 and Figure 6.25. Although the Li-Cu FS-LiPON cell without external pressure ended up with non-uniform stripping that led to the formation of gaps between Cu and FS-LiPON and generates inactive lithium (Figure 6.24), an external pressure of ~87.5 kPa helped largely improve the Coulombic efficiency to 82.7% (Figure 6.25). It is important to stress that external pressure appears to be essential for the stripping process, while uniformly dense Li metal plating could be realized via interfacial stress and seeding layer solely. Another note is that the external pressure used in this set of experiments was nearly two orders of magnitude lower than the pressure commonly used in bulk solid-state Li metal batteries.[47,126] With such a low external pressure, a relatively good Coulombic efficiency for Li metal plating and stripping was achieved. An intriguing observation was that the gap/void caused by stripping was formed between Cu and Li metal instead of being present between Li metal and FS-LiPON (Figure 6.25C), in contrast to the scenarios reported in bulk solid-state systems using argyrodite- or garnet-type SSEs.[196,197] Such difference is indeed related to the various current densities applied. Nevertheless, the fact that void was absent between Li metal and SSE in this case pertains to the unique characteristics of LiPON itself and Li/LiPON interface: LiPON is known for its amorphous nature, where grain boundaries are avoided. However, grain boundaries in other SSEs could be detrimental for creating current hotspot during Li plating/stripping as grain boundaries exhibit a higher electrical conductivity than bulk SSE does;[94] Meanwhile, the interface formed between Li and LiPON guarantees a facile lithium transport with excellent electrochemical stability that prevents current hotspot caused by continuous interfacial reactions. These features might have contributed to the absence of void formation between Li metal and LiPON and could shed light on the interface engineering in the bulk solid-state batteries.
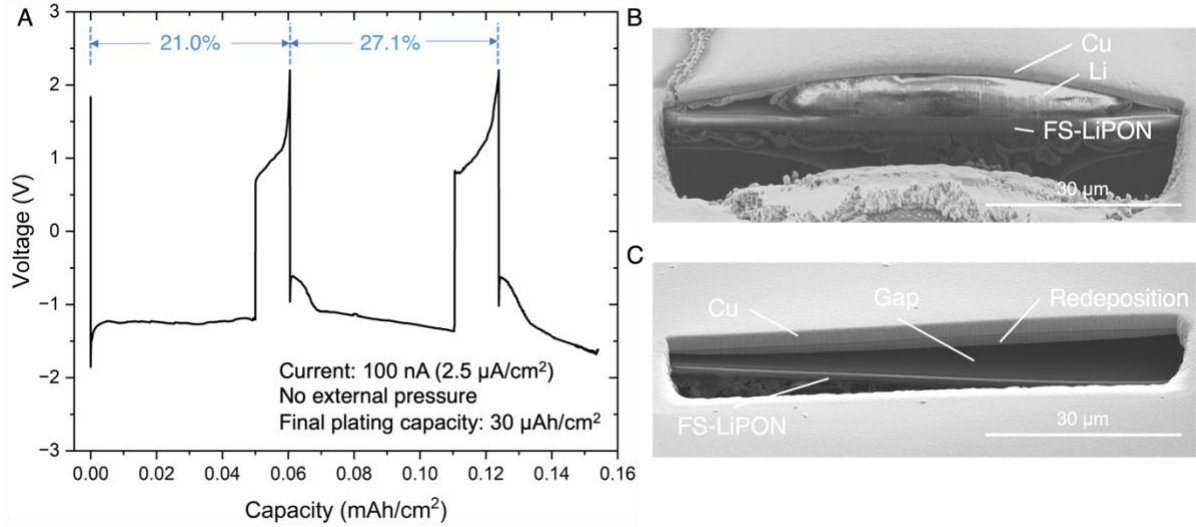
Figure 6.24 (A) Voltage curve of Li-Cu FS-LiPON cell cycled with a current of 100 nA under no external pressure. (B) Cross-section image of Li-Cu cell with Au seeding layer after cycling. Li metal layer appears charging under SEM. (C) Cross-section image of Li-Cu cell with Au seeding layer after cycling with a gap formed between Cu and FS-LiPON layers.
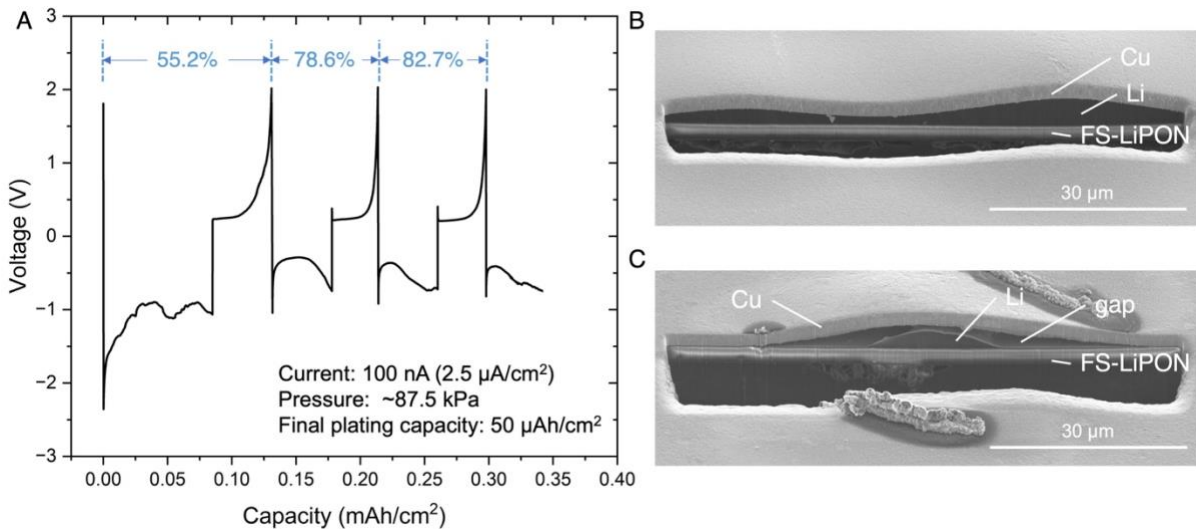
Figure 6.25 (A) Voltage curve of Li-Cu FS-LiPON cell cycled with a current of 100 nA under an external pressure of ~87.5 kPa. (B)(C) Cross-section images of Li-Cu cell with Au seeding layer after cycling.

125

6.4 Conclusions and Outlook

This work presents a different methodology to produce a thin film SSE in a freestanding form that manifests transparency and remarkable flexibility. Basic characterizations validated the chemical compatibility of FS-LiPON against materials used during synthesis procedure. The absence of substrate for FS-LiPON largely leverages fundamental studies on LiPON material. Solid-state NMR illustrates fresh quantitative insights of Li/LiPON interface supplementing the previous findings by electron microscopy. DSC captures the glass transition behavior of LiPON around 207 °C with a high signal-to-noise ratio. Nanoindentation and flexibility test yield a Young's modulus of ~33 GPa of LiPON and show the flexible nature of LiPON film, respectively, calling for further mechanical tests to comprehensively explore LiPON's native mechanical properties. A further demonstration of an electrochemical cell employing FS-LiPON shows its ability to conduct lithium ions. Stress analysis at Li/Cu interface suggests the presence of a high compressive stress in the order of 10^{-1} GPa, which facilitates Li metal yielding and is the key for a dendrite-free, dense Li metal morphology. With the further aid of Au seeding layer, a fully dense and uniform Li metal deposition was realized under zero external pressure. The ideal conditions proposed for uniform Li metal deposition that combine interfacial stress and seeding layer provide new perspectives for interface engineering. The effort on Li metal stripping implies the essence of the amorphous nature of SSE and interfacial stability on preventing void formation within Li metal during the stripping process. With the freestanding form of LiPON thin films, opportunities have been opened up for a wider application of LiPON material. When coupled with casted cathodes, FS-LiPON can potentially be utilized as the SSE and enable Li metal anode with minimal external pressure.

Chapter 6, in full, is a reprint of the material, as it appears in a work that is currently under rebuttal with *Nature Nanotechnology*: **D. Cheng**, T. Wynn, B. Lu, B. Han, R. Shimizu, B. Sreenarayanan, M. Marple, Y. Yang, H. Nguyen, W. Li, G. Zhu, M. Zhang and Y. S. Meng, "Freestanding LiPON: from Fundamental Study to Uniformly Dense Li Metal Deposition Under Zero External Pressure", 2023. The dissertation author was the primary investigator and first author of this paper.

Chapter 7. Conclusion and Future Perspectives

7.1 Summary of the dissertation

Over decades of battery research on developing new materials/chemistries and advancing characterization methodologies, numerous fresh understandings on active materials and interfaces have been documented in literature. Nevertheless, Li metal anode remains as the "holy grail" for researchers in the fields of both liquid-electrolyte battery and its solid-state analogues. Although some liquid-electrolyte battery using fluorinated-ether-based electrolyte has enable a Coulombic efficiency as high as 99.9%,[8,75] the reactivity of Li metal and highly flammable organics in the electrolyte cast big question marks on its practical use in the electric vehicles. On the other hand, the intrinsically safer alternative that utilize SSEs has demonstrate some success on addressing the Li dendrite issue and interface instability,[47] however, the high isostatic pressure required for stable cycling introduced extra hurdles for battery scaling up. Future efforts on ASSB call for new strategies to enable uniform Li metal plating/stripping at lower stacking pressure and to stabilize Li metal-associated interface with more effective way.

Owing to the well-defined platform provided by LiPON-based thin film batteries, a deeper understanding of LiPON's interface stability against highly reductive Li metal and high oxidative LNMO cathode has been unraveled with the aid of advanced electron microscopy. The efforts on producing freestanding LiPON film offered valuable quantitative insights on interface formation between Li metal and LiPON by solid-state NMR, which serves as supportive evidence to the electron microscopy observation. Moreover, freestanding LiPON was demonstrated to enable Li metal plating in a uniform and fully dense manner without external pressure. Such observations provide new insight on interface engineering, but also bring new hints on reducing the external pressure on Li metal ASSB that is required for stable cycling.

Chapter 4 focuses on one of the most famous yet least understood interfaces, Li/LiPON interface, for characterization. By coupling cryo-FIB/SEM and cryo-TEM, such an air- and beam-sensitive interface was illustrated to form a 76-nm-thick interphase, composed of Li_2O, Li_3N and Li_3PO_4 decomposition products that are embedded in an amorphous matrix. The mixture of these ionically conductive but electrically insulating species, and the elemental gradients at the interphase are proposed to effectively protect LiPON from being continuously reduced by Li metal anode. The findings on LiPON's electrochemical stability against Li metal stress on the essence of suitable interface component (i.e., Li_3N) and chemical gradient at the interface, pivoting interface engineering towards new directions.

Chapter 5 sheds light on the new understanding of LNMO/LiPON interface by combining advanced characterization tools and computational methods. An overlithiation is observed at the surface of LNMO at the interface that leads excess 1st charge capacity and Mn reduction. The deposition process of LiPON on LNMO is proposed to be the cause of overlithiation, which is potentially related to LiPON's resilience against the high oxidative potential of LNMO. The intact interface contact between LNMO and LiPON after over 500 cycles suggests the importance of atomic contact to interface stability, and offers hints to remove conductive agents at the interface that could serve as the hotspots for interfacial decomposition.

Chapter 6 demonstrates a new methodology to synthesis LiPON film in a freestanding form. The removal of rigid, thick substrate provides numerous merits for both fundamental studies and applications. Ss-NMR was able to probe the Li/LiPON interface with quantitative insights on the interfacial components formation, which are regarded as the supportive evidence to the spatial distribution observed in the Li/LiPON work by cryo-TEM in Chapter 4. DSC measurement yields a well-defined glass transition temperature of LiPON, while nanoindentation uncovers a Young's

modulus of ~33 GPa of LiPON that might be related to a residual stress release process in the freestanding film. FS-LiPON film was further illustrated to enable a uniformly dense Li metal plating with zero external pressure, aided by combining interfacial stress and seeding layer, which provides valuable insights on interface engineering in bulk ASSB.

In summary, this dissertation demonstrates a thorough study of LiPON and associated solid-solid interfaces in a Li/LiPON/LNMO thin film battery system with the help of advanced electron microscopy. Despite the deepened understanding of these subjects from above studies, the ex-situ characterizations still lack the ability to capture metastable phases and kinetics during reactions. Moreover, the local information collected by electron microscopy can be misleading when the sampling region is small. In the next section, we will discuss some potential directions for follow-up work as well as some limitations from instrumental perspective that could be addressed in the future.

7.2 Future Perspectives

7.2.1 In situ Li metal plating and stripping study by leveraging FS-LiPON film

A uniformly dense Li metal plating has been observed in a Li-Cu FS-LiPON cell when zero external pressure is present. It was proposed that the uniform Li nucleation due to the use of seeding layer is the key to uniform Li metal growth afterwards. By leveraging the in-situ FIB/SEM capability that was developed years ago (Figure 7.1), one can verify the nucleation uniformity by observing surface morphology by SEM when biasing the Li-Cu FS-LiPON cell. Cross-section SEM image at early plating stage could offer direct evidence regarding Li metal nucleation and how seeding layer aids uniform nucleation.

As introduced in Chapter 6, a Li-Cu FS-LiPON cell could achieve a Coulombic efficiency of 82.6% when stripped under external pressure. The intriguing finding in this experiment is that

voids are formed between Cu and residual Li metal instead of being between Li metal and LiPON. Such observation indicates the unique amorphous nature of LiPON and a good Li/LiPON interface might be key for preventing void formation during stripping in ASSB.
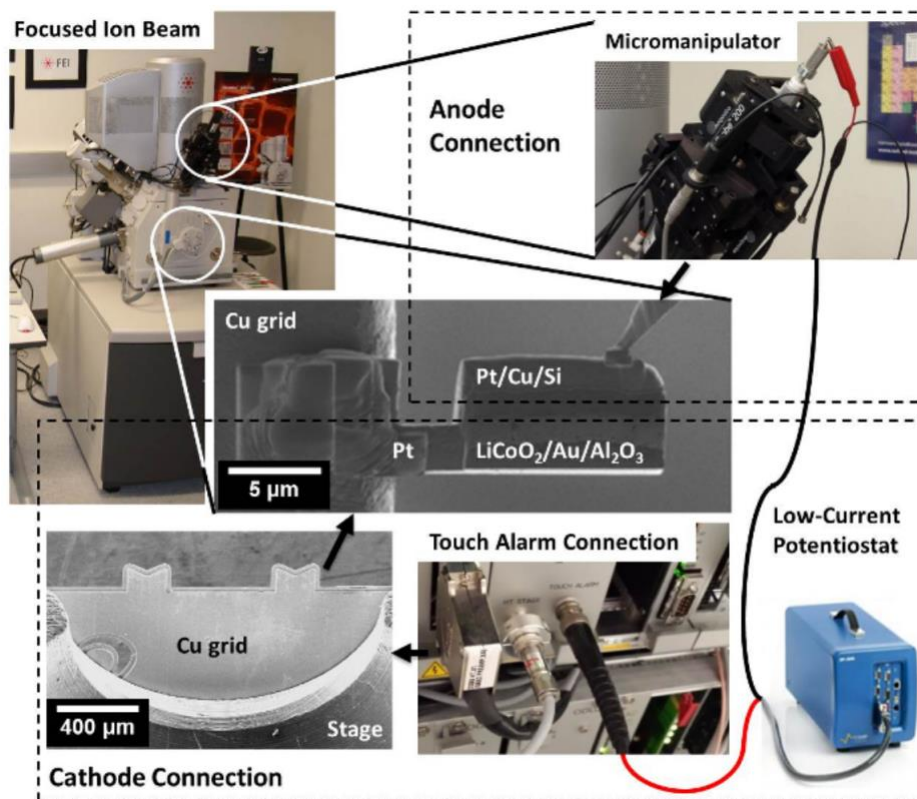
Figure 7.1 Electrical connection schematic to enable in situ biasing within a FIB/SEM

Therefore, it is necessary to conduct Li metal stripping following the in-situ plating in FIB/SEM. Exposing the cross section of the Li-Cu FS-LiPON cell during stripping can give unequivocal evidence of Li metal behavior upon stripping with/without external pressure. Results could generate meaningful dataset to explain Li metal stripping process in ASSB. However, note that due to the redeposition effect during FIB milling, Li-Cu FS-LiPON cell can be easily shorted at the cross-section region. Extra optimization on FIB milling parameters might be needed to perform above experiments.

7.2.2 A regulated cryo-EM workflow specifically for battery research

Although the application of cryo-EM in batteries seems promising, herein we list out several concerns pertaining to the regulation of cryo-EM study that calls for attention: 1) the limitation of cryogenic protection; 2) cryogenic sample transfer protocols; 3) consistent data collection and reliable data analysis; 4) the dearth of knowledge for phase change of complex materials at low temperature.
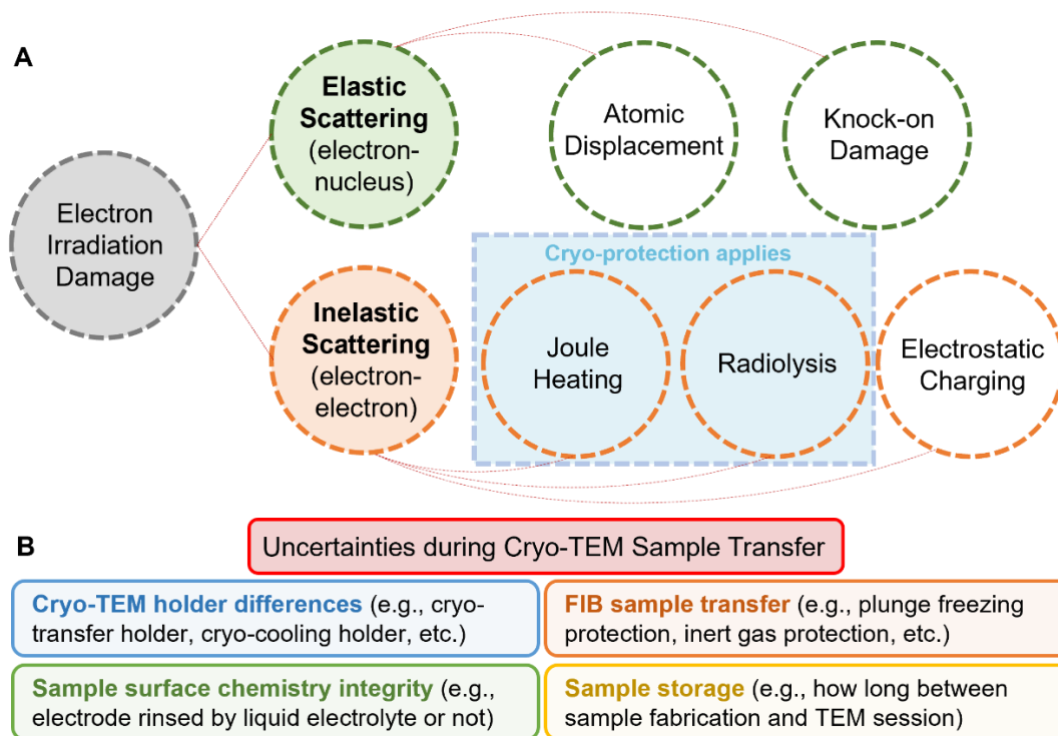
Figure 7.2 (A) Schematic of electron irradiation damage mechanisms, where only beam damage from Joule heating and Radiolysis can be mitigated by cryogenic protection. (B) Uncertainties during cryo-TEM sample transfer that can lead to inconsistent data collection and interpretation.

Cryogenic protection is applied on material to avoid damage on its structure or chemistry from electron beam irradiation. The damage mechanisms fall into two main categories – elastic scattering (electron-nucleus interaction) and inelastic scattering (electron-electron interaction)[198] (Figure 7.2A). When elastic scattering damage occurs, accelerated electrons with high kinetic energy reaching the specimen surface lead to the displacement of atoms within the specimen.

132

Atoms are knocked off when the momentum transferred from electrons is high enough, resulting in irradiation damage. Alternatively, inelastic scattering damage occurs due to the interaction between incoming electrons and specimen electrons, which may cause overly joule heating, radiolysis, and electrostatic charging[199]. Note that of all the damage mechanisms, only joule heating and radiolysis can be mitigated by cryogenic protection, stressing the importance of knowing the damage mechanisms of target material before choosing the right way for protection from irradiation.

The complexity of cryo-EM characterization determines that the discrepancies can be easily generated during the many steps of operation or generated as a result of diverse sample handling protocols. Such uncertainties lie in the whole sample transfer procedure, where cryo-TEM holder choices, cryo-FIB sample transfer process, metal anode sample washing process and TEM sample storage before actual TEM sessions all need to be regulated with standardized protocols or well documented in the publication (Figure 7.2B). In specific, TEM holder choices between cryo-transfer holder and cryo-cooling holder could lead to data discrepancies due to the various amount of air exposure during the transfer[200]; cryo-FIB sample transferred through plunge freezing protection suffers from icing problem; metal anode TEM samples should not be washed by liquid electrolyte to maintain the surface chemistry integrity; the storage time for the TEM sample before actual measurement is also likely to cause result discrepancies even in the atmosphere-controlled glovebox.

7.2.3 Automation of EM data analysis

Another solution to ensure consistent dataset is the implantation of AI technology into the EM examination process, during both data collection and data analysis (Figure 7.3). Automated

TEM image acquisition will benefit on large-batch data acquisition and reduce the human errors caused by potential beam alignment issues, incorrect target material locating or inconsistent image acquisition parameters[201]. TEM images must be coupled with techniques such as EELS to confirm the characteristic chemical signature of target species[202]. Once dataset is collected, the analytic process requires new approaches that are capable of handling datasets of gigantic size with high efficiency and accuracy, with AI being a potential solution. Recently there has been a renaissance in AI-assisted data post-processing, owing to the success of deep learning (DL)[203–205]. However, certain limitations present in these studies due to the use of datasets from one specific sample[204] and the lack of a universal model for all the high-resolution images from one dataset. Thus, it is essential to develop coding tools that can be equipped with DL to process multiple TEM images and utilize suitable segmentation method to extract features such as the spots in Fast Fourier Transform (FFT) patterns so that crystallographic information about the specimens can be processed and summarized in an accurate way. The subsequent outputs eventually yield conclusions that can be based on statistics. Meanwhile, the emergence of automated analysis methods in materials science calls for adequate computational capability, which has given rise to open-source software and web-based hosting services[206,207]. Nevertheless, such analytical tools require an appropriate computational environment with necessary storage for operation. To avoid constantly upgrading and setting up the limited local computational environment (i.e., personal computers), cloud computing helps to achieve high-throughput data analysis using Software-as-a-Service (SaaS) model, though data privacy and security remain an issue[208,209]. Hence, the development of web platforms that can provide material simulation and analysis, and supercomputer facility that allows real-time access for such TEM data processing will be imperative for the success of automated big data analysis.
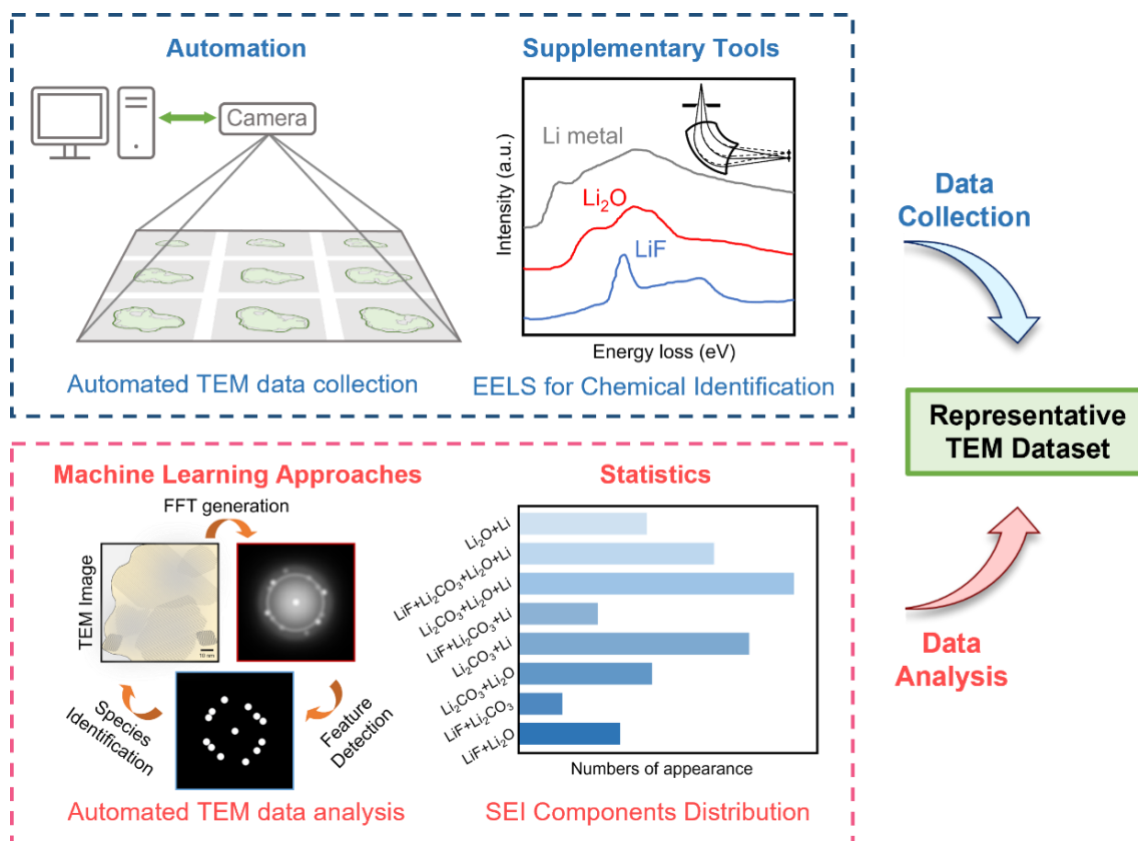
Figure 7.3 Proposed workflow of AI-assisted TEM data collection and analysis.

The deployment of cryo-EM into the battery field in the past four years has motivated many more efforts in studying the beam-sensitive interfaces and other crucial components lying at nanoscale, and provided invaluable insights for advancing battery design. The research focus of Li metal anode has shifted from suppressing dendrite growth to eliminating inactive lithium accumulation. Newly gained knowledge enabled morphology-controlled uniform Li metal deposition that can be tuned by nucleation process, interface engineering and external uniaxial pressure. Cryo-EM applications in other branches of battery research have shed light on the correlation between beam-sensitive interfaces/interphases and material performance. Looking forward, numerous fresh understandings can be obtained through more advanced capabilities of cryo-EM, such as 3D-tomography of SEI or operando biasing within TEM, which potentially

generate a more comprehensive picture of SEI formation/distribution and dynamic changes within battery during operation. Coupled with AI-assisted data collection and processing, cryo-EM will continue bringing advancement of battery systems at a far faster rate.

In retrospect, the early development of cathode materials for battery and cryogenic functionality for electron microscopy occurred in the same era, but barely any interaction occurred for over four decades. Now electron microscopy finally made a detour back with cryogenic protection for advancing battery material characterizations. Unprecedented insights obtained from cryogenic techniques benefit not limited to the battery field, but to the whole material science community, stressing the importance of fully understanding material properties and behaviors over a vast temperature range. In this regard, exploring the phase diagram of complex materials at low temperature remains essential for better data interpretation from cryogenic techniques, which can yield new insights to the material study. With the advancement of high-end detectors and imaging techniques such as 4D-STEM, cryo-EM also gives chance to a more comprehensive picture of exotic physical properties of quantum materials and neuromorphic electronic materials when the motion of matters is slowed down at low temperature and can be then captured within a reasonable temporal scale.

Chapter 7, in part, is a reprint of the material, as it appears in: **D. Cheng**, B. Lu, G. Raghavendran, M. Zhang and Y. S. Meng, "Leveraging Cryogenic Electron Microscopy for Advancing Battery Design", *Matter*, 2022, 5, 26–42. The dissertation author was the primary investigator and first author of this paper.

References

1. Singh, P., Singh, S., Kumar, G. & Baweja, P. *Energy: Crisis, Challenges and Solutions*. (John Wiley & Sons, Ltd, 2022).
2. U.S. Energy Information Administration. *Annual Energy Outlook 2022*. https://www.eia.gov/ (2022).
3. Ela, E., Diakov, V., Ibanez, E. & Heaney, M. *Impacts of Variability and Uncertainty in Solar Photovoltaic Generation at Multiple Timescales*. *National Renewable Energy Laboratory* http://www.nrel.gov/docs/fy13osti/58274.pdf (2013).
4. Ritchie, H., Roser, M. & Rosado, P. CO_2 and Greenhouse Gas Emissions. *OurWorldInData.org* https://ourworldindata.org/co2-and-greenhouse-gas-emissions (2020).
5. Winter, M., Barnett, B. & Xu, K. Before Li Ion Batteries. *Chem. Rev.* **118**, 11433–11456 (2018).
6. Xu, K. Nonaqueous liquid electrolytes for lithium-based rechargeable batteries. *Chem. Rev.* **104**, 4303–4417 (2004).
7. Xu, K. Electrolytes and interphases in Li-ion batteries and beyond. *Chem. Rev.* **114**, 11503–11618 (2014).
8. Meng, Y. S., Srinivasan, V. & Xu, K. Designing better electrolytes. *Science (80-.).* **378**, (2022).
9. Frith, J. T., Lacey, M. J. & Ulissi, U. A non-academic perspective on the future of lithium-based batteries. *Nat. Commun.* **14**, (2023).
10. Whittingham, M. S., Fanwood & N.J. Chalcogenide battery. *Exxon Research and Engineering Company* 1–5 (1977).
11. Goodenough, J. B., Mizushima, K. & Wiseman, P. J. Electrochemical cell and method of making ion conductors for said cell. *UNITED KINGDOM ATOMIC ENERGY AUTHORITY* vol. 13 258–283 (1976).
12. Thackeray, M. ., Johnson, P. J., de Picciotto, L. A., Bruce, P. G. & Goodenough, J. B. Electrochemical extraction of lithium from LiMn2O4. *Mater. Res. Bull.* **19**, 179–187 (1984).
13. Delmas, C. & Saadoune, I. Electrochemical and physical properties of the LixNi1−yCoyO2 phases. *Solid State Ionics* **56**, 370–375 (1992).
14. Padhi, A. K., Nanjundaswamy, K. S. & Goodenough, J. B. Phospho-olivines as Positive-Electrode Materials for Rechargeable Lithium Batteries. *J. Electrochem. Soc.* **144**, 1188 (1997).
15. Gao, Y., Myrtle, K., Zhang, M., Reimers, J. N. & Dahn, J. R. Valence band and its effects on the voltage profiles /Li electrochemical cells. *Phys. Rev. B* **54**, 16670–16675 (1996).
16. Li, J. Y., Xu, Q., Li, G., Yin, Y. X., Wan, L. J. & Guo, Y. G. Research progress regarding Si-based anode materials towards practical application in high energy density Li-ion batteries. *Mater. Chem. Front.* **1**, 1691–1708 (2017).
17. Niu, C., Liu, D., Lochala, J. A., Anderson, C. S., Cao, X., Gross, M. E., Xu, W., Zhang, J.-G., Whittingham, M. S., Xiao, J. & Liu, J. Balancing interfacial reactions to achieve long cycle life in high-energy lithium metal batteries. *Nat. Energy* (2021) doi:10.1038/s41560-021-00852-3.
18. Xu, W., Wang, J., Ding, F., Chen, X., Nasybulin, E., Zhang, Y. & Zhang, J.-G. Lithium metal anodes for rechargeable batteries. *Energy Environ. Sci.* **7**, 513–537 (2014).

19.   Fang, C., Li, J., Zhang, M., Zhang, Y., Yang, F., Lee, J. Z., Lee, M.-H., Alvarado, J., Schroeder, M. A., Yang, Y., Lu, B., Williams, N., Ceja, M., Yang, L., Cai, M., Gu, J., Xu, K., Wang, X. & Meng, Y. S. Quantifying inactive lithium in lithium metal batteries. *Nature* **572**, 511–515 (2019).

20.   Lin, D., Liu, Y. & Cui, Y. Reviving the lithium metal anode for high-energy batteries. *Nat. Nanotechnol.* **12**, 194–206 (2017).

21.   Gao, Z., Sun, H., Fu, L., Ye, F., Zhang, Y., Luo, W. & Huang, Y. Promises, Challenges, and Recent Progress of Inorganic Solid-State Electrolytes for All-Solid-State Lithium Batteries. *Adv. Mater.* **30**, 1–27 (2018).

22.   Chen, R., Qu, W., Guo, X., Li, L. & Wu, F. The pursuit of solid-state electrolytes for lithium batteries: From comprehensive insight to emerging horizons. *Mater. Horizons* **3**, 487–516 (2016).

23.   Hayashi, A., Kama, S., Mizuno, F., Tadanaga, K., Minami, T. & Tatsumisago, M. Characterization of Li2S-P2S5 glass-ceramics as a solid electrolyte for lithium secondary batteries. *Solid State Ionics* **175**, 683–686 (2004).

24.   Zuo, X., Liu, X. M., Cai, F., Yang, H., Shen, X. D. & Liu, G. A novel all-solid electrolyte based on a co-polymer of poly-(methoxy/ hexadecal-poly(ethylene glycol) methacrylate) for lithium-ion cell. *J. Mater. Chem.* **22**, 22265–22271 (2012).

25.   Zhu, Y., He, X. & Mo, Y. Origin of Outstanding Stability in the Lithium Solid Electrolyte Materials: Insights from Thermodynamic Analyses Based on First-Principles Calculations. *ACS Appl. Mater. Interfaces* **7**, 23685–23693 (2015).

26.   Richards, W. D., Miara, L. J., Wang, Y., Kim, J. C. & Ceder, G. Interface Stability in Solid-State Batteries. *Chem. Mater.* **28**, 266–273 (2016).

27.   Tippens, J., Miers, J. C., Afshar, A., Lewis, J. A., Cortes, F. J. Q., Qiao, H., Marchese, T. S., Di Leo, C. V., Saldana, C. & McDowell, M. T. Visualizing Chemomechanical Degradation of a Solid-State Battery Electrolyte. *ACS Energy Lett.* **4**, 1475–1483 (2019).

28.   Ma, C., Cheng, Y., Yin, K., Luo, J., Sharafi, A., Sakamoto, J., Li, J., More, K. L., Dudney, N. J. & Chi, M. Interfacial Stability of Li Metal-Solid Electrolyte Elucidated via in Situ Electron Microscopy. *Nano Lett.* **16**, 7030–7036 (2016).

29.   Cheng, E. J., Sharafi, A. & Sakamoto, J. Intergranular Li metal propagation through polycrystalline Li6.25Al0.25La3Zr2O12 ceramic electrolyte. *Electrochim. Acta* **223**, 85–91 (2017).

30.   Wood, K. N., Steirer, K. X., Hafner, S. E., Ban, C., Santhanagopalan, S., Lee, S. H. & Teeter, G. Operando X-ray photoelectron spectroscopy of solid electrolyte interphase formation and evolution in Li2S-P2S5 solid-state electrolytes. *Nat. Commun.* **9**, 1–10 (2018).

31.   Schwöbel, A., Hausbrand, R. & Jaegermann, W. Interface reactions between LiPON and lithium studied by in-situ X-ray photoemission. *Solid State Ionics* **273**, 51–54 (2015).

32.   Weiss, M., Seidlhofer, B. K., Geiß, M., Geis, C., Busche, M. R., Becker, M., Vargas-Barbosa, N. M., Silvi, L., Zeier, W. G., Schröder, D. & Janek, J. Unraveling the Formation Mechanism of Solid-Liquid Electrolyte Interphases on LiPON Thin Films. *ACS Appl. Mater. Interfaces* **11**, 9539–9547 (2019).

33.   Sicolo, S., Fingerle, M., Hausbrand, R. & Albe, K. Interfacial instability of amorphous LiPON against lithium: A combined Density Functional Theory and spectroscopic study. *J. Power Sources* **354**, 124–133 (2017).

34.   Janek, J. & Zeier, W. G. Challenges in speeding up solid-state battery development. *Nat.*

Energy **8**, 230–240 (2023).

35. Tan, D. H. S., Banerjee, A., Chen, Z. & Meng, Y. S. From nanoscale interface characterization to sustainable energy storage using all-solid-state batteries. *Nat. Nanotechnol.* **15**, 1–11 (2020).

36. Banerjee, A., Wang, X., Fang, C., Wu, E. A. & Meng, Y. S. Interfaces and Interphases in All-Solid-State Batteries with Inorganic Solid Electrolytes. *Chem. Rev.* **120**, 6878–6933 (2020).

37. J.B. Bates, N.J. Dudney, G.R. Gruzalski, R.A. Zuhr, A. Choudhury, C. F. L. Electrical properties of amorphous lithium electrolyte thin films. *Solid State Ionics* **29**, 42–44 (1992).

38. Bates, J. B., Dudney, N. J., Gruzalski, G. R., Zuhr, R. A., Choudhury, A., Luck, C. F. & Robertson, J. D. Fabrication and characterization of amorphous lithium electrolyte thin films and rechargeable thin-film batteries. *J. Power Sources* **43**, 103–110 (1993).

39. Neudecker, B. J., Dudney, N. J. & Bates, J. B. "Lithium-Free" Thin-Film Battery with In Situ Plated Li Anode. *J. Electrochem. Soc.* **147**, 517 (2000).

40. Li, J., Ma, C., Chi, M., Liang, C. & Dudney, N. J. Solid electrolyte: The key for high-voltage lithium batteries. *Adv. Energy Mater.* **5**, 1–6 (2015).

41. Wang, Z., Santhanagopalan, D., Zhang, W., Wang, F., Xin, H. L., He, K., Li, J., Dudney, N. & Meng, Y. S. In situ STEM-EELS observation of nanoscale interfacial phenomena in all-solid-state batteries. *Nano Lett.* **16**, 3760–3767 (2016).

42. Cheng, D., Wynn, T. A., Wang, X., Wang, S., Zhang, M., Shimizu, R., Bai, S., Nguyen, H., Fang, C., Kim, M., Li, W., Lu, B., Kim, S. J. & Meng, Y. S. Unveiling the Stable Nature of the Solid Electrolyte Interphase between Lithium Metal and Lipon Via Cryogenic Electron Microscopy. *Joule* **4**, 2484–2500 (2020).

43. Park, S. I., Quan, Y. J., Kim, S. H., Kim, H., Kim, S., Chun, D. M., Lee, C. S., Taya, M., Chu, W. S. & Ahn, S. H. A review on fabrication processes for electrochromic devices. *Int. J. Precis. Eng. Manuf. - Green Technol.* **3**, 397–421 (2016).

44. Oukassi, S., Salot, R., Bazin, A., Secouard, C., Chevalier, I., Poncet, S., Poulet, S., Boissel, J. M., Geffraye, F. & Brun, J. Millimeter scale thin film batteries for integrated high energy density storage. *Tech. Dig. - Int. Electron Devices Meet. IEDM* **2019-Decem**, 618–621 (2019).

45. Wang, Z., Lee, J. Z., Xin, H. L., Han, L., Grillon, N., Guy-Bouyssou, D., Bouyssou, E., Proust, M. & Meng, Y. S. Effects of cathode electrolyte interfacial (CEI) layer on long term cycling of all-solid-state thin-film batteries. *J. Power Sources* **324**, 342–348 (2016).

46. Han, B., Xu, D., Chi, S. Sen, He, D., Zhang, Z., Du, L., Gu, M., Wang, C., Meng, H., Xu, K., Zheng, Z. & Deng, Y. 500 Wh kg−1 Class Li Metal Battery Enabled by a Self-Organized Core–Shell Composite Anode. *Adv. Mater.* **32**, 1–11 (2020).

47. Lee, Y. G., Fujiki, S., Jung, C., Suzuki, N., Yashiro, N., Omoda, R., Ko, D. S., Shiratsuchi, T., Sugimoto, T., Ryu, S., Ku, J. H., Watanabe, T., Park, Y., Aihara, Y., Im, D. & Han, I. T. High-energy long-cycling all-solid-state lithium metal batteries enabled by silver–carbon composite anodes. *Nat. Energy* **5**, 299–308 (2020).

48. Dudney, N. J. Solid-state thin-film rechargeable batteries. *Mater. Sci. Eng. B Solid-State Mater. Adv. Technol.* **116**, 245–249 (2005).

49. Put, B., Mees, M. J., Hornsveld, N., Hollevoet, S., Sepúlveda, A., Vereecken, P. M., Kessels, W. M. M. & Creatore, M. Plasma-Assisted ALD of LiPO(N) for Solid State Batteries. *J. Electrochem. Soc.* **166**, A1239–A1242 (2019).

50. Nimisha, C. S., Rao, G. M., Munichandraiah, N., Natarajan, G. & Cameron, D. C. Chemical and microstructural modifications in LiPON thin films exposed to atmospheric humidity. *Solid State Ionics* **185**, 47–51 (2011).
51. Zhao, S., Fu, Z. & Qin, Q. A solid-state electrolyte lithium phosphorus oxynitride film prepared by pulsed laser deposition. *Thin Solid Films* **415**, 108–113 (2002).
52. Lacivita, V., Westover, A. S., Kercher, A., Phillip, N. D., Yang, G., Veith, G., Ceder, G. & Dudney, N. J. Resolving the Amorphous Structure of Lithium Phosphorus Oxynitride (Lipon). *J. Am. Chem. Soc.* **140**, 11029–11038 (2018).
53. Marple, M. A. T., Wynn, T. A., Cheng, D., Shimizu, R., Mason, H. E. & Meng, Y. S. Local Structure of Glassy Lithium Phosphorus Oxynitride Thin Films: A Combined Experimental and Ab Initio Approach. *Angew. Chemie - Int. Ed.* **59**, 22185–22193 (2020).
54. Zhu, Y., He, X. & Mo, Y. First principles study on electrochemical and chemical stability of solid electrolyte-electrode interfaces in all-solid-state Li-ion batteries. *J. Mater. Chem. A* **4**, 3253–3266 (2016).
55. Yu, X., Bates, J. B., Jellison, G. E. & Hart, F. X. A Stable Thin-Film Lithium Electrolyte: Lithium Phosphorus Oxynitride. *J. Electrochem. Soc.* **144**, 524 (1997).
56. Wang, X., Zhang, M., Alvarado, J., Wang, S., Sina, M., Lu, B., Bouwer, J., Xu, W., Xiao, J., Zhang, J. G., Liu, J. & Meng, Y. S. New Insights on the Structure of Electrochemically Deposited Lithium Metal and Its Solid Electrolyte Interphases via Cryogenic TEM. *Nano Lett.* **17**, 7606–7612 (2017).
57. Santhanagopalan, D., Qian, D., McGilvray, T., Wang, Z., Wang, F., Camino, F., Graetz, J., Dudney, N. & Meng, Y. S. Interface limited lithium transport in solid-state batteries. *J. Phys. Chem. Lett.* **5**, 298–303 (2014).
58. Knoll, M. & Ruska, E. Beitrag zur geometrischen Elektronenoptik. I. *Ann. Phys.* **404**, 529–640 (1927).
59. Wang, H., Jang, Y., Huang, B., Sadoway, D. R. & Chiang, Y. TEM Study of Electrochemical Cycling-Induced Damage and Disorder in LiCoO2 Cathodes for Rechargeable Lithium Batteries. *J. Electrochem. Soc.* **146**, 473–480 (1999).
60. Taylor, K. A. & Glaeser, R. M. Electron Diffraction of Frozen , Hydrated Protein Crystals. *Science (80-.).* **186**, 1036–1037 (2016).
61. Dubochet, J., Chang, J. J., Freeman, R., Lepault, J. & McDowall, A. W. Frozen aqueous suspensions. *Ultramicroscopy* **10**, 55–61 (1982).
62. Henderson, R., Baldwin, J. M., Ceska, T. A., Zemlin, F., Beckmann, E. & Downing, K. H. Model for the structure of bacteriorhodopsin based on high-resolution electron cryo-microscopy. *J. Mol. Biol.* **213**, 899–929 (1990).
63. Sigworth, F. J. A maximum-likelihood approach to single-particle image refinement. *J. Struct. Biol.* **122**, 328–339 (1998).
64. Shi, D., Nannenga, B. L., Iadanza, M. G. & Gonen, T. Three-dimensional electron crystallography of protein microcrystals. *Elife* **2**, 1–17 (2013).
65. Li, Y., Li, Y., Pei, A., Yan, K., Sun, Y., Wu, C. L., Joubert, L. M., Chin, R., Koh, A. L., Yu, Y., Perrino, J., Butz, B., Chu, S. & Cui, Y. Atomic structure of sensitive battery materials and interfaces revealed by cryo–electron microscopy. *Science (80-.).* **358**, 506–510 (2017).
66. Lee, J. Z., Wynn, T. A., Alvarado, J., Schroeder, M. A., Wang, X., Guy-Bouyssou, D., Proust, M. & Meng, Y. S. Cryogenic Focused Ion Beam Characterization of Lithium Metal Anodes. *ACS Energy Lett.* **4**, 489−493 (2019).

67. Zachman, M. J., Tu, Z., Choudhury, S., Archer, L. A. & Kourkoutis, L. F. Cryo-STEM mapping of solid–liquid interfaces and dendrites in lithium-metal batteries. *Nature* **560**, 345–349 (2018).

68. Jin, C., Liu, T., Sheng, O., Li, M., Liu, T., Yuan, Y., Nai, J., Ju, Z., Zhang, W., Liu, Y., Wang, Y., Lin, Z. & Lu, J. Rejuvenating dead lithium supply in lithium metal anodes by iodine redox. *Nat. Energy* 26–28 (2021) doi:10.1038/s41560-021-00789-7.

69. Huang, W., Wang, H., Boyle, D. T., Li, Y. & Cui, Y. Resolving Nanoscopic and Mesoscopic Heterogeneity of Fluorinated Species in Battery Solid-Electrolyte Interphases by Cryogenic Electron Microscopy. *ACS Energy Lett.* **5**, 1128–1135 (2020).

70. Huang, W., Wang, J., Braun, M. R., Zhang, Z., Li, Y., Boyle, D. T., McIntyre, P. C. & Cui, Y. Dynamic Structure and Chemistry of the Silicon Solid-Electrolyte Interphase Visualized by Cryogenic Electron Microscopy. *Matter* **1**, 1232–1245 (2019).

71. Yang, Y., Davies, D. M., Yin, Y., Borodin, O., Lee, J. Z., Fang, C., Olguin, M., Zhang, Y., Sablina, E. S., Wang, X., Rustomji, C. S. & Meng, Y. S. High-Efficiency Lithium-Metal Anode Enabled by Liquefied Gas Electrolytes. *Joule* **3**, 1986–2000 (2019).

72. Doux, J. M., Yang, Y., Tan, D. H. S., Nguyen, H., Wu, E. A., Wang, X., Banerjee, A. & Meng, Y. S. Pressure effects on sulfide electrolytes for all solid-state batteries. *J. Mater. Chem. A* **8**, 5049–5055 (2020).

73. Aurbach, D. The Surface Chemistry of Lithium Electrodes in Alkyl Carbonate Solutions. *J. Electrochem. Soc.* **141**, L1 (1994).

74. Peled, E. The Electrochemical Behavior of Alkali and Alkaline Earth Metals in Nonaqueous Battery Systems—The Solid Electrolyte Interphase Model. *J. Electrochem. Soc.* **126**, 2047 (1979).

75. Wang, C., Meng, Y. S. & Xu, K. Fluorinating Interphases. *J. Electrochem. Soc.* **166**, A5184–A5186 (2019).

76. Cao, X., Ren, X., Zou, L., Engelhard, M. H., Huang, W., Wang, H., Matthews, B. E., Lee, H., Niu, C., Arey, B. W., Cui, Y., Wang, C., Xiao, J., Liu, J., Xu, W. & Zhang, J. G. Monolithic solid–electrolyte interphases formed in fluorinated orthoformate-based electrolytes minimize Li depletion and pulverization. *Nat. Energy* **4**, 796–805 (2019).

77. Shadike, Z., Lee, H., Borodin, O., Cao, X., Fan, X., Wang, X., Lin, R., Bak, S. M., Ghose, S., Xu, K., Wang, C., Liu, J., Xiao, J., Yang, X. Q. & Hu, E. Identification of LiH and nanocrystalline LiF in the solid–electrolyte interphase of lithium metal anodes. *Nat. Nanotechnol.* **16**, 549–554 (2021).

78. Han, B., Zhang, Z., Zou, Y., Xu, K., Xu, G., Wang, H., Meng, H., Deng, Y., Li, J. & Gu, M. Poor Stability of Li2CO3 in the Solid Electrolyte Interphase of a Lithium-Metal Anode Revealed by Cryo-Electron Microscopy. *Adv. Mater.* **33**, (2021).

79. Han, B., Li, X., Bai, S., Zou, Y., Lu, B., Zhang, M., Ma, X., Chang, Z., Meng, Y. S. & Gu, M. Conformal three-dimensional interphase of Li metal anode revealed by low-dose cryoelectron microscopy. *Matter* **4**, 3741–3752 (2021).

80. Han, B., Zou, Y., Zhang, Z., Yang, X., Shi, X., Meng, H., Wang, H., Xu, K., Deng, Y. & Gu, M. Probing the Na metal solid electrolyte interphase via cryo-transmission electron microscopy. *Nat. Commun.* **12**, 1–8 (2021).

81. Wang, X., Pawar, G., Li, Y., Ren, X., Zhang, M., Lu, B., Banerjee, A., Liu, P., Dufek, E. J., Zhang, J. G., Xiao, J., Liu, J., Meng, Y. S. & Liaw, B. Glassy Li metal anode for high-performance rechargeable Li batteries. *Nat. Mater.* **19**, 1339–1345 (2020).

82. Yuan, H., Nai, J., Tian, H., Ju, Z., Zhang, W., Liu, Y., Tao, X. & Lou, X. W. An

ultrastable lithium metal anode enabled by designed metal fluoride spansules. *Sci. Adv.* **6**, 1–10 (2020).

83. Yuan, H., Nai, J., Fang, Y., Lu, G., Tao, X. & Lou, X. W. Double-Shelled C@MoS2 Structures Preloaded with Sulfur: An Additive Reservoir for Stable Lithium Metal Anodes. *Angew. Chemie - Int. Ed.* **59**, 15839–15843 (2020).

84. Fang, C., Lu, B., Pawar, G., Zhang, M., Cheng, D., Chen, S., Ceja, M., Doux, J.-M., Musrock, H., Cai, M., Liaw, B. & Meng, Y. S. Pressure-tailored lithium deposition and dissolution in lithium metal batteries. *Nat. Energy* **6**, 987–994 (2021).

85. Han, B., Zou, Y., Xu, G., Hu, S., Kang, Y., Qian, Y., Wu, J., Ma, X., Yao, J., Li, T., Zhang, Z., Meng, H., Wang, H., Deng, Y., Li, J. & Gu, M. Additive Stabilization of SEI on Graphite Observed Using Cryo-Electron Microscopy. *Energy Environ. Sci.* (2021) doi:10.1039/D1EE01678D.

86. He, Y., Jiang, L., Chen, T., Xu, Y., Jia, H., Yi, R., Xue, D., Song, M., Genc, A., Bouchet-Marquis, C., Pullan, L., Tessner, T., Yoo, J., Li, X., Zhang, J.-G., Zhang, S. & Wang, C. Progressive growth of the solid–electrolyte interphase towards the Si anode interior causes capacity fading. *Nat. Nanotechnol.* (2021) doi:10.1038/s41565-021-00947-8.

87. Alvarado, J., Schroeder, M. A., Zhang, M., Borodin, O., Gobrogge, E., Olguin, M., Ding, M. S., Gobet, M., Greenbaum, S., Meng, Y. S. & Xu, K. A carbonate-free, sulfone-based electrolyte for high-voltage Li-ion batteries. *Mater. Today* **21**, 341–353 (2018).

88. Yang, Y., Yin, Y., Davies, D. M., Zhang, M., Mayer, M., Zhang, Y., Sablina, E. S., Wang, S., Lee, J. Z., Borodin, O., Rustomji, C. S. & Meng, Y. S. Liquefied gas electrolytes for wide-temperature lithium metal batteries. *Energy Environ. Sci.* **13**, 2209–2219 (2020).

89. Zhang, Z., Yang, J., Huang, W., Wang, H., Zhou, W., Li, Y., Li, Y., Xu, J., Huang, W., Chiu, W. & Cui, Y. Cathode-Electrolyte Interphase in Lithium Batteries Revealed by Cryogenic Electron Microscopy. *Matter* **4**, 302–312 (2021).

90. Xing, X., Li, Y., Wang, X., Petrova, V., Liu, H. & Liu, P. Cathode electrolyte interface enabling stable Li–S batteries. *Energy Storage Mater.* **21**, 474–480 (2019).

91. Ma, C., Cheng, Y., Yin, K., Luo, J., Sharafi, A., Sakamoto, J., Li, J., More, K. L., Dudney, N. J. & Chi, M. Interfacial Stability of Li Metal-Solid Electrolyte Elucidated via in Situ Electron Microscopy. *Nano Lett.* **16**, 7030–7036 (2016).

92. Liu, X., Chen, Y., Hood, Z. D., Ma, C., Yu, S., Sharafi, A., Wang, H., An, K., Sakamoto, J., Siegel, D. J., Cheng, Y., Jalarvo, N. H. & Chi, M. Elucidating the mobility of H+ and Li+ ions in (Li6.25-: XHxAl0.25)La3Zr2O12 via correlative neutron and electron spectroscopy. *Energy Environ. Sci.* **12**, 945–951 (2019).

93. Cheng, M., Rangasamy, E., Liang, C., Sakamoto, J., More, K. L. & Chi, M. Excellent stability of a lithium-ion-conducting solid electrolyte upon reversible LI+/H+ exchange in aqueous solutions. *Angew. Chemie - Int. Ed.* **54**, 129–133 (2015).

94. Liu, X., Garcia-Mendez, R., Lupini, A. R., Cheng, Y., Hood, Z. D., Han, F., Sharafi, A., Idrobo, J. C., Dudney, N. J., Wang, C., Ma, C., Sakamoto, J. & Chi, M. Local electronic structure variation resulting in Li 'filament' formation within solid electrolytes. *Nat. Mater.* **20**, (2021).

95. Sheng, O., Zheng, J., Ju, Z., Jin, C., Wang, Y., Chen, M., Nai, J., Liu, T., Zhang, W., Liu, Y. & Tao, X. In Situ Construction of a LiF-Enriched Interface for Stable All-Solid-State Batteries and its Origin Revealed by Cryo-TEM. *Adv. Mater.* **32**, 1–10 (2020).

96. Aurbach, D. Review of selected electrode-solution interactions which determine the performance of Li and Li ion batteries. *J. Power Sources* **89**, 206–218 (2000).

97. Zheng, J., Zheng, H., Wang, R., Ben, L., Lu, W., Chen, L., Chen, L. & Li, H. 3D visualization of inhomogeneous multi-layered structure and Young's modulus of the solid electrolyte interphase (SEI) on silicon anodes for lithium ion batteries. *Phys. Chem. Chem. Phys.* **16**, 13229–13238 (2014).

98. Se, T. H. E., Electrolyte, M. & Batteries, T. O. L. The SEI model-application electrolyte. *Elecrrochimica Acta.* **40**, 2197–2204 (1995).

99. Wang, A., Kadam, S., Li, H., Shi, S. & Qi, Y. Review on modeling of the anode solid electrolyte interphase (SEI) for lithium-ion batteries. *npj Comput. Mater.* **4**, (2018).

100. Senevirathne, K., Day, C. S., Gross, M. D., Lachgar, A. & Holzwarth, N. A. W. A new crystalline LiPON electrolyte: Synthesis, properties, and electronic structure. *Solid State Ionics* **233**, 95–101 (2013).

101. Nanda, J., Yang, G., Hou, T., Voylov, D. N., Li, X., Ruther, R. E., Naguib, M., Persson, K., Veith, G. M. & Sokolov, A. P. Unraveling the Nanoscale Heterogeneity of Solid Electrolyte Interphase Using Tip-Enhanced Raman Spectroscopy. *Joule* **3**, 2001–2019 (2019).

102. Singh, C. N., Butler, K. T., MacDonald, A. H., Piper, L. F. J. & Lee, W.-C. Dynamic disorder induced memristance in amorphous solids. *arXiv:1908.08070* (2019).

103. Li, Y., Li, Y., Pei, A., Yan, K., Sun, Y., Wu, C. L., Joubert, L. M., Chin, R., Koh, A. L., Yu, Y., Perrino, J., Butz, B., Chu, S. & Cui, Y. Atomic structure of sensitive battery materials and interfaces revealed by cryo–electron microscopy. *Science (80-.).* **358**, 506–510 (2017).

104. Li, Y., Huang, W., Li, Y., Pei, A., Boyle, D. T. & Cui, Y. Correlating Structure and Function of Battery Interphases at Atomic Resolution Using Cryoelectron Microscopy. *Joule* **2**, 2167–2177 (2018).

105. Santos-Ortiz, R., Rojhirunsakool, T., Jha, J. K., Al Khateeb, S., Banerjee, R., Jones, K. S. & Shepherd, N. D. Analysis of the structural evolution of the SEI layer in FeF2 thin-film lithium-ion batteries upon cycling using HRTEM and EELS. *Solid State Ionics* **303**, 103–112 (2017).

106. Perdew, J. P. & Yue, W. Accurate and simple density functional for the electronic exchange energy: Generalized gradient approximation. *Phys. Rev. B* **33**, 8800–8802 (1986).

107. Joubert, D. From ultrasoft pseudopotentials to the projector augmented-wave method. *Phys. Rev. B - Condens. Matter Mater. Phys.* **59**, 1758–1775 (1999).

108. Kresse, G. & Hafner, J. Ab initio molecular-dynamics simulation of the liquid-metalamorphous- semiconductor transition in germanium. *Phys. Rev. B* **49**, 14251–14269 (1994).

109. Kresse, G. & Furthmüller, J. Efficiency of ab-initio total energy calculations for metals and semiconductors using a plane-wave basis set. *Comput. Mater. Sci.* **6**, 15–50 (1996).

110. Farhat, D. Bookworms and party animals: An artificial labour market with human and social capital accumulation. *J. Educ. Work* **27**, 1–42 (2014).

111. Henkelman, G., Uberuaga, B. P. & Jónsson, H. A Climbing image nudged elastic band method for finding saddle points and minimum energy paths. *J. Chem. Phys.* **113**, 9901–9904 (2000).

112. Wynn, T. A., Lee, J. Z., Banerjee, A. & Meng, Y. S. In situ and operando probing of solid–solid interfaces in electrochemical devices. *MRS Bull.* **43**, 768–774 (2018).

113. Lorger, S., Usiskin, R. & Maier, J. Transport and Charge Carrier Chemistry in Lithium

Oxide. *J. Electrochem. Soc.* **166**, A2215–A2220 (2019).

114. Lapp, T., Skaarup, S. & Hooper, A. Ionic conductivity of pure and doped Li3N. *Solid State Ionics* **11**, 97–103 (1983).

115. Jodi, H., Supardi, S., Kartini, E. & Zulfia, A. SYNTHESIS AND ELECTROCHEMICAL CHARACTERIZATION OF Li3PO4 FORSOLID STATE ELECTROLYTES. *J. Sains Mater. Indones.* **18**, 1 (2018).

116. Adam-benvenïste, M. Study of the electrical conductivity of lithium fluoride. (Université de Paris, 1969).

117. Stoebe, G. T. Influence of OH- Ions on Infrared Absorption and Ionic Conductivity in Lithium Fluoride Crystals. *J. Phys. Chem. Solids* **28**, 1375–1382 (1967).

118. Fast Ion Transport in Li2SO4-LiCl Mixed crystal and multiphase system. *Solid State Ionics* **24**, 121–127 (1987).

119. Court-Castagnet, R., Kaps, C., Cros, C. & Hagenmuller, P. Ionic conductivity-enhancement of LiCl by homogeneous and heterogeneous dopings. *Solid State Ionics* **61**, 327–334 (1993).

120. Choi, S., Yoon, I., Nichols, W. T. & Shin, D. Carbon-coated Li2S cathode for improving the electrochemical properties of an all-solid-state lithium-sulfur battery using Li2S-P2S5 solid electrolyte. *Ceram. Int.* **44**, 7450–7453 (2018).

121. Hakari, T., Hayashi, A. & Tatsumisago, M. Highly utilized lithium sulfide active material by enhancing conductivity in All-solid-state batteries. *Chem. Lett.* **44**, 1664–1666 (2015).

122. Zhu, Y., He, X. & Mo, Y. Strategies Based on Nitride Materials Chemistry to Stabilize Li Metal Anode. 1–11 (2017) doi:10.1002/advs.201600517.

123. Wu, M., Wen, Z., Liu, Y., Wang, X. & Huang, L. Electrochemical behaviors of a Li3N modified Li metal electrode in secondary lithium batteries. *J. Power Sources* **196**, 8091–8097 (2011).

124. Ediger, M. D. Perspective: Highly stable vapor-deposited glasses. *J. Chem. Phys.* **147**, 210901 (2017).

125. Wenzel, S., Randau, S., Leichtweiß, T., Weber, D. A., Sann, J., Zeier, W. G. & Janek, J. Direct Observation of the Interfacial Instability of the Fast Ionic Conductor Li10GeP2S12 at the Lithium Metal Anode. *Chem. Mater.* **28**, 2400–2407 (2016).

126. Doux, J. M., Nguyen, H., Tan, D. H. S., Banerjee, A., Wang, X., Wu, E. A., Jo, C., Yang, H. & Meng, Y. S. Stack Pressure Considerations for Room-Temperature All-Solid-State Lithium Metal Batteries. *Adv. Energy Mater.* **10**, 1–6 (2020).

127. Jain, A., Ong, S. P., Hautier, G., Chen, W., Richards, W. D., Dacek, S., Cholia, S., Gunter, D., Skinner, D., Ceder, G. & Persson, K. A. Commentary: The materials project: A materials genome approach to accelerating materials innovation. *APL Materials* vol. 1 at https://doi.org/10.1063/1.4812323 (2013).

128. Luo, Y. R. *Comprehensive handbook of chemical bond energies*. *Comprehensive Handbook of Chemical Bond Energies* (2007). doi:10.1201/9781420007282.

129. Leung, K., Pearse, A. J., Talin, A. A., Fuller, E. J., Rubloff, G. W. & Modine, N. A. Kinetics-Controlled Degradation Reactions at Crystalline LiPON/LixCoO2 and Crystalline LiPON/Li-Metal Interfaces. *ChemSusChem* **11**, 1956–1969 (2018).

130. Placke, T., Kloepsch, R., Dühnen, S. & Winter, M. Lithium ion, lithium metal, and alternative rechargeable battery technologies: the odyssey for high energy density. *J. Solid State Electrochem.* **21**, 1939–1964 (2017).

131. Reddy, M. V., Mauger, A., Julien, C. M., Paolella, A. & Zaghib, K. Brief history of early

lithium-battery development. *Materials (Basel).* **13**, 1–9 (2020).

132. Liu, J., Bao, Z., Cui, Y., Dufek, E. J., Goodenough, J. B., Khalifah, P., Li, Q., Liaw, B. Y., Liu, P., Manthiram, A., Meng, Y. S., Subramanian, V. R., Toney, M. F., Viswanathan, V. V, Whittingham, M. S., Xiao, J., Xu, W., Yang, J., Yang, X.-Q., Pathways for practical high-energy long-cycling lithium metal batteries. *Nat. Energy* 10.1038/s41560-019-0338–x (2019) doi:10.1038/s41560-019-0338-x.

133. Tarascon, J.-M. & Armand, M. Issues and challenges facing rechargeable lithium batteries. *Nature* **414**, 359–367 (2001).

134. Choi, J. W. & Aurbach, D. Promise and reality of post-lithium-ion batteries with high energy densities. *Nat. Rev. Mater.* **1**, (2016).

135. Lu, J. & Lee, K. S. Spinel cathodes for advanced lithium ion batteries: a review of challenges and recent progress. *Mater. Technol.* **31**, 628–641 (2016).

136. Yu, X., Yu, W. A. & Manthiram, A. Advances and Prospects of High-Voltage Spinel Cathodes for Lithium-Based Batteries. *Small Methods* **5**, 1–30 (2021).

137. Li, W., Cho, Y. G., Yao, W., Li, Y., Cronk, A., Shimizu, R., Schroeder, M. A., Fu, Y., Zou, F., Battaglia, V., Manthiram, A., Zhang, M. & Meng, Y. S. Enabling high areal capacity for Co-free high voltage spinel materials in next-generation Li-ion batteries. *J. Power Sources* **473**, 228579 (2020).

138. Li, Y., Veith, G. M., Browning, K. L., Chen, J., Hensley, D. K., Paranthaman, M. P., Dai, S. & Sun, X. G. Lithium malonatoborate additives enabled stable cycling of 5 V lithium metal and lithium ion batteries. *Nano Energy* **40**, 9–19 (2017).

139. Arbizzani, C., De Giorgio, F. & Mastragostino, M. Characterization tests for plug-in hybrid electric vehicle application of graphite/LiNi0.4Mn1.6O4 cells with two different separators and electrolytes. *J. Power Sources* **266**, 170–174 (2014).

140. Mancini, M., Axmann, P., Gabrielli, G., Kinyanjui, M., Kaiser, U. & Wohlfahrt-Mehrens, M. A High-Voltage and High-Capacity Li1+x Ni0.5 Mn1.5 O4 Cathode Material: From Synthesis to Full Lithium-Ion Cells. *ChemSusChem* **9**, 1843–1849 (2016).

141. Yang, L., Ravdel, B. & Lucht, B. L. Electrolyte reactions with the surface of high voltage LiNi 0.5Mn1.5O4 cathodes for lithium-ion batteries. *Electrochem. Solid-State Lett.* **13**, 95–98 (2010).

142. Pieczonka, N. P. W., Liu, Z., Lu, P., Olson, K. L., Moote, J., Powell, B. R. & Kim, J. H. Understanding transition-metal dissolution behavior in LiNi 0.5Mn1.5O4 high-voltage spinel for lithium ion batteries. *J. Phys. Chem. C* **117**, 15947–15957 (2013).

143. Li, W., Song, B. & Manthiram, A. High-voltage positive electrode materials for lithium-ion batteries. *Chem. Soc. Rev.* **46**, 3006–3059 (2017).

144. Takada, K. Progress in solid electrolytes toward realizing solid-state lithium batteries. *J. Power Sources* **394**, 74–85 (2018).

145. Asl, H. Y. & Manthiram, A. Reining in dissolved transition-metal ions. *Science (80-.).* **369**, 140–141 (2020).

146. Herbert, E. G., Tenhaeff, W. E., Dudney, N. J. & Pharr, G. M. Mechanical characterization of LiPON films using nanoindentation. *Thin Solid Films* **520**, 413–418 (2011).

147. Iriyama, Y., Nishimoto, K., Yada, C., Abe, T., Ogumi, Z. & Kikuchi, K. Charge-Transfer Reaction at the Lithium Phosphorus Oxynitride Glass Electrolyte/Lithium Manganese Oxide Thin-Film Interface and Its Stability on Cycling. *J. Electrochem. Soc.* **153**, A821 (2006).

148. Phillip, N. D., Westover, A. S., Daniel, C. & Veith, G. M. Structural Degradation of High Voltage Lithium Nickel Manganese Cobalt Oxide (NMC) Cathodes in Solid-State Batteries and Implications for Next Generation Energy Storage. *ACS Appl. Energy Mater.* **3**, 1768–1774 (2020).

149. Xia, H., Tang, S. B., Lu, L., Meng, Y. S. & Ceder, G. The influence of preparation conditions on electrochemical properties of LiNi0.5Mn1.5O4 thin film electrodes by PLD. *Electrochim. Acta* **52**, 2822–2828 (2007).

150. Xia, H., Meng, Y. S., Lu, L. & Ceder, G. Electrochemical Properties of Nonstoichiometric LiNi[sub 0.5]Mn[sub 1.5]O[sub 4−δ] Thin-Film Electrodes Prepared by Pulsed Laser Deposition. *J. Electrochem. Soc.* **154**, A737 (2007).

151. Song, J., Shin, D. W., Lu, Y., Amos, C. D., Manthiram, A. & Goodenough, J. B. Role of Oxygen Vacancies on the Performance of Li[Ni0.5−xMn1.5+x]O4 (x = 0, 0.05, and 0.08) Spinel Cathodes for Lithium-Ion Batteries. *Chem. Mater.* **24**, 3101–3109 (2012).

152. Lee, E., Nam, K., Hu, E. & Manthiram, A. Influence of Cation Ordering and Lattice Distortion on the Charge− Discharge Behavior of LiMn1.5Ni0.5O4 Spinel between 5.0 and 2.0 V. *Chem. Mater.* **24**, 3610–3620 (2012).

153. Xia, H., Tang, S. B., Lu, L., Meng, Y. S. & Ceder, G. The influence of preparation conditions on electrochemical properties of LiNi0.5Mn1.5O4 thin film electrodes by PLD. *Electrochim. Acta* **52**, 2822–2828 (2007).

154. Lamaze, G. P., Chen-Mayer, H. H., Becker, D. A., Vereda, F., Goldner, R. B., Haas, T. & Zerigian, P. Cold neutron depth profiling of lithium-ion battery materials. *J. Power Sources* **119**–**121**, 680–685 (2003).

155. Downing, R. G., Lamaze, G. P., Langland, J. K. & Hwang, S. T. Neutron depth profiling: Overview and description of NIST facilities. *J. Res. Natl. Inst. Stand. Technol.* **98**, 109–126 (1993).

156. Tan, C., Leung, K. Y., Liu, D. X., Canova, M., Downing, R. G., Co, A. C. & Cao, L. R. Gamma radiation effects on Li-ion battery electrolyte in neutron depth profiling for lithium quantification. *J. Radioanal. Nucl. Chem.* **305**, 675–680 (2015).

157. Nagpure, S. C., Downing, R. G., Bhushan, B., Babu, S. S. & Cao, L. Neutron depth profiling technique for studying aging in Li-ion batteries. *Electrochim. Acta* **56**, 4735–4743 (2011).

158. Zhang, X., Verhallen, T. W., Labohm, F. & Wagemaker, M. Direct Observation of Li-Ion Transport in Electrodes under Nonequilibrium Conditions Using Neutron Depth Profiling. *Adv. Energy Mater.* **5**, 1–8 (2015).

159. Wang, C., Gong, Y., Dai, J., Zhang, L., Xie, H., Pastel, G., Liu, B., Wachsman, E., Wang, H. & Hu, L. In Situ Neutron Depth Profiling of Lithium Metal-Garnet Interfaces for Solid State Batteries. *J. Am. Chem. Soc.* **139**, 14257–14264 (2017).

160. Lyons, D. J., Weaver, J. L. & Co, A. C. Considerations in applying neutron depth profiling (NDP) to Li-ion battery research. *J. Mater. Chem. A* **10**, 2336–2351 (2022).

161. Intan, N. N., Klyukin, K. & Alexandrov, V. Theoretical Insights into Oxidation States of Transition Metals at (001) and (111) LiNi 0.5 Mn 1.5 O 4 Spinel Surfaces . *J. Electrochem. Soc.* **165**, A1099–A1103 (2018).

162. Xu, B., Fell, C. R., Chi, M. & Meng, Y. S. Identifying surface structural changes in layered Li-excess nickel manganese oxides in high voltage lithium ion batteries: A joint experimental and theoretical study. *Energy Environ. Sci.* **4**, 2223–2233 (2011).

163. Wang, Z. L., Yin, J. S. & Jiang, Y. D. EELS analysis of cation valence states and oxygen

vacancies in magnetic oxides. *Micron* **31**, 571–580 (2000).

164. Liang, W., Wang, P., Ding, H., Wang, B. & Li, S. Granularity control enables high stability and elevated-temperature properties of micron-sized single-crystal LiNi0.5Mn1.5O4 cathodes at high voltage. *J. Mater.* **7**, 1049–1060 (2021).

165. Luo, S., Li, J., Lu, J., Tao, F., Wan, J., Zhang, B., Zhou, X. & Hu, C. High-performance aqueous asymmetric supercapacitor based on hierarchical wheatear-like LiNi0.5Mn1.5O4 cathode and porous Fe2O3 anode. *Mater. Today Phys.* **17**, 100337 (2021).

166. Schichtel, P., Geiß, M., Leichtweiß, T., Sann, J., Weber, D. A. & Janek, J. On the impedance and phase transition of thin film all-solid-state batteries based on the Li4Ti5O12 system. *J. Power Sources* **360**, 593–604 (2017).

167. Santhanagopalan, D., Qian, D., Mcgilvray, T., Wang, Z., Wang, F., Camino, F., Graetz, J., Dudney, N. & Meng, Y. S. Interface Limited Lithium Transport in Solid-State Batteries. (2014) doi:10.1021/jz402467x.

168. Usubelli, C., Besli, M. M., Kuppan, S., Jiang, N., Metzger, M., Dinia, A., Christensen, J. & Gorlin, Y. Understanding the Overlithiation Properties of LiNi 0.6 Mn 0.2 Co 0.2 O 2 Using Electrochemistry and Depth-Resolved X-ray Absorption Spectroscopy . *J. Electrochem. Soc.* **167**, 080514 (2020).

169. Takada, K., Ohno, T., Ohta, N., Ohnishi, T. & Tanaka, Y. Positive and Negative Aspects of Interfaces in Solid-State Batteries. *ACS Energy Lett.* **3**, 98–103 (2018).

170. De Klerk, N. J. J. & Wagemaker, M. Space-Charge Layers in All-Solid-State Batteries; Important or Negligible? *ACS Appl. Energy Mater.* **1**, 5609–5618 (2018).

171. Kawasoko, H., Shiraki, S., Suzuki, T., Shimizu, R. & Hitosugi, T. Extremely Low Resistance of Li3PO4Electrolyte/Li(Ni0.5Mn1.5)O4Electrode Interfaces. *ACS Appl. Mater. Interfaces* **10**, 27498–27502 (2018).

172. Xia, Q., Sun, S., Xu, J., Zan, F., Yue, J., Zhang, Q., Gu, L. & Xia, H. Self-Standing 3D Cathodes for All-Solid-State Thin Film Lithium Batteries with Improved Interface Kinetics. *Small* **14**, 1–11 (2018).

173. Sharafi, A., Meyer, H. M., Nanda, J., Wolfenstine, J. & Sakamoto, J. Characterizing the Li-Li7La3Zr2O12 interface stability and kinetics as a function of temperature and current density. *J. Power Sources* **302**, 135–139 (2016).

174. Zhang, W., Leichtweiß, T., Culver, S. P., Koerver, R., Das, D., Weber, D. A., Zeier, W. G. & Janek, J. The Detrimental Effects of Carbon Additives in Li10GeP2S12-Based Solid-State Batteries. *ACS Appl. Mater. Interfaces* **9**, 35888–35896 (2017).

175. Tan, D. H. S., Wu, E. A., Nguyen, H., Chen, Z., Marple, M. A. T., Doux, J.-M., Wang, X., Yang, H., Banerjee, A. & Meng, Y. S. Elucidating Reversible Electrochemical Redox of Li6PS5Cl Solid Electrolyte. *ACS Energy Lett.* 2418–2427 (2019) doi:10.1021/ACSENERGYLETT.9B01693.

176. Tan, D. H. S., Chen, Y. T., Yang, H., Bao, W., Sreenarayanan, B., Doux, J. M., Li, W., Lu, B., Ham, S. Y., Sayahpour, B., Scharf, J., Wu, E. A., Deysher, G., Han, H. E., Hah, H. J., Jeong, H., Lee, J. B., Chen, Z. & Meng, Y. S. Carbon-free high-loading silicon anodes enabled by sulfide solid electrolytes. *Science (80-.).* **373**, 1494–1499 (2021).

177. Hood, Z. D., Chen, X., Sacci, R. L., Liu, X., Veith, G. M., Mo, Y., Niu, J., Dudney, N. J. & Chi, M. Elucidating Interfacial Stability between Lithium Metal Anode and Li Phosphorus Oxynitride via in Situ Electron Microscopy. *Nano Lett.* **21**, 151–157 (2021).

178. Lewis, J. A., Tippens, J., Cortes, F. J. Q. & McDowell, M. T. Chemo-Mechanical Challenges in Solid-State Batteries. *Trends Chem.* 1–14 (2019)

doi:10.1016/j.trechm.2019.06.013.

179. Xu, F., Belliard, L., Fournier, D., Charron, E., Duquesne, J. Y., Martin, S., Secouard, C. & Perrin, B. Complete elastic characterization of lithium phosphorous oxynitride films using picosecond ultrasonics. *Thin Solid Films* **548**, 366–370 (2013).

180. Kozen, A. C., Pearse, A. J., Lin, C. F., Noked, M. & Rubloff, G. W. Atomic Layer Deposition of the Solid Electrolyte LiPON. *Chem. Mater.* **27**, 5324–5331 (2015).

181. Muñoz, F., Durán, A., Pascual, L., Montagne, L., Revel, B. & Rodrigues, A. C. M. Increased electrical conductivity of LiPON glasses produced by ammonolysis. *Solid State Ionics* **179**, 574–579 (2008).

182. Westover, A. S., Kercher, A. K., Kornbluth, M., Naguib, M., Palmer, M. J., Cullen, D. A. & Dudney, N. J. Plasma Synthesis of Spherical Crystalline and Amorphous Electrolyte Nanopowders for Solid-State Batteries. *ACS Appl. Mater. Interfaces* **12**, 11570–11578 (2020).

183. López-Aranguren, P., Reynaud, M., Głuchowski, P., Bustinza, A., Galceran, M., López del Amo, J. M., Armand, M. & Casas-Cabanas, M. Crystalline LiPON as a Bulk-Type Solid Electrolyte. *ACS Energy Lett.* 445–450 (2021) doi:10.1021/acsenergylett.0c02336.

184. Le Van-Jodin, L., Ducroquet, F., Sabary, F. & Chevalier, I. Dielectric properties, conductivity and Li+ ion motion in LiPON thin films. *Solid State Ionics* **253**, 151–156 (2013).

185. Köcher, S. S., Schleker, P. P. M., Graf, M. F., Eichel, R. A., Reuter, K., Granwehr, J. & Scheurer, C. Chemical shift reference scale for Li solid state NMR derived by first-principles DFT calculations. *J. Magn. Reson.* **297**, 33–41 (2018).

186. M. F. Vieira, E., F. Ribeiro, J., Sousa, R., G. Rolo, A., M. Silva, M. & M. Goncalves, L. Flexible solid-state Ge – LiCoO2 battery: From materials to device application. *Adv. Mater. Lett.* **8**, 820–829 (2017).

187. Sepúlveda, A., Criscuolo, F., Put, B. & Vereecken, P. M. Effect of high temperature LiPON electrolyte in all solid state batteries. *Solid State Ionics* **337**, 24–32 (2019).

188. Kalnaus, S., Westover, A. S., Kornbluth, M., Herbert, E. & Dudney, N. J. Resistance to fracture in the glassy solid electrolyte Lipon. *J. Mater. Res.* 1–10 (2021) doi:10.1557/s43578-020-00098-x.

189. Ma, D., Chung, W. O., Liu, J. & He, J. Determination of Young's modulus by nanoindentation. *Sci. China, Ser. E Technol. Sci.* **47**, 398–408 (2004).

190. Abadias, G. & Daniel, R. *Stress in physical vapor deposited thin films: Measurement methods and selected examples. Handbook of Modern Coating Technologies* (BV, 2021). doi:10.1016/b978-0-444-63239-5.00008-1.

191. Swadener, J. G., Taljat, B. & Pharr, G. M. Measurement of residual stress by load and depth sensing indentation with spherical indenters. *J. Mater. Res.* **16**, 2091–2102 (2001).

192. Hobold, G. M., Lopez, J., Guo, R., Minafra, N., Banerjee, A., Shirley Meng, Y., Shao-Horn, Y. & Gallant, B. M. Moving beyond 99.9% Coulombic efficiency for lithium anodes in liquid electrolytes. *Nat. Energy* **6**, 951–960 (2021).

193. Wang, M. J., Carmona, E., Gupta, A., Albertus, P. & Sakamoto, J. Enabling "lithium-free" manufacturing of pure lithium metal solid-state batteries through in situ plating. *Nat. Commun.* **11**, 1–9 (2020).

194. Motoyama, M., Ejiri, M. & Iriyama, Y. Modeling the Nucleation and Growth of Li at Metal Current Collector/LiPON Interfaces. *J. Electrochem. Soc.* **162**, A7067–A7071 (2015).

195. Yan, K., Lu, Z., Lee, H. W., Xiong, F., Hsu, P. C., Li, Y., Zhao, J., Chu, S. & Cui, Y. Selective deposition and stable encapsulation of lithium through heterogeneous seeded growth. *Nat. Energy* **1**, 16010 (2016).

196. Lee, K., Kazyak, E., Wang, M. J., Dasgupta, N. P. & Sakamoto, J. Analyzing void formation and rewetting of thin in situ-formed Li anodes on LLZO. *Joule* **6**, 2547–2565 (2022).

197. Kasemchainan, J., Zekoll, S., Spencer Jolly, D., Ning, Z., Hartley, G. O., Marrow, J. & Bruce, P. G. Critical stripping current leads to dendrite formation on plating in lithium anode solid electrolyte cells. *Nat. Mater.* **18**, 1105–1111 (2019).

198. Egerton, R. F., Li, P. & Malac, M. Radiation damage in the TEM and SEM. *Micron* **35**, 399–409 (2004).

199. Jiang, N. Electron beam damage in oxides: A review. *Reports Prog. Phys.* **79**, (2015).

200. Wang, X., Li, Y. & Meng, Y. S. Cryogenic Electron Microscopy for Characterizing and Diagnosing Batteries. *Joule* **2**, 2225–2234 (2018).

201. Schorb, M., Haberbosch, I., Hagen, W. J. H., Schwab, Y. & Mastronarde, D. N. Software tools for automated transmission electron microscopy. *Nat. Methods* **16**, 471–477 (2019).

202. Wang, F., Graetz, J., Moreno, M. S., Ma, C., Wu, L., Volkov, V. & Zhu, Y. Chemical distribution and bonding of lithium in intercalated graphite: Identification with optimized electron energy loss spectroscopy. *ACS Nano* **5**, 1190–1197 (2011).

203. Güven, G. & Oktay, A. B. Nanoparticle detection from TEM images with deep learning. *26th IEEE Signal Process. Commun. Appl. Conf. SIU 2018* 1–4 (2018) doi:10.1109/SIU.2018.8404468.

204. Horwath, J. P., Zakharov, D. N., Mégret, R. & Stach, E. A. Understanding important features of deep learning models for segmentation of high-resolution transmission electron microscopy images. *npj Comput. Mater.* **6**, 1–9 (2020).

205. Ronneberger, O., Fischer, P. & Brox, T. INet: Convolutional Networks for Biomedical Image Segmentation. *arXiv:1505.04597* 1–8 (2015) doi:10.1109/ACCESS.2021.3053408.

206. Hill, J., Mulholland, G., Persson, K., Seshadri, R., Wolverton, C. & Meredig, B. Materials science with large-scale data and informatics: Unlocking new opportunities. *MRS Bull.* **41**, 399–409 (2016).

207. Heron, M., Hanson, V. L. & Ricketts, I. Open Source - Acessibility and limitations. *J. Interact. Sci.* **1(1)**, 1–10 (2013).

208. Rafique, K., Tareen, A. W., Saeed, M., Wu, J. & Qureshi, S. S. Cloud computing economics opportunities and challenges. in *Proceedings - 2011 4th IEEE International Conference on Broadband Network and Multimedia Technology, IC-BNMT 2011* 401–406 (IEEE, 2011). doi:10.1109/ICBNMT.2011.6155965.

209. Cusumano, M. Cloud computing and SaaS as new computing platforms. *Commun. ACM* **53**, 27–29 (2010).